Irradiation Behaviour of High Entropy Alloys

By Fu Honglun (傅弘伦)

Thesis submitted in accordance with the requirements of the University of Liverpool and National Tsing Hua University for the degree of Doctor in Philosophy (Dual-PhD)

September 2021

Abstract

Four high entropy alloys (HEA), CoCrCuFeNi, Co1.5CrFeNi1.5Ti0.5Mo0.1, both adopting an FCC structure, and TaNbHfZrTi, and AlCoCrFeNiSi, adopting a BCC structure, have been irradiated with He and 3 MeV Ni ions, as part of the process of understanding their application within fission based nuclear reactors.

When irradiated nano-indentation analysis shows that the FCC and BCC respond differently. The FCC phases show a decrease in hardness with increasing ion fluence, for example at depth of 100nm CoCrCuFeNi shows a decrease from ~7.5 GPa to ~4.5 GPa. However, the BCC phases show an initial increase in hardness with ion fluence, for example at a depth of 100nm TaNbHfZrTi, shows an intial increase from ~9.5 GPa to ~ 10.2 GPa, with a subsequent drop to ~8.75 GPa.

Transmission electron microscopy based analysis shows that ion beam induced damage is visible in the samples, with 3 MeV Ni inducing differing levels of visible damage. Analysis of He irradiated samples suggests that there might be beginnings of bubble formation, but the evidence is not clear cut.

Acknowledgements

I am deeply grateful to this joint degree program between University of Liverpool and National Tsing Hua University. This program offered me a great opportunity to join the PhD. study. I am very enjoyed this research time and I will always remember this experience.

I would like to express special thanks to Professor Karl Whittle from the bottom of my heart. With long patience and guidance, he tutored me through the majority of my student and research life. As an overseas student, I received great encouragement from him with generosity and perfusions to actively adept in new live and study environment. He also offered me this great opportunity to start this project which allows me to extend my skill and vision of scientific study. I am very lucky to meet such a supervisor and he will keep enlightening my future path with his teaching and professional advice.

I also want to deliver great thanks and respect to Professor Jenq-Horng Liang. He is a wise and elegant man and researcher. I received a lot of useful advice from him to become a more organised and humbler as a person and as a researcher.

I want to thank Doctor Karl Dawson and Doctor Maulik Patel. I have taken onboard a lot of research expertise and training from them. They helped me to resolve issues from experiments and ensured the work continued.

I would like to dress extend thanks to Doctor Anna Kareer. She offered a great deal of help on sample synthesis. Due to the nature of high entropy alloy, the synthesis equipment she provided was extremely valuable to this project.

I want to thank my partner Miss. Xiaqi Ye. She accompanied me in this extremely difficult pandemic time. She supported me during this stressful time.

I owe my deepest gratitude to my parents Mr. Yanqiao Fu and Mrs. Shuyun Song. I love them not only for they bring me to this beautiful world, but also love and teach me.

This thesis is dedicated to everyone who offer extreme generosity and helping to this project, especially in this extremely difficult time period.

Covid-19 Mitigation Statement

The work presented in this thesis was that undertaken until mid 2020, at this point it became apparent that due to the Covid-19 situation in the UK it would be unlikely that the planned experimental work could be completed in time. The decision was therefore made to complete the outstanding analysis of collected data. The planned work that could not be continued was the irradiation of the samples by 4.5 MeV Au, which was planned for mid-April 2020.

Linked with this situation the analysis of the changes induced by the irradiation was also restricted in access to the microscopy facilities, due to the necessity for safe working, with access restricted to one user per week.

As the situation evolved it became apparent that irradiation was unlikely to occur until at least the autumn of 2020, which coupled with the availability of SEM/TEM time made it impossible to complete the work in the time available.

The results obtained from the planned 4.5 MeV Au irradiation would have helped with increased understanding of the effects from radiation and provided information on the changes in properties from higher levels of damage. To that end this thesis contains the completed analysis that could be undertaken, with interim conclusions drawn from the work.

Chapter 1 - Introduction

1.1 Background

A high entropy alloy or HEA is an innovative type of alloy system when compared with conventional alloys.[1] High entropy alloys have a range of advanced properties such as high strength and toughness. One of the attractive characteristics of high entropy alloys, above all is the ability to maintain high grade mechanical properties under high temperature working conditions.[2] Combined with high creep resistance and hardness, high entropy alloys have the potential to be used in harsh working environments, particularly those at high temperature.[3]

In recent years, an evolving energy crisis has started to become apparent, with an increasing number of people appreciating that an ever increasing demand for energy and preservation of environment are in conflict.[4] In order to generate energy both safely and environmentally friendly, many new methods and technologies have been proposed for power generation such as solar energy, wind energy etc. However, compared with other energy forms, nuclear power has its advantages. The most obvious one is generating energy density which, whilst not a precise scientific term, can be described as the relationship between power output and total land area required. Due to its significantly high energy density, nuclear power is highly suitable for powering modern industry.[5] Alternately, most green energy sources have a secondary problem, that is a lack of consistency in supply. They normally rely on environmental conditions, such as solar energy relies on sun light whilst wind power relies on wind. This limitation will significantly increase running costs for each, as in many cases the working time cannot reach 24 hours per day. As a result, the power output can be unstable which will require vast and complex equipment to compensate for supply and voltage drop off. Therefore, nuclear power is more suitable for modern industry and production, when judged by the current technology and developing tendency, nuclear power is the most promising energy source compare with others.

Nuclear reactor cores are one of the harshest working environments. For example, in a reactor core, the parts and componentry will not only experience high temperatures and pressures but also a high fluence of particle irradiation. Irradiation induced damage can impact the material at the atomic level.[6] With irradiation damage accumulation, the material can lose its fundamental crystal structure, leading to the loss of macro mechanical properties. Applying more reliable core materials within the reactor, the design tolerance of nuclear reactor can be significantly increased along with the overall power efficiency of entire power plant. An increase in design tolerance can significantly raise the safety standards of nuclear power, which continues to be one of the important challenges for all nuclear energy generation and usage. High entropy alloys have great potential as they can retain mechanical properties when experiencing significant irradiation induced damage. With longer service time before replacement of parts, the maintenance cycle of nuclear reactor can be elongated, giving rise to a longer operational lifetime of the power plant, lower running costs and lower potential risk caused by maintaining process. [7]

The focus of this project is to identify radiation induced damage behaviour of high entropy alloys, with a close focus on microstructural changes. The determination of radiation induced damage resistance is based on two different approaches. The first one focuses on the changes in microstructure after receiving significant amounts of irradiation induced damage, using high energy particle irradiation. Such damage, defined by displacements per atom or dpa, is key to identify if a material can maintain its overall structure, with the original orientation being disrupted, particularly if the material maintains its mechanical properties after receiving high doses of irradiation. The second focus is the determination of the mechanical property change linked with the radiation damage build up. Mechanical hardness change is an obvious factor to determine, with the primary consideration being that, with radiation damage build up, the material will modify its hardness and shift in value. For example, in many cases, hardness will be increased with radiation embrittlement, whilst at the same time, the damaging radiation is also able to relax the material structure and reduce the hardness.

1.2 Nuclear power

A basic description of a nuclear power station is a complex system capable of converting released binding energy as heating and converting it to electricity.[8] Once completed a nuclear power station will contain three main parts, the reactor core, a heat cycling system and an electricity generation system. The main principle of nuclear power station is not much different from a conventional coal/gas fired power station. The major difference is the heat source. In a nuclear power plant, the nuclear core itself is providing the heat to boil water to generate steam.[9] Although on a very simplistic scale a nuclear power station and coal/gas fired power station are similar, a nuclear reactor is required to have more redundancy. The main reason is that the nuclear fission process will produce radioactive materials some of which are extreme in their radiotoxicity. Under all conditions, nuclear power station must contain all nuclear fuel and reactive substance inside the reactor, as even a small leakage of nuclear reactor will cause major problems and can have a catastrophic impact on the environment. [8] [10]

However, the world requires more and more energy to support expanding production, and more advanced production technology will need more energy.[7] Currently nuclear power is a reasonable solution for this energy crisis. Therefore, safer, and more efficient nuclear power stations can help restore the trust in nuclear energy.

1.3 Nuclear Fission

All the existing nuclear power plants rely on nuclei fission. Nuclear fission is defined as one atom being split into smaller components, including daughter atom/fission products, neutrons and gamma rays of varying energy.[11] Taking the fissile element, uranium 235 (U-235) as an example, it can split into following.

$${}^{1}_{0}\mathrm{n} + {}^{235}_{92}\mathrm{U} = {}^{141}_{56}\mathrm{Ba} + {}^{92}_{36}\mathrm{Kr} + 3\,{}^{1}_{0}\mathrm{n}$$

When a U-235 nucleus is impacted by a neutron, the nucleus can gain extra mass and energy, and become unstable. Applying the water drop model, under this excited state uranium nuclei start to deform, with the binding force no longer able to hold the increasing potential energy and the nucleus splits, with two newly formed nuclei moving away, often with neutrons also being released. [11] This process not only releases the fragments, but it also releases a significant amount of binding energy, which then becomes heat.

1.4 Nuclear power station

As mentioned previously, a nuclear power station is a system to convert nuclear energy to electrical energy. As showing in Figure 1.1, the fundamental nature of it is a thermal engine.

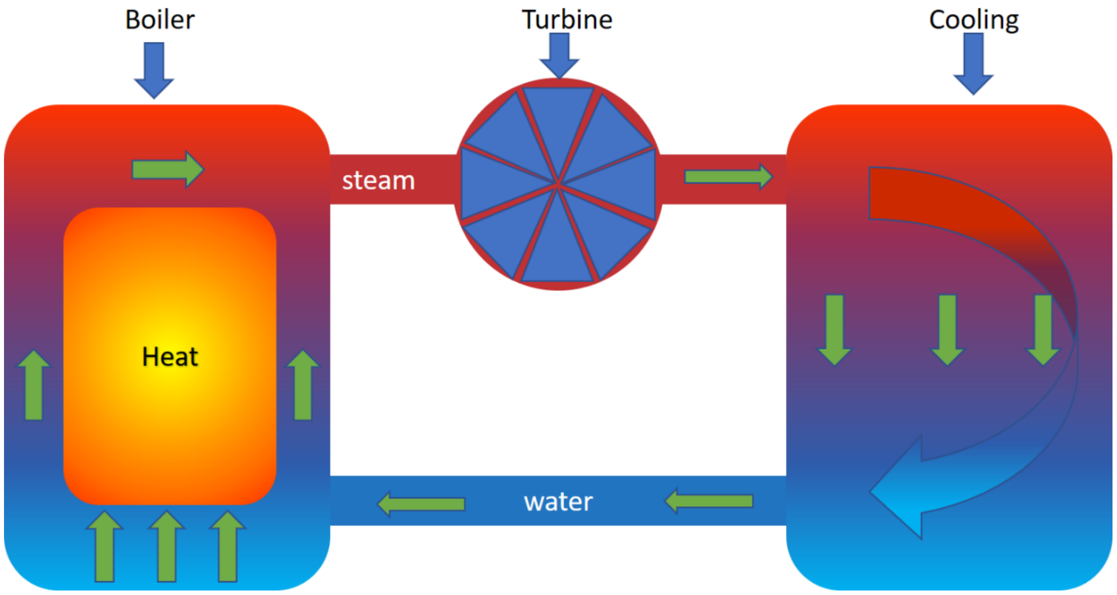

Figure 1.1 - A schematic of a nuclear reactor where the core is effectively a large heat source for a steam turbine [12]

The core part of reactor, where the fission process occurs, is called the pressure vessel. It contains the fissile fuel, control devices and safety measures. The fissile fuel used in modern nuclear reactor is uranium-235, with a common enrichment around 3-5%. It varies with different nuclear power stations designs and purposes. Nuclear reactors are always surrounded by thermal transferring media which has the function of taking the heat away from the core. The most common thermal transferring media is water which has a high specific heat capacity and is easy to obtain. Nuclear fuel has significantly higher energy density when compared with other fuel, such as fossil fuel or even hydrogen gas, therefore an economical nuclear power station will have higher efficiency and are more environmentally friendly when the power station is running under safe and normal conditions. The heat is carried to the turbines as kinetic energy, generally by steam, or it can be by gas. The turbines then transform this kinetic energy into rotation of turbines, converting this thermal/kinetic energy into mechanical energy, which is then used to drive an electrical turbine.

1.5 Nuclear power design

Since nuclear power has been applied to electrical generation the design of a nuclear power station has continuously developed, achieving higher efficiency and output. From the first generation to designs of the future, there are various options of nuclear power station that have been constructed and tested.[8] Generally, the nuclear power station design is directly linked to the design of the core as often the turbine and electricity generator are similar. Different designs have various advantages and disadvantages, but the aim is all the same which is to increase efficiency and safety. [8]

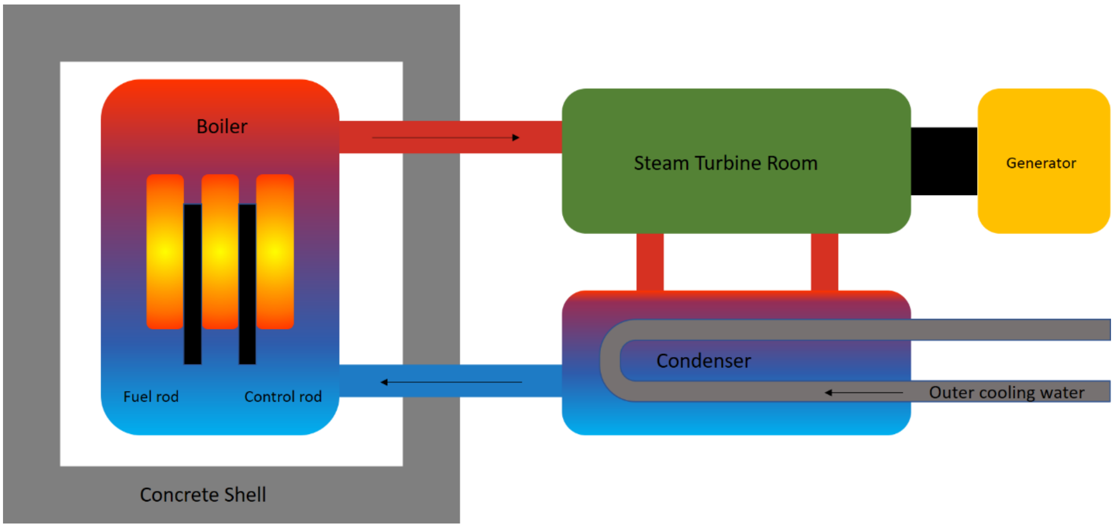

Figure 1.2 - A schematic of a single loop boiling water reactor power station[13]

1.5.1 Boiling Water Reactors (BWR)

A Boiling Water Reactor or BWR is a classic, simple, design of light water reactor. In this type of reactor, the coolant collects heat from nuclear fuel and boils, generating steam, which is directly sent to the turbines. Steam is then condensed back into liquid water and pumped back to the core. As shown in Figure 1.2, the entire system is very simple compared to other design of nuclear reactor. However, it has several disadvantages. Firstly, BWRs operate at ~75 atm or 7.6 MPa, so the maximum steam temperature is around 285 °C. For a thermal engine, this relatively low heat source temperature will significantly limit the total power output of a power station. The second disadvantage is that the steam is directly contact with fuel rod, so all major componentry such as turbine and condenser can be contaminated with radioactive material. This largely increases the maintenance cost and difficulty, also reduced safety measure.[14]

1.5.2 Pressurised Water Reactors (PWR)

A Pressurised Water Reactor or PWR is a popular nuclear power reactor design, accounting for more than 60% of existing nuclear power stations. The main difference between PWR and BWR is that a PWR contains a second circulation system. As shown in the Figure 1.3, the primary cycle loop normally works under ~155 atm or 15.5 MPa and ~320 °C, which is designed to keep water in liquid form. This super-heated water is passed through a heat exchanger to deliver the heat to a second loop, generally this heat exchanger is a steam generator which boils water in secondary loop to generate steam. High temperature steam is then transported to the turbines and condensed. Through this separation between the nuclear fuel and primary coolant water, all the radioactive material can be sealed inside the reactor shell, significantly improving the safety. The total system tolerance is also improved.[14]

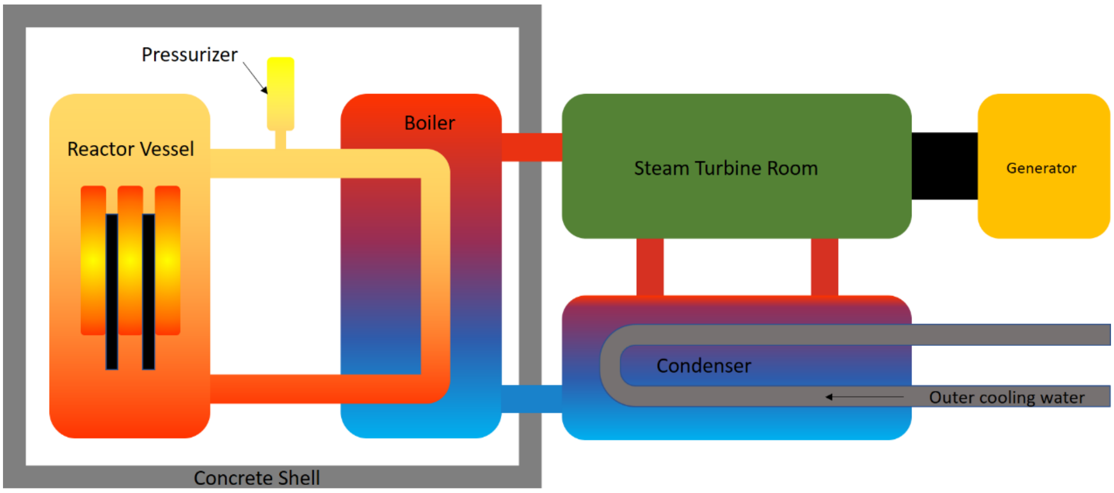

Figure 1.3 - A schematic of a two loop pressured water reactor, the major component is the primary loop and pressuriser [15]

There are other nuclear reactor designs such as the MSR (Molten Salt Reactor), RBMK (Reaktor Bolshoy Moschnosti Kanalniy “High Power Channel Reactor”), Advanced Gas-cooled Reactor (AGR), Liquid Metal Fast-breeder Reactor (LMFBR) etc. These reactors generally work on a different principle to the traditional BWR/PWR design with different conditions, and material requirements.

1.6 Future Nuclear Reactor Designs

With designs evolving nuclear reactors are become more and more compact, with higher total power outputs, with some reactors able to use alternative fissile fuels, for example plutonium and thorium. There are also fast breeder reactors, which are attractive future designs for nuclear reactors which can produce fissile fuel by employ fast neutron capture.

Increasing energy output can be achieved through raising the fission chain reaction rate and heat exchange efficiency. This approach gives rise to the Generation IV fission reactor having significantly higher working temperatures, also giving rise to the working components receiving higher radiation damage within the core.[16] As shown in the Figure. 1.4 some of the Generation IV reactor designs have much higher working temperature, approaching 1000°C in one case. Thus, it gives a higher requirement for materials with creep resistance and high temperature mechanical properties to be able to work at this extremely high temperature. [16] At the same time, the intensity of radiation inside reactor will increase inducing more radiation damage on cladding and other components around the core. During increased service time, high levels of radiation will cause damage, such as swelling, embrittlement and other significant change of mechanical properties. [17] The high temperatures inside a Generation IV reactors requires any cladding used to have much higher corrosion resistance, when compared with current materials. Simple chemical corrosion under this condition becomes more intense, leading to further damage on reactor parts when it is combined with stress and radiation. In current reactor designs, where the most common moderator is water, the chemical corrosion resistance is the primary factor considered when predicting behaviour in water or steam environments.

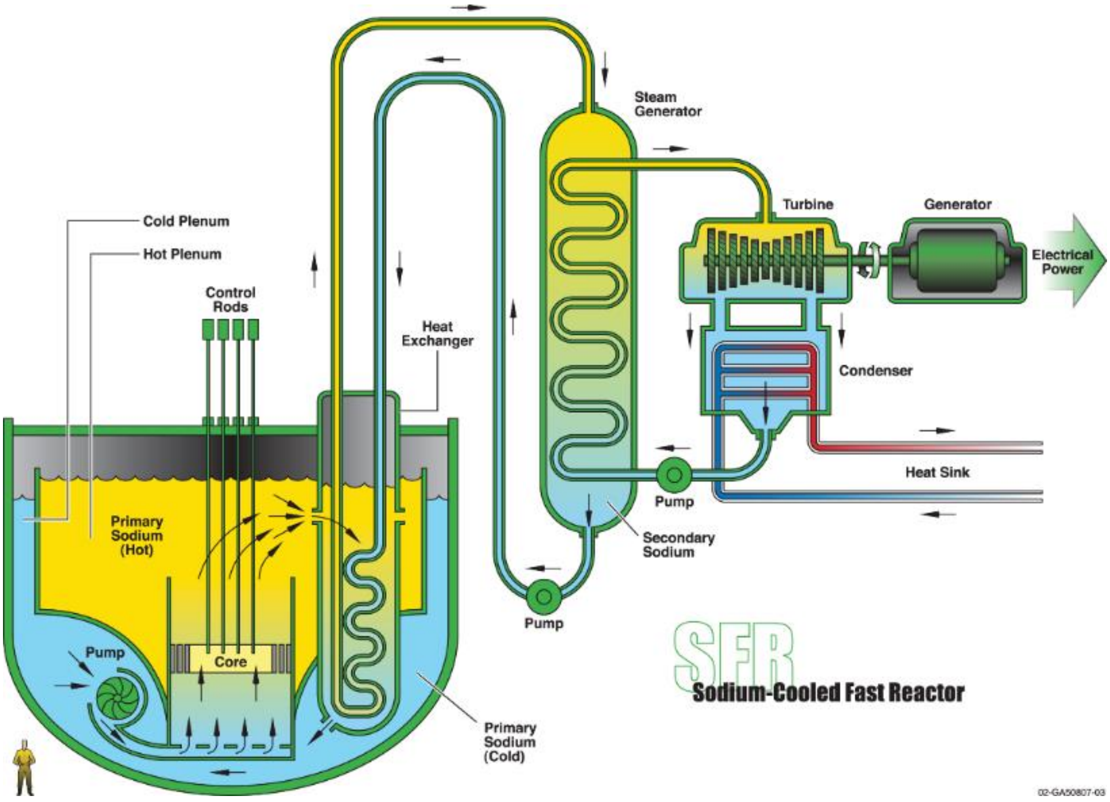

Figure 1.4 - A schematic of sodium cooled fast reactor which is a future design of Gen IV nuclear reactor. It has much smaller size and higher safety measures. [18]

However, in future nuclear reactor designs, other materials are being selected as both a moderator and heat exchange medium. These candidate materials include molten salts, low melting point metals, super critical water etc. These designs have much higher working temperatures which require the structural material, and particularly any cladding to have good mechanical properties under such working environments. The applying of molten salt mixtures and low melting point metals give further challenges for materials. The corrosion mechanism for molten salts is different from corrosion in water, with molten salts able to extract element out from the alloy particularly at the grain boundaries. [19] This modifies a material's microstructure due to shifts in component composition and the surface of sample being physically broken down. The corrosion process not only occurs on the surface but also travels along the grain boundary, finally giving rise to fracture of the sample. The molten metal coolants have similar problems and, when using pure element metals having such a huge impact is a major challenge.

Thus, the next generation of nuclear power plant will have increased energy density with higher power output and smaller reactor volumes. To achieve such design goals, the new generation designs have increased core working temperatures or at least significantly increased from the former type of last generation design. The new challenge is therefore focused on high temperature creep, molten salt corrosion, thermal corrosion etc.

1.7 Cladding Material Choices and Development

As showing in the Figure 1.5, fuel cladding is the nuclear reactor component closest to the nuclear fuel. It requires, unlike some other materials within a reactor, the chosen material to be as highly neutron transparent as possible. This property allows the fission process to proceed with the highest possible efficiency.

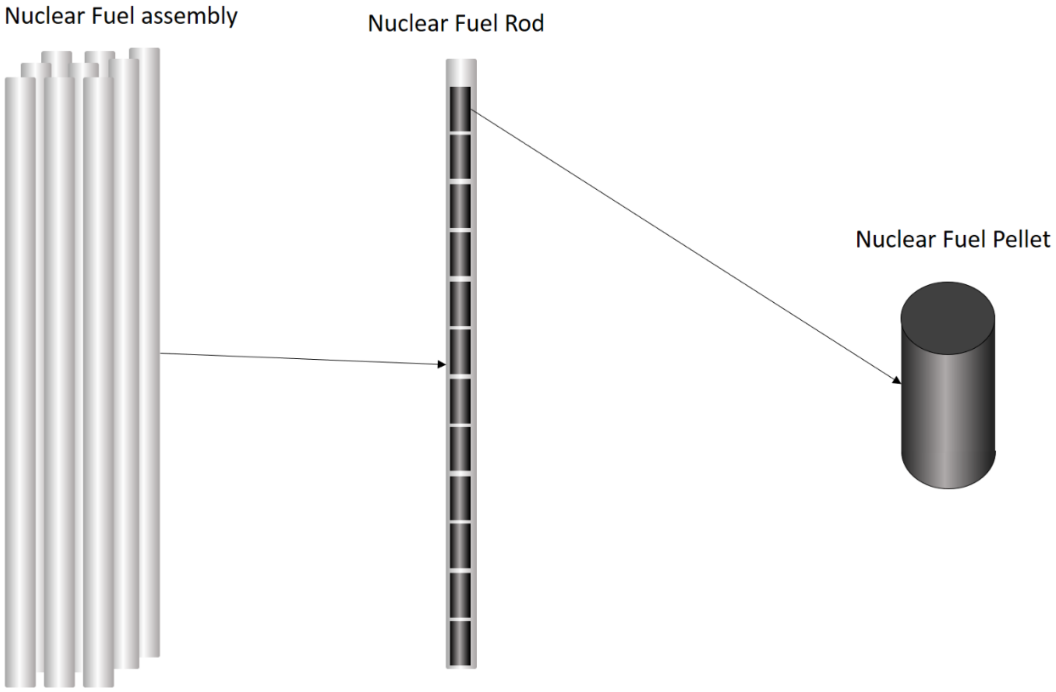

Figure 1.5 - A schematic of fuel and cladding in an assembly that contains the fuel pellets within fuel rod, with several fuel rods assembled into fuel bundle and final assembly [12]

Based on this criterion, elements such as aluminium, magnesium and zirconium-based alloys have already been applied as fuel cladding, as shown in Figure 1.6. For most nuclear power plants constructed currently, zirconium-based alloys are the chosen option for the nuclear fuel cladding material, primarily due to their performance.[20] The primary reason for cladding material selection is not simply based on the neutron transparency, even if it is one of the most important requirements for making nuclear fuel cladding, as there are other factors that need to be considered during the material selection. One of these factors is good mechanical performance which includes high strength, toughness, suitable hardness, creep resistance, a high working temperature and ideally a high radiation damage resistance. A secondary equally important factor is the resistance to corrosion because water acts as both moderator and heat exchange agent in most nuclear reactor designs. As a result, the chemical environment in the nuclear reactor can be changing and complex, which can create a highly reactive and corrosion environment. [21] The working environment inside the nuclear reactor is very harsh, particularly for the fuel cladding and pressure vessel. To keep the nuclear fuel and reactor safety and function in long period of time, cladding material should have the ability to resist damage and deformation during service life. Zirconium-based alloys have low neutron absorption and sufficient mechanical property to support this action in nuclear reactor as fuel cladding. The real advantage of zirconium-based alloys applied in this field are the lower levels of induced irradiation embrittlement when compared with other alloys.[21]

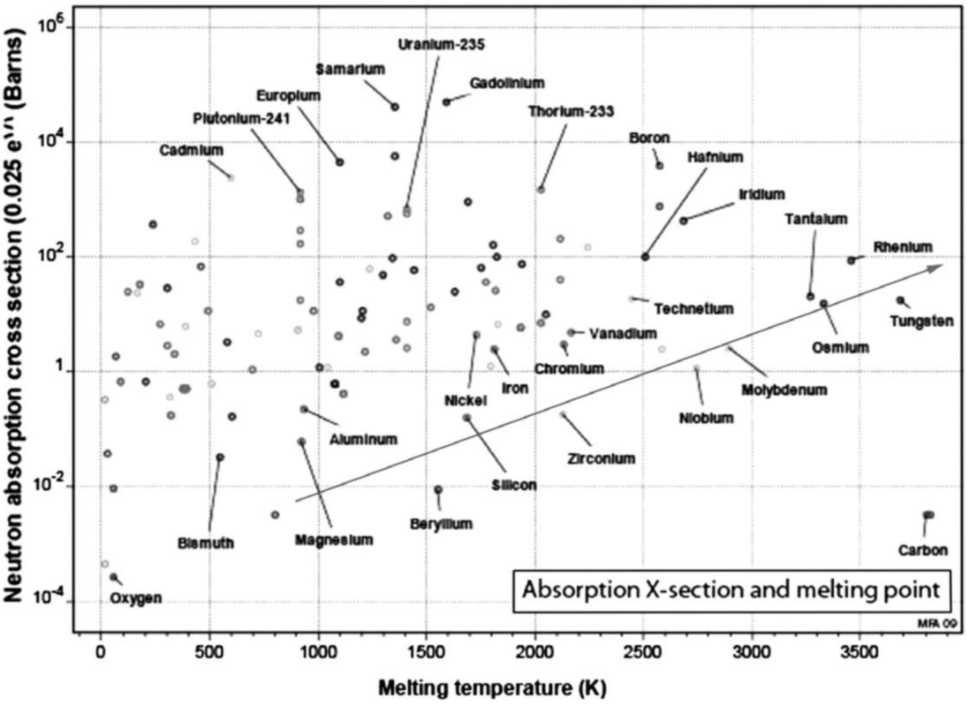

Figure 1.6 - Neutron absorption cross section against melting point for a range of elements, with both having significant effect on reactor performance [22]

However, zirconium-based alloys are not the ultimate solution for nuclear fuel cladding, because they have certain disadvantages during the service. Firstly, zirconium-based alloys can have problems from hydride formation giving rise to secondary phase formation, which impacts performance. Inside the nuclear reactor if we combine the heavy radiation and high operation temperature, hydrogen is routinely produced from water. Under operational temperatures, hydrogen gains mobility, resulting in even distribution on the surface rather than accumulated in certain areas. Thus, leading to a reduction in cladding integrity and mechanical performance. [23]

Secondly zirconium-based alloys are impacted by irradiation induced deformation leading to enhanced irradiation creep and growth, an example of this for Stainless Steel 316 is shown Figure 1.7, both highly critical to the behaviour of fuel cladding.

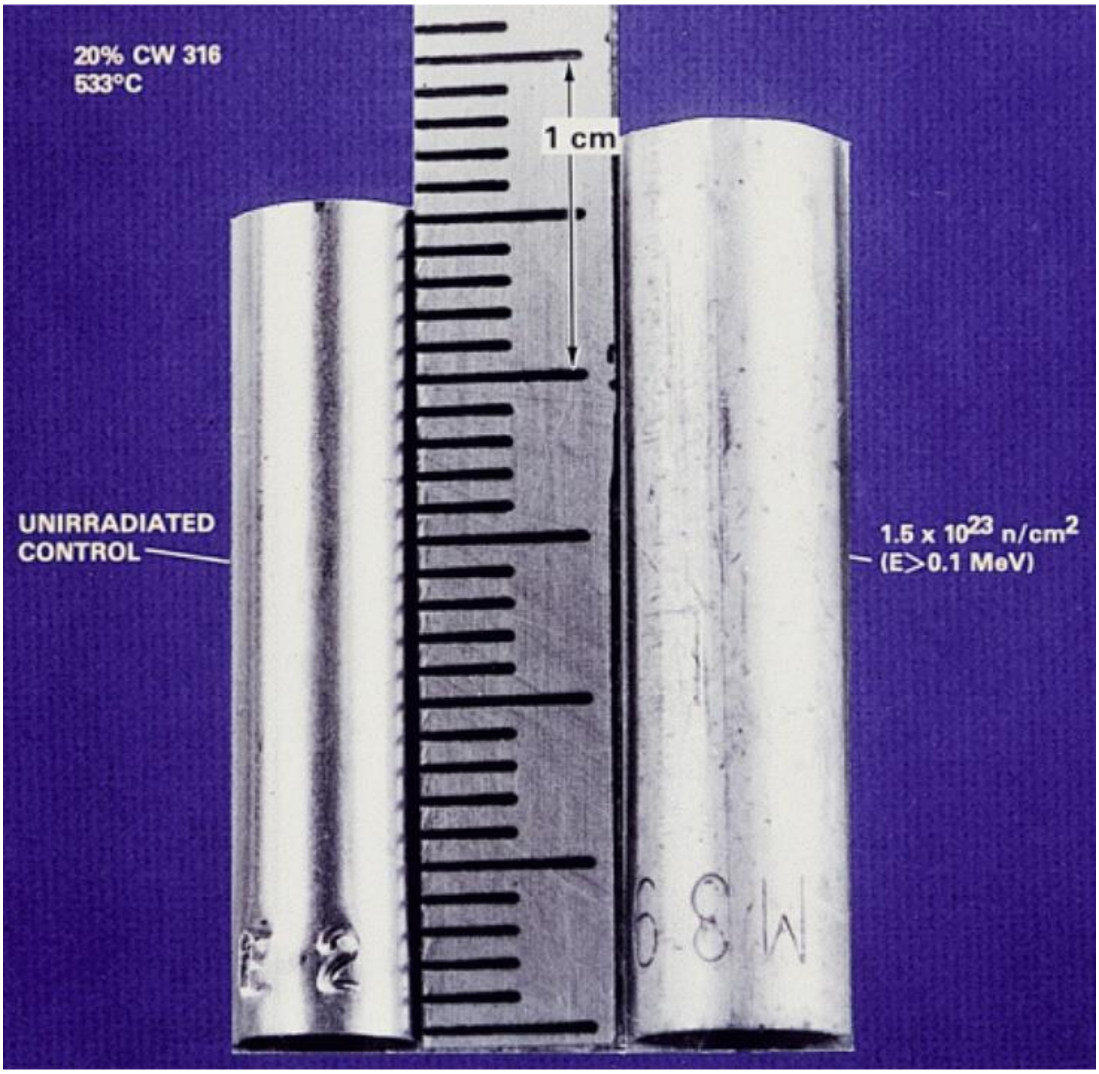

Figure 1.7 - A sample of SS316 showing the difference before and after irradiation to 1.5×10^{23} neutrons cm^{-2} which has increased its length by 12% [12]

1.8 Radiation damage

Radiation damage is a major concern within nuclear materials, and is induced by irradiation with particles, e.g., neutrons, fission fragments etc. There are two general situations that will occur when a particle interacts with a lattice atom. Firstly, if the particle does not contain sufficient energy to overcome the threshold displacement energy of the lattice atom, the lattice atom will not be displaced, although some or all energy will be transferred. The threshold displacement energy is the energy required to displace an atom from its position in the lattice. The second case is where a particle has enough energy and is able to displace the lattice atom, in many cases the primary knock-on atom will still have enough energy to repeat this process further, due to the energy not completely transfer to the receiving particle. The atom displaced by the primary knock-on atom may in turn have enough energy to displace further atoms in the lattice.[6]

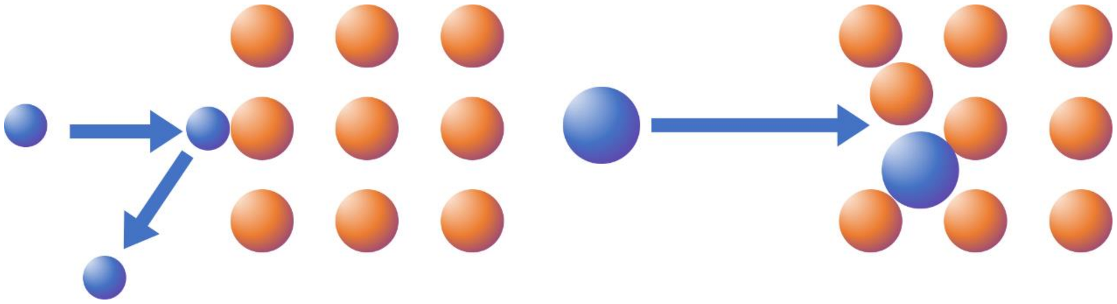

Figure 1.8 - Two situations of particle interaction, Left) lower energy collision, Right) high energy collision the kinetic energy it determined by the atom mass and speed [12]

As shown in Figure 1.8, during this process, the local atom will be displaced from its original location. The moved atom will be stopped in a location determined by interaction between the moving atom and stable lattice atoms. After several collisions and interactions, this moving atom may not be aligned with other atom, so it creates a defect. Once this defect forms, whilst it can recover, it is unlikely to recover to its original state. With the accumulation of such defects, radiation damage begins to form in the irradiated zone.

1.9 The result of radiation damage

To understand the result of radiation damage, it is important to introduce other factors such as lattice recovery. The brief description of this relationship is that the competition between radiation damage and lattice recovery, helps determine the outcome of radiation damage. Lattice recovery is the response within a lattice system when a defect is present. As outlined in Figure 1.9, within a close packed structure, neighbourhood atoms around point defect will start to move and recover from the defect to a more ordered arrangement, lower thermodynamic state, giving the system an ability to normalise the defect in many situations.

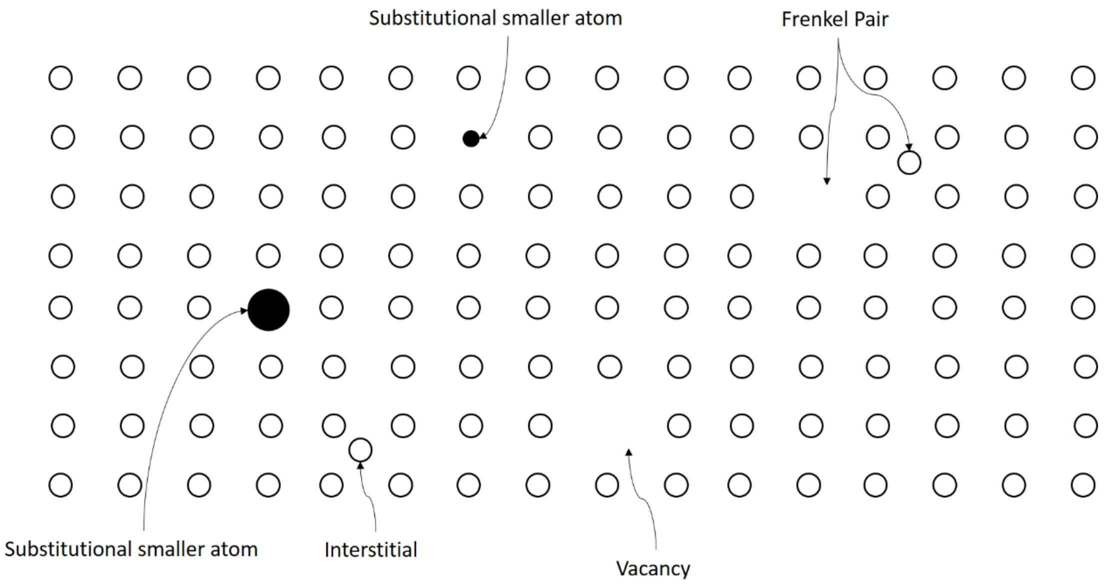

Figure 1.9 - Schematic of an ‘impurity’ affecting the local material crystalline structure reducing the consistency of the original local microstructure[2]

This recovery can include significant movement of atoms, which can be considered partially random and in turn can be altered by further radiation damage. In a nuclear reactor, the primary radiation damage is caused by neutron, and other atomic species produced from the fission reaction of nuclear fuel, which can include He particles arising from alpha decay.[24] As outlined in Figure 1.10, these particles have different energy and mass, so the damage path will be different. Higher mass particles normally cause large scale displacement within a short range, whereas lower mass particles with high energy such as neutron and helium ions will tend to displace over a longer range. The first type of damage pattern is known as direct impact, the second one as defect accumulation. The variety of damage mechanisms and recovery process makes damage difficult to predict across various alloy systems, as the composition and microstructure will lead to changes under irradiation.[25]

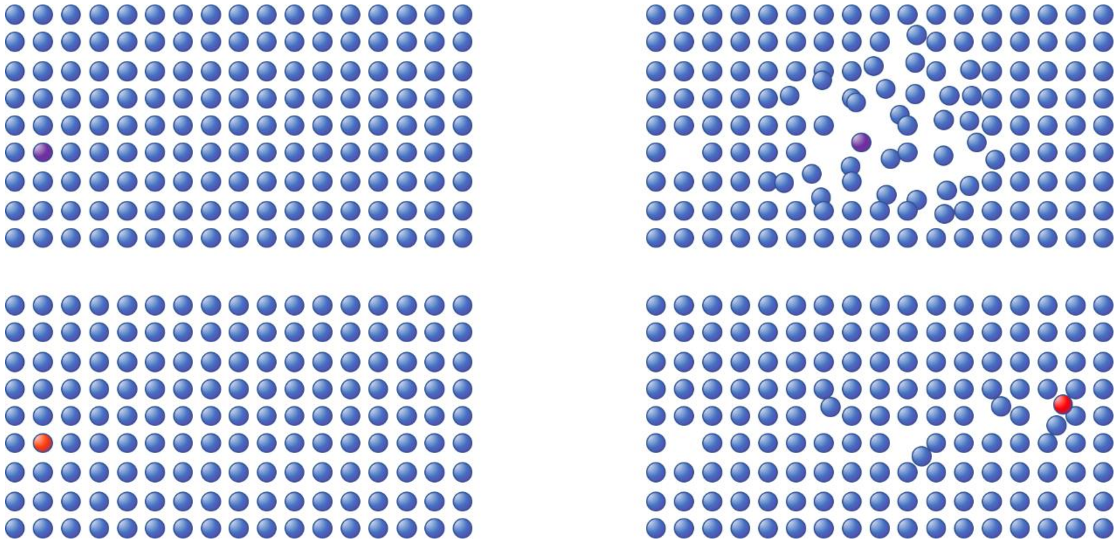

Figure 1.10 - Two results from different mass on insert atom, (Top) direct impact. (Bottom) defect accumulation, which is result of different types of interaction [12]

The lattice recovery rate is affected by many factors, with temperature being significant. Increasing temperature will increase atomic migration, thus speed up the recovery process. Atomic scale defects such as elemental change, arising from transmutation, can influence the lattice recovery rate, and is related to properties such as atomic species, electro-negativity, lattice structure etc. [6]

1.10 The bulk effects of radiation damage

Any microstructural change can impact the macro properties of a material. During the accumulation of irradiation damage, the microstructure in a radiation affected zone will be significantly modified. Therefore, in this area the bulk physical properties will also change. Consequently, due to the uneven distribution of irradiation, the localised physical properties change can lead to material failure including expansion, embrittlement, cracking, segregation and thermal conductivity change etc. [26]

Expansion is one of the most obvious geometrical change and most common result in all bulk effects. As shown previously, the dimensions can increase. There are three main mechanisms behind this geometry change. First is the formation of vacancies or other point defect. With radiation damage building up, this introduces residual stress and strain into the material. This is found most commonly in metals. Vacancies are atomic scale in nature and induce a change in both density and volume. With this reduction in density under irradiation the arrangement of atom will altered in many different ways. As an example, most single crystals will be become damaged, leading to amorphization, after experiencing irradiation. A second cause is the formation of gas bubbles, arising from nucleation of gaseous atoms within the lattice, for example helium, which comes from the charged neutralised alpha particle. Helium gas bubbles form when they nucleate together.[24]

For material applications within nuclear cores changes in bulk properties are crucial and may directly impact the function of the reactor core. For example, reduction in thermal conductivity has been observed in many materials such as SiC, due to the damaged lattice structure losing efficiency of heat transportation. The loss of thermal conductivity will reduce the heat transfer leading to accumulating heat, leading to possible melting. Embrittlement is another hidden effect arising from damage processes. Many materials will become more and more brittle or lose their ductility while accumulating radiation damage. Over the service lifetime of material under irradiation, it may no longer meet the requirements, in other words the designed service time will largely be shortened. This could happen in localised area rapidly and can eliminate parts quickly. Cracking could be described as the ultimate presentation of radiation damage, with crack formation indicating that the material is no longer able to handle the increasing internal stress and strain, with cracking releasing such energy. Radiation induced segregation is an obscure effect often initiated by radiation damage and tending to occur in a complex material. For example, complex alloys can start to dealloy, giving rise to formation of different phases. This segregation could significantly affect a high entropy alloy which will be described in a later section. [24]

1.11 High entropy alloys

1.11.1 General Alloys

Alloys are a metal mixture combined with other metal or non-metal elements. Alloys can produce differing characteristics to serve different purposes. [27] Normally alloys can operate for longer when compared with single element metals, and with modem development, the metallurgical nature of alloys makes it easy to produce and process. With developments in chemistry, more and more elements have been identified and purified, providing a wider range recipe for alloy making. For an alloy, the properties can be altered by slight change of the component of original recipe. However, all this process needs to be done under highly controlled environments. The amount of added element needs to be very precise, and the impurity should be removed completely to ensure the resultant alloy gaining desired properties. An example of a nuclear related alloy is ZIRLO from

Westinghouse.[28]

1.11.2 Definition of high entropy alloy

A high entropy alloy is an alloy system which is significantly different from a conventional alloy system. It is important when giving a definition of high entropy alloy to identify the boundary between a high entropy alloy and other alloy. With research and developing some of the basic concepts about high entropy alloys have been reviewed. As shown in Figure 1.11, there is no significant sign of surface property which indicate a difference between a high entropy alloy and conventional alloy.

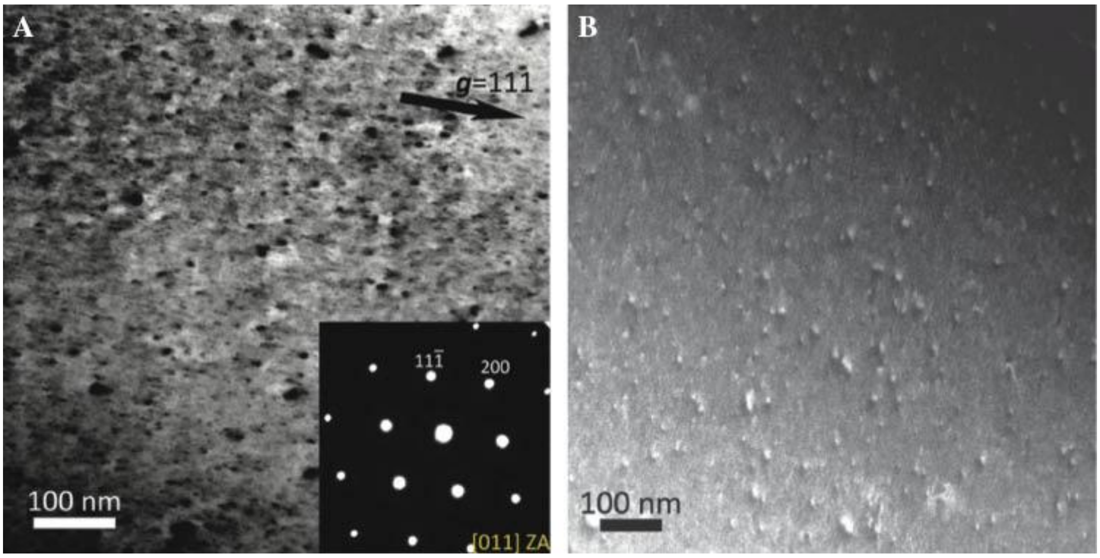

Figure 1.11 - A TEM image of a uniform high entropy alloy. [29]

There are several definitions that can be used to describe a high entropy alloy, with no single overwhelming one used. The definitions cover multiple areas and try to give the best description of high entropy alloy. For example, the most common definition is given as ‘an alloy system containing five or more principal element with equimolar ratios.’

This indicates a high entropy alloy system should contain multiple elements and that each of them should have similar compositional fraction in the final product. [30] However, this definition is not complete. For example, to modify the mechanical properties, the composition of each principal element can be varied between 0.2~5 atomic ratio. The term ‘high entropy’ therefore indicates the amount of entropy, or disorder, contained within the alloy. As a consequence, another definition quantifies the total configurational molar entropy in an ideal single-phase into low (below 0.69R), medium (between 0.69R and 1.61R) and high (above 1.61R) (where R is the gas constant in the Boltzmann equation).

[31] The main concern with this definition is that the Boltzmann equation is itself based on an assumption that the ideal single-phase is itself in order, which is not commonly found in metallic solutions. There are several other definitions to describe high entropy alloys but most of them cannot fully cover all the properties of high entropy alloys. From those definitions, the high entropy alloy can be summarised as a multiple element alloy system with certain mechanical performance, linked to the highly random orientated lattice in either the single-phase or high entropy state. [32]

1.12 The core effects of high entropy alloy

1.12.1 High entropy effect

The high entropy effect is the most important characteristic of high entropy alloys and one which defines the term ‘high entropy’ and enhances the formation of a solid solution. If one follows the traditional physical metallurgy concept, then multiple existing segregated phases and more than one compound system are not only hard to analyse but can also be very brittle. However, in a high entropy alloy which has a solid solution one would normally form one equilibrium stable phase with the lowest free energy. The lattice adopted could be BCC, FCC or HCP, with BCC and FCC being the more common lattice structures. A high entropy alloy has a random distribution of all elements which directly reduces the system enthalpy and significantly reduces the intermolecular free energy. [33] As outlined in Figure 1.12, with the number of elements increasing, the mixing enthalpy for the completely disordered state for an alloy system is closer to the completely ordered state. As substances prefer to shift into more disorder, i.e., increased entropy and lower enthalpy, the multi-component and highly random system is stabilised especially at high temperature. There are multiple factors that can affect the composition of a high entropy system, such as the large difference in lattice bonding energy between each element, the atom size difference and adding repulsive element to the rest of other components. These factors all lead to a similar consequence that encourages formation of secondary phases or forming elemental enriched phases. As a result, the material is more order oriented and gains mixed enthalpy. [34]

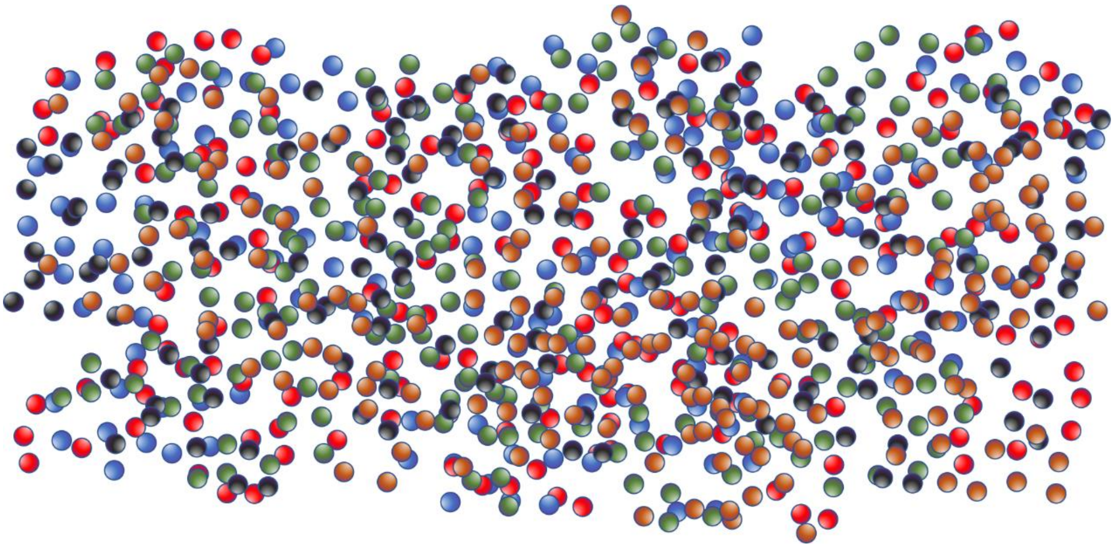

Figure 1.12 - Schematic of atoms distributed inside a high entropy alloy [35]

1.12.2 Lattice distortion

Due to the highly random distribution of component atoms within high entropy alloys, it leads to a range of differing sized atoms occupying each site within the lattice. As shown in Figure 1.13, these atoms have differing sizes and electronic configuration, so both binding energy and bond length are different. Therefore, the lattice no longer forms a regular shape but is now distorted.

These changes not only increase the hardness and strength but also reduce the effect of temperature on them. Moreover, thermal conductivity is also reduced by such lattice distortion arising from the disordered nature of connections within the lattice. [36] Generally it is found that most physical properties found in high entropy alloys are broadly insensitive to temperature change. [37]

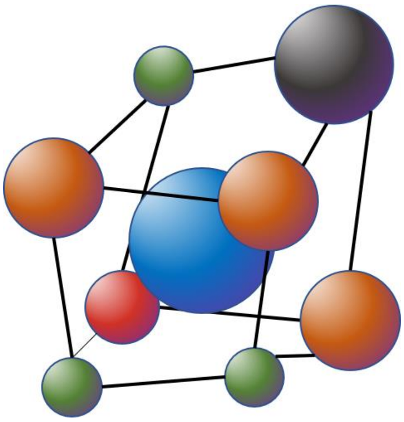

Figure 1.13 - Schematic of a distorted BCC crystal cell, it maintains the geometry relationship of atom on the each site of crystal cell but the distance between each atom is difference due to the size of atoms [38]

1.12.3 Sluggish diffusion

The formation of new phases within high entropy alloys generally requires significant atomic diffusion. In such a solid solution system the arrangement of atoms is significantly different from that found in a conventional alloy. In this system, atom diffusion will be slow as it will experience constantly changing activation energies for migration from one location to another, each one with a different local atomic species. A vacancy or low lattice potential site can thus trap a diffusing atom, leading to sluggish diffusion. [39] As described in Figure 1.14, the degree of this effect is directly affected by the number of elements involved within the alloy composition, the more of the element the larger the effect. This property can impact phase nucleation, growth and distribution, there are several potential advantages of having this impact on microstructure, such as forming supersaturated states and finer particles. Based on this type of grain structure and distribution, the macro property of the material could be high creep resistance. [39]

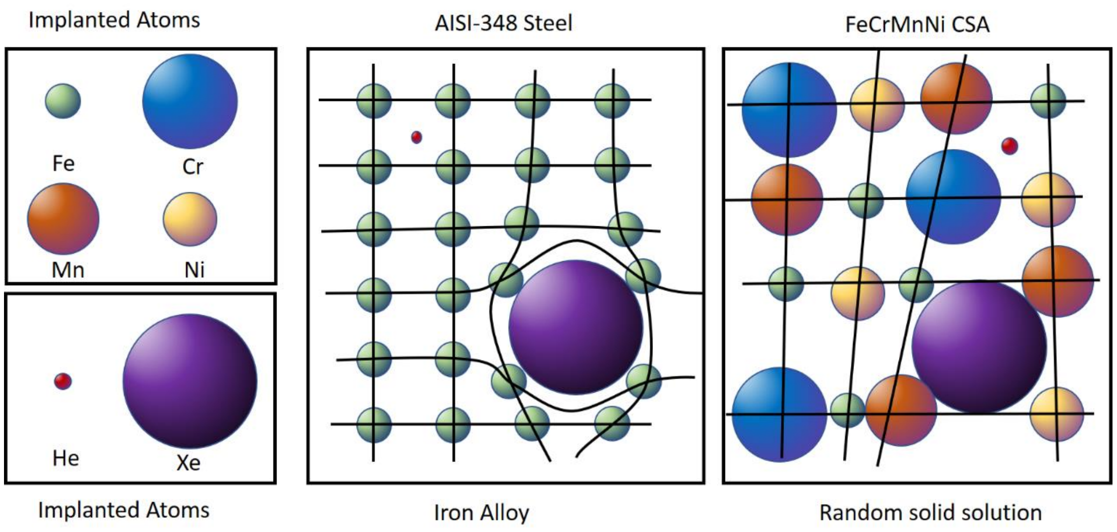

Figure 1.14 - Schematic of the differences between a material with and without a slow diffusion rate when an alien atom is insert into the material system [40]

1.12.4 Cocktail Effect

This effect arises from a high entropy alloy with five or more elements having a constituent phase which is constructed from all other possible phase existing in the alloy, and links with phase properties such as size, shape, boundary etc. Each single phase has various elements with slightly different composition on atomic level, leading to the properties of this phase being different from other phases. The final properties of this constituent phase are a combination of the general mixture of elements and the induced lattice distortion. Therefore, this cocktail effect has many influences, mainly on the atomic level microstructure.[41] When combined with other effects, the high entropy alloy system is able to manipulate not only the mechanical properties and high temperature performance but also magnetic and electrical properties.[42] The cocktail effect is an iconic characteristic of high entropy alloys, but the result is not always positive. The cocktail effect arising from the atomic level microstructure means a slight composition shift will impact performance of the material, as many of the properties of a material are decided by the microstructure. Therefore, it brings more challenges to both alloy design and synthesis, as Figure 1.15 shows. Accordingly, these effects can make it difficult to predict both properties and performance of new developed high entropy alloys.

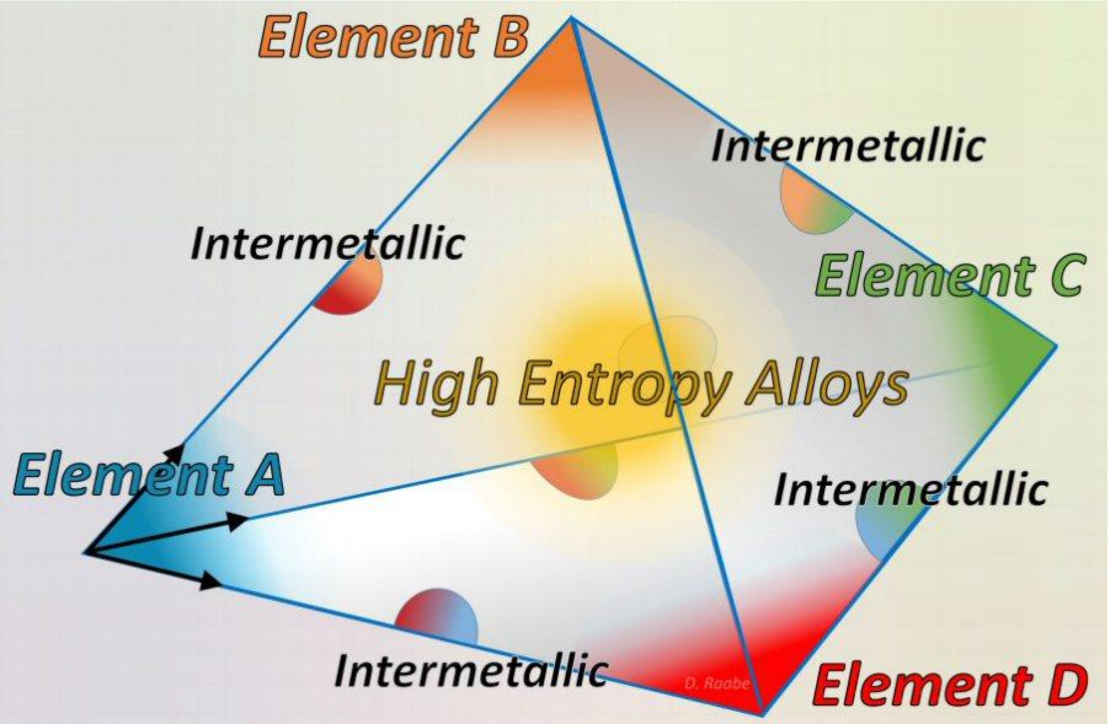

Figure 1.15 - Schematic of a phase diagram for a simple high entropy alloy, due to the nature of the elements this phase diagram inevitably becomes 4D in nature which significantly increases the complexity of this novel alloy system [43]

1.13 Evaluation of the core effect of high entropy alloy

Recent research on high entropy alloys indicate that four major factors need to be verified. For a high entropy state, most research is focused on the as cast state high entropy alloy samples, some of which are not in the high entropy sate. [36], [43] The characteristics of high entropy alloy samples can therefore become difficult to exam. During testing of high entropy alloy the different solid solution and inter molecular phases both have played important roles in the overall properties. For lattice distortion, there is less past research when compared with other testable properties. The main reason is that this characteristic is difficult to test and easily modified by other properties.[44] For sluggish diffusion, more detailed data shows that the diffusion rate of particles in high entropy alloys is lower than the average diffusion rate. However, the diffusion rate does not fall into lowest material group. [45]. In all four factors, the cocktail effect is the only one that is easily determinable. Therefore, this unique factor is a fundamental of this new alloy system and requires further research.

1.14 The mechanical and chemical properties of high entropy alloys

The physical properties of high entropy alloys are different from a traditional alloy. A traditional alloy generally has one element as its basis, with one or more other elements added to modify the lattice and phase distribution to alter the chemical and physical properties of final alloy produced. Modern alloys have been developed, that work under extreme conditions for example, turbo-jet engines. However, with the number of additional elements added, the mechanical property of the alloy tends to be more hard or brittle and loses ductility. [46] The explanation is complex and is based on the contribution of randomly located secondary phase particles and increased shear energy on the lattice plane. On the other hand, high entropy alloys have different trends when compared with traditional alloys, for example with specific size, shape and distribution of phases, high entropy alloys can gain balance between strength and ductility. The dendritic formation of various element rich phases is broadly found in most of existing high entropy alloys which is a highly distinguishing characteristic and an indication of a high entropy state. [47] This solid solution-based alloy has extraordinary mechanical properties such as strength and toughness, keeping these properties up to high temperatures. The lattice structure for a high entropy alloy is normally FCC or BCC. In some types of alloys however, both of them can be present dependent on the thermal path used in formation. Alloys with a BCC structure show significantly higher hardness, even for a joint BCC/FCC structure, with increasing hardness with BCC content. [48] Other microstructural features such as grain size and element rich phase orientation, can significantly modify mechanical properties, but these can also be altered by thermal treatment. Generally, a high entropy alloy normally has good corrosion and oxidation resistance due to elements such as nickel and chrome which can enhance the formation ability of passivation film on the final product. [49]

1.15 Nuclear reactors and high entropy alloys

Within a nuclear reactor, it not only commonly has extreme high temperatures and pressures, but it also has extreme radiation which can significantly impact a material’s microstructure. Next generation nuclear reactor designs also bring new challenges and higher requirements in the use of materials, with increased temperature inside reactor and new coolants with increased corrosivity. These increasing requirements are approaching the limitation of conventional alloy. Therefore, future nuclear reactors require new materials such as silicon carbides which have great potential to be applied in TRISO nuclear fuel as cladding material. [50] High entropy alloys, as outlined previously are relatively new, and can have dramatically different properties from conventional alloys. The strong mechanical properties at high temperature and reasonable corrosion resistance make the high entropy alloy an excellent prospective material.[51] The strong performance under high temperatures shows great potential for use within in nuclear power core, as cladding. However, to be applied, there is more required than just strength and hardness. The final goal of this project is to examine the radiation damage and recovery which is a key criterion before application within high radiation environments. By determining if high entropy alloys have enhanced recovery properties, it can verify that high entropy alloys might be applied as fuel cladding, as such this is the main focus of this project. The mechanical properties at high temperatures for high entropy alloys are excellent, which can provide more capabilities for the next generation of high temperature nuclear power plant design. Also, with enhanced corrosion resistance, a high entropy alloy could better handle the crucial corrosion environments in new reactors, such as the molten-salt and liquid metal reactors. Therefore, the evidence that high entropy alloys can keep their characteristics and properties under high irradiation will highlight the potential within the nuclear industry. There are several different benefits which including lower running cost, longer service life, higher safety standard and etc, that will reduce the total cost of generation per unit of electricity and make the nuclear power industry more profitable. The successful application of these types of material will not only be able to significantly boost the development of fission nuclear power plant, but also can be a technology solution for the controllable fusion power plant construction.

When it comes to the application of high entropy alloys in the reactor, there are various scenarios which need to be discussed individually. The nuclear fuel pellet containing the fissile fuel is not ideal for applying high entropy alloy, as during fission the induced damage and fission will significantly change the composition. Also, the enormous amount of heat will easily melt the nuclear fuel in alloy form. This outweighs the benefits from increased heat conductivity compared to the current ceramic fission fuel pin, so is therefore unsuitable. Nuclear fuel cladding, containing the nuclear fuel, is a possibility, however. Nuclear fuel cladding, outside the fuel itself, experiences the highest rate of irradiation, inside a fission reactor. It suffers from irradiation damage but is also required to maintain its shape and function during its entire service life. It may seem an ideal application for high entropy alloys but, the design of nuclear fission fuel cladding requires the material to have very a low neutron absorption cross section. This requirement arises from the need to allow neutrons to transfer between fuel pins, enhancing the performance of fission. The current material used in fuel cladding is routinely based on zirconium which has a very low neutron absorption cross section. However, it is very difficult to develop a high entropy alloy to have such low neutron absorption cross section, as there are very few elements that have low neutron absorption cross sections, and which can be used in a high entropy alloy. One of the most important applications of nuclear fission reactor is the reactor vessel. The reactor vessel itself is far from the radiation sources, as the majority of the radiation is shielded by the moderator and other fuel. Therefore, the main design requirement for the material used in the fission reactor vessel is the classical mechanical properties such as strength, toughness, density, cost etc. Across all these, cost will be the main challenge for a high entropy alloy to be applied as the reactor vessel. Based on the current research, the synthesis of high entropy alloy needs pure element material to ensure the correctness of the composition and the performance of the product, which increases the cost of high entropy alloys. In order to make such a large structure, it will require large pieces of material formed into the designed shape to reduce wastage. However, this process is not ideal for the current high entropy alloys, as the effect of large-scale deformation of high entropy alloy is not identified yet. Therefore, the conventional alloy like SS316 or SS304 is more suitable applied as reactor vessel. Apart from the components mentioned above, the rest of the parts like support structure, control parts and maintenance parts are more suitable for applying the high entropy alloy. Dependent on the high entropy alloy be applied, the elements involved in the produce alloy will be different. For making bulk material, the elements used will tend to use cheaper element such as Fe to control cost. For making coatings on existing material, the elements such as W and Hf could be used. Those elements will give better performance on both chemical and physical properties. Also fabricating high entropy alloys as a coating will significantly cut down the cost and avoid the challenge from over processing as well.

1.16 Advantages and disadvantages of using high entropy alloys within nuclear applications

In summary, the material property requirements for next generation nuclear reactors, such as Gen IV, include excellent mechanical properties, high corrosion resistance, high heat conductivity, long service time and ability to retain such properties under high temperature. Based on the current existing research, high entropy alloys have the capability to meet most of these requirements but applying high entropy alloy is more than just selecting a suitable material. High entropy alloys have extraordinary mechanical properties compared with most current used material in nuclear reactor. They could allow the nuclear reactor to be designed with higher primary power output and can potentially improve safety of core components. Furthermore, high entropy alloys can normally keep high mechanical performance under extremely high temperature. This could enhance further the safety of the nuclear core by reducing the risk of a containment breach. Higher capacity in withstanding high temperatures and pressures could increase the energy output and energy efficiency of reaction core, but more likely leave room for safety buffering. Increased corrosion resistance is one of the most important properties required by the next generation of reactors, as salt mixtures or liquid metals selected as new moderators and coolant, can lead to devastating corrosion of conventional alloy. Thus, high entropy alloys are strong candidates for the next generation of nuclear reactor design, not only as the material meets the required properties but also gains balance between each of them.

High entropy alloys also have shortcomings for applications within nuclear reactors. Firstly, the cost of high entropy alloy is high. As the alloys are continuously being developed, they do not commercialise well, which means a reactor prototype will cost more using high entropy alloys. However, after commercialisation high entropy alloys will still be optimal in many conditions compared with other conventional alloy. [52] The synthesis of high entropy alloys has many challenges which require the product to have a uniform solid solution. Due to the nature of high entropy alloys, the composition of each element within the alloy needs to be verified several times before it forms a stable high entropy state. Moreover, the thermal path for synthesis needs to be carefully adjusted to guarantee the desired microstructure. From the mechanical side, if a material is hard, tough, and strong etc. it can have ideal mechanical properties, but it also means the processing of this material is very difficult. A last but not least disadvantage is radiation induced segregation, as mentioned before, segregation normally occurs in a complex system which high entropy alloys are. During service within the nuclear reactor, dealloying could occur in many places on parts which could lead to modification of mechanical properties and fatigue, leading to fatigue failure.

1.17 The synthesis of high entropy alloy

Several fabrication methods of making high entropy alloy have been developed in recent research which capable of making qualified one. One of the popular methods applied is based on the classical melting and casting route. This route simply casts the molten mixture into ingots. Although there are many options able to melt the metal ingredient into liquid state such as burning furnace, electric furnace, induction furnace and electric arc furnace. Each of them has different characteristics and properties when melting any content in the crucible. [52]

Figure 1.16 - An air burner furnace, with a pool of molten metal.[53]

As shown in Figure 1.16, the burning furnace is a very traditional furnace which burns various fuels including methane, carbon monoxide to provide a sufficient temperature for melting the metals. The fuel is normally gas, but some older designs burn coal or fuel oil. This equipment is very cheap compared to others, but the downside is also significant. The biggest problem with this method is the introduction of extra oxygen. Direct burning is not able to generate enough temperature, so a high-speed gas jet or oxygen is applied which will strongly impact the melting and mixture process.

An induction furnace, like in Figure 1.17, uses a strong magnetic field to induce eddy currents inside the target material, generating heat. However, it requires the target material to have sufficient mass to be affected by the applied magnetic field. For small scale scrap material melting, it is not ideal for example. However, induction furnaces are one of the gentlest methods to melt and mix the sample. With the assistance of vacuum chambers, it can provide delicate control on the element composition on the final product. [54]

Figure 1.17 - AFI-06 induction furnace purposed for small batch sample making [55]

Figure 1.18 - Arc 200 arc furnace which can produce over 3000˚C for making high malting point sample [56]

An electric arc furnace, as showing in the Figure 1.18, using high voltage electrodes to create high power arcs can penetrate all material in the arc path and melt them. The process runs under low pressure and protective gas environments, providing better arc formation and protecting the material from oxidation during the melting process. The electrode is not necessary to be in contact with material, the arc will find the shortest path to the other electrode. To maintain conduction between electrode contact and material, and prevent it melting by high temperature, the crucibles are generally made of copper and water cooled. Although small amounts of lower melting point metals can evaporate during the process, this method is ideal of making small test portion of alloy. After the mixture has melted and is fully mixed, the alloy formed is in a liquid form, and can be cooled into an ingot.[57]

Figure 1.19 - Simoloyer® CM01-2l high energy ball milling with vacuum or inert gas protection [58]

For more advanced synthesis, there is laser-engineered net shaping, assisted with high-energy solid-state synthesis or spark plasma sintering. This is a combined process, with the material powder prepared for high entropy solid state synthesis and shaped by laser-engineered net shaping. The high entropy solid state synthesis is a vacuum ball milling system, similar to that shown in Figure 1.19, which is able to apply sufficient energy to the fine powders through milling to enable them to join. The alloy formed at this stage is a very fine powder form and requires the process to be carried out under inert gas protected conditions. [59]

Figure 1.20 - Plasma assist powder 3D print technology, the pre-prepared material powder is spread while the plasma heating the working area [60]

As shown in Figure 1.20, laser-engineered net shaping is an application of additive layer manufacturing capable of fabricating larger pieces of high entropy alloy through injecting material powder into the target area and using a high energy laser to melt. Compared to normal additive layer manufacture, the products from laser engineered net shaping are much denser in texture. [61]

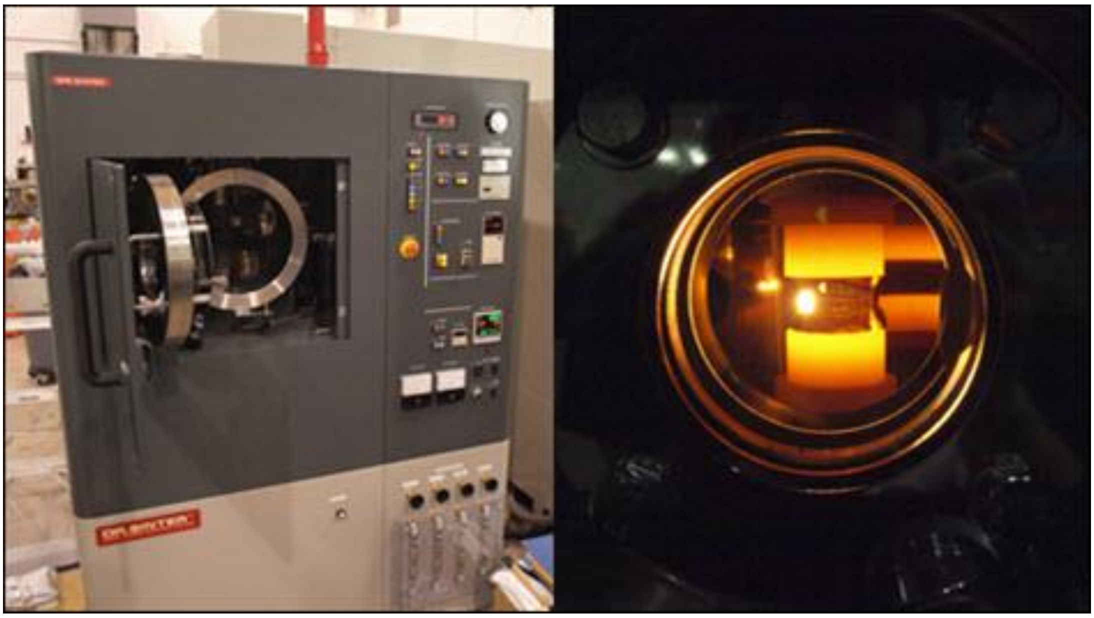

Figure 1.21 - The spark plasma sintering can provide over 2000°C to make a very regular shape sample [62]

The final option is a spark assist pressed die system which applies electric current though metal powder to generate heat, and shapes the material with press die. Such a device is shown in Figure 1.21. During this process, the material powder does not melt, but slowly deforms and sinters together. Under vacuum controlled environment, the material can be protected from oxidation. The resulting product has very low porosity and uniform distribution of each component. [63]

1.18 Heat Treatment

Heat treating is a process whereby the target material is heated in a series of heating/cooling cycles to alter the microstructure and achieve the desired mechanical properties. Heat treatment is very useful during high entropy alloy synthesis, as it increases the uniform distribution of elements. Annealing is a common heat treatment that can release the residue stress and unify the element distribution of the material. Various heat cycles have different effects on the final properties obtained, as there are many parameters that can be varied. For example, annealing can have different temperature ramp up and down times, holding temperature and holding time etc. Therefore, the most suitable thermal cycle of one material normally requires multiple attempts.

1.19 The verification of high entropy alloy behaviour after irradiation

As mentioned earlier, the main focus of this project is to verify the behaviour of high entropy alloys after they have been irradiated. Some high entropy alloys have been shown to recover from damage after experiencing relatively small amounts of atom displacement. [32] This process matches the initial expectation, that as the already disordered solution has a randomly distributed lattice structure, a slight shift of atoms is not expected to dramatically change the overall lattice structure at such low levels of damage. However, for the working parts in the nuclear reactor, the displacement per atom (dpa) experienced during the service time will easily pass 100 dpa, possibly even reaching 200 dpa in some designs like lead fast reactor. [33] Because of the nature of high entropy alloy, there are two main concerns with it experiencing large doses of radiation. First is radiation induced segregation, as it is possible that after long periods of irradiation the high entropy alloy will start to form an ordered lattice structure and lose the high entropic state solid solution. The second concern is implantation itself. Radiation within a nuclear reactor is powerful involving light particles like neutrons and helium nuclei, and heavy particles such as fission and decay products. These will not only be causing damage to the material but will also insert extra elements into the material. Based on the cocktail effect of high entropy alloy, such radiation damage can lead to unexpected composition shifts at the atomic scale. The result of this type of shifting can be hard to predict. When coupled these give the project two requirements in experiment design, the first is that the irradiation time is long enough to allow the specimen to receive large doses of radiation, whilst give time for recovery processes to take place. The second is the ion source for the irradiation should be heavy and the energy of irradiation should be high. This is to guarantee the result of radiation damage is obvious and can enhance the difference between damaged and undamaged sample, whilst also achieving a level of damage as close to the actual service result as possible in a short period of time.

1.20 The critical recent work on high entropy alloy

In recent times, there has been increasing research on high entropy alloys. From when high entropy alloys were discovered and identified as a new the alloy system, their special characteristics have attracted a lot of attention. For many years of research, more properties of this new material has been discovered. According to the Xiang, C. and Wang, J's research, the corrosion resistant properties of the raw material elements will affect the final product alloy. [64] This research indicates that those elements, which will form dense oxidation layers, enhancing corrosion resistance, will increase the oxidation resistance property within the final alloy product. This phenomenon seems positive when related to the numbers of those element added in the alloy recipe. However, such properties do not always give the high entropy alloy superior corrosion resistance performance compared to a conventional material. D.B.Miracle's research has more discussion on the definition of the high entropy alloy itself.[43] After many years of research, high entropy alloys still lack understanding and require more research, with past research often having problems on the sample synthesis with some unable to produce qualified sample with sufficient distribution of element. The synthesis of high entropy faces two main challenges. One is that some transition metals naturally bind together, which makes it harder for other elements to mix. The solution is to further mix the alloy until it is fully mixed. However, it can lead to another other problem, that being long term heating can cause some elements to evaporate. This can arise when the material is melted inside a vacuum crucible and the temperature exceeds 1500˚C. At this temperature and low pressure, some of the low melting point elements may start evaporating and leave the crucible, reducing the amount inside the final alloy product. High entropy alloys are high reliant on the equilibrium of the element portions, meaning a lack of some elements will modify the formation of high entropy state. On the other hand, use of physical vapour deposition (PVD) is able to produce qualified high entropy alloy, but due to the nature of PVD it can never provide a large enough sample to perform larger scale experiment. In addition, estimating the high entropy state of high entropy alloys is very difficult. It is unknown which main factor within elements contribute to the high entropy state in the final alloy product. According to Jin, K. and Lu, C.'s research, the higher the number elements in alloy the higher the resistance to irradiation. [80] In this research, samples are divided into 5 group which have 1, 2, 3, 4 and 5 elements in each of them. Irradiation induced swelling is smaller in alloy with higher element alloys, for 5 element samples, same as a high entropy alloy, there is extremely low swelling compared to other groups. This indicates that high entropy system is able to resist the volume change leaded by the irradiation.

Chapter 2 - Experimental Methodology

2.1 Experimental Design

The aim of this PhD was to examine how high entropy alloys respond to ion induced irradiation damage, focusing primarily on the impacts on microstructure. The experiments are divided into four main parts: sample preparation, irradiation, analysis and comparison. Each individual phase also contains multiple steps, depending on the system being fabricated and analysed.

2.2 Material selection

High entropy alloys (HEA) have a vast compositional range, with current research indicating the majority containing transition metals, but there are more than 20 elements used [43]. Due to the 'cocktail effect' each high entropy alloy has different mechanical and chemical properties. This difference can be significant with just one element change, giving rise to several challenges in the selection of the target material. First, identifying that the material is able to represent the fundamental properties of high entropy, as the key focus of this project was to examine mechanism and capacity of high entropy alloys, under levels of ion induced radiation damage. Therefore, the target material should have the common properties of most high entropy alloys. The second challenge is one of composition, or alternatively what are the viable components within the alloys. For example, yttrium and scandium are relatively expensive, which makes production of such allows expensive, as in order to control the final product, highly purified elemental material is routinely used. Finally, for the alloy to be of use it must have good mechanical properties under high temperature working conditions. However, they are normally designed to serve practical properties such as within a jet engine, which means they may not be the ideal material for use within a reactor. Therefore, model alloys considered in this project are based on chromium, iron, cobalt and nickel. Each alloy contains at least one of these elements. For example, $Co_{1.5}CrFeNi_{1.5}Ti_{0.5}Mo_{0.1}$, $AlCoCrFeNiSi_{0.1}$, and TaNbHfZrTi, based on the work by C. Xiang and J. Wang' [64] have potential for application in the nuclear industry. CoCrCuFeNi is another selected material, previously proposed by S. Xia and Z. Wang's [65]. These compositions were chosen as they could be prepared in the facilities available and be representative of potential compositions for use within a reactor core. The element used in these compositions, such as cobalt, nickel and iron are popular when making high entropy alloys. Iron one of most used material in the current world, according to the productivity of iron, using them will significantly increase the commercial value of high entropy alloys. Chromium is also widely used in modern materials as anti-corrosion agent, potentially having benefits in water-based reactors. Aluminium, titanium and molybdenum act as stabilising agents modifying the final properties within alloy. Normally they are added in high entropy alloy to ensure a certain crystal structure or to enhance the formation of the high entropy state. Tantalum, niobium and hafnium are different elements used in high entropy alloy. These elements have very high melting point compared to another element used in this project. The higher the melting point for an element will, theoretically at least will raise the melting point of the formed high entropy alloy. This recipe was first proposed in a research of coating material on jet engine nozzle which require very high melting point of alloy. Zirconium is an ideal element for such composition to build high entropy alloy, because it naturally combines with hafnium and reduce the overall melting point to increase workability of finally alloy. The choice of these four recipes covered high entropy alloys with the most popular group of element combination, with different variations and a totally different category of element used in high entropy alloy which is much rarer. It is not only able to review the differences in experiment result within the same category high entropy alloy but also across different high entropy alloys. Therefore, the set of experiments will provide a more representative and wider observation of high entropy alloy irradiation behaviour.

2.3 SRIM simulation

Stopping and Range of Ions in Matter (SRIM) is a Monte Carlo computer simulation that can estimate various changes when a particle impacts a target material. The core programme of SRIM is Transport of ion in matter or TRIM. This programme was developed by F. Ziegler and Jochen P. Biersack around 1983 and has been updated since [66]. The focus of this software is to simulate high energy particles slowing down and interacting with the target material. SRIM is widely used in research on ion implantation, sputtering, and the reflection/transmission of ions. [67] In this project, SRIM was applied to predict levels of damage and range for each material under the various ion implantations. This ion implantation is commonly obtained using an ion accelerator which ionises and accelerates ions into matter. This interaction has essentially the same fundamental physical mechanism as radiation induced damage. Therefore, high energy ion implantation is usually applied in radiation damage research, with SRIM being used to simulate the range and expected levels of damage arising from the incoming ion interacting with the target.

When using SRIM there are several parameters that should be set up before the simulation is started. SRIM will simulate damage paths for each ion, thus more ions give rise to a higher reliability of the simulation. The first parameter is the impacting ion, which includes the element and its energy. The mass of an ion directly links with the interaction between the ion and the target. Heavier atoms with a similar momentum to a lighter atom will be slower for the same velocity and penetrate less into the sample. In addition to the energy, the angle of ion incidence is also adjustable, which allows for variation in the simulation.

The second parameter is the target material or inserted matrix. Within SRIM this process is separated into two parts: the layer thickness and composition. For the layer thickness, SRIM allows for the setup of multiple layers within the target. These layers overlay each other and can have variable thickness, composition, and density. The threshold displacement energy is referred to as the minimum energy required to move an atom from its site within a system. However, due to the large number of elements and insufficient understanding of high entropy alloy, the accurate displacement energy is difficult to estimate. Therefore, the displacement energy was set as default, which in this case was 25eV.

The simulation will produce data about the ion path, and interactions with the sample. In this project, the focus of the simulation was to estimate both the stopping range and expected levels of radiation damage across the range. This will help in locating the observation windows for cross sectional analysis of irradiated samples in the later stages.

2.4 Synthesis of High Entropy Alloy (HEA) samples

There are many technologies that can be applied to synthesise HEA. The method chosen here was electric arc melting. High purity stoichiometric amounts of the alloy components were mixed in a mill, sectioned into sample sizes and placed in an arc furnace. High purity alloy components were used to minimise where possible the formation of secondary phases. Due to the nature of the process, the materials were twice washed with acetone to remove surface contamination. Also, to avoid furnace contamination fine powders were not used. The model of electric arc furnace used in this project was an Arcast Products Arc 200 Cold Crucible Arc Melting Furnace.

When using the furnace at full power, theoretically all the material should fully melt and mix. The crucible of electric arc furnace is protected by a water-cooling system which prevents damage to the crucible during melting. As a result, the bottom side of sample is very difficult to melt due to the water cooling. Therefore, in order to make the final product as uniform as possible, each sample was melted at least twice, with the semi-product flipped over between each melting. More melting processes can be used for further homogenisation of high entropy alloy samples and adjustment of sample shape. However, the multiple melting will also cause element loss, making it difficult to control composition. To prevent the sample oxidising during the melting and cooling process the entire process was run under inert gas protection. As stated, the copper crucible is protected with water cooling, so once the arc is cut off the sample will quickly cool and solidify. After the sample is cooled, it can be removed from the chamber, with the ingots forming a shape similar to a button.

Compared to other methods, electric arc furnace has several advantages. One of them is less impurity introduced into the final product. The synthesis of high entropy alloy requires high levels of control for each component inside the alloy, thus less impurity means a higher quality of high entropy alloy. The other advantage is the lower cost of operation. It requires a solid form of material which is easier and cheaper to purchase and process. There is of course a downside in using an electric arc furnace. The most serious one is that the quality of high entropy alloy made by electric arc furnace has an upper limit, which is lower than that produced by physical vapor deposition or other more advanced methods.

2.5 Sample Fabrication for Analysis

After the initial fabrication and before the start of analysis, the cast HEA ingot was prepared into a suitable form, using sectioning and polishing.

2.5.1 Sectioning

There are multiple methods for sectioning/slicing a cast ingot. In this project, gravity saw, and electrical discharge machining or electrode erosion were employed to perform the sectioning. Each ingot was sectioned by both methods to halve the sample. Both methods can cut the ingot with as small as possible cutting slip, helping to retain the maximum amount of sample.

The gravity wafering saw is a common cutting tool in material research, and generally contains a gravity wafering saw attached to a driving shaft, diamond wafering blade and cutting fluid. During the cutting process, the cutting edge of diamond wafering blade is held constantly against the object surface. The material on the cutting area will be gradually removed as the small diamond particles contained on the blade scratch/ablate the cutting surface on the sample. The diamond wafering blade is driven by the driving shaft which can rotate with sufficient torque to overcome friction from the cutting action. The bottom part of the diamond wafering blade is submerged into cutting fluid, a lubricant for the cutting process to prevent the blade getting stuck by high friction on the cutting surface and keeping the blade cool. Beyond those basic functions, the cutting fluid has one other important role in the cutting process which is to wash away the material particle accumulated between diamond particle on the blade. The main reason is linked with the mechanism of a wafering blade. The word “wafering” indicates that small diamond is mosaiced on the blade matrix, so through the cutting process the metal matrix was slightly worn away, due to interaction with the diamond particle. This type of cutting relies on the gentle removal of material, hence accumulated material between diamond particles will significantly slow down the cutting speed. To perform a stable and uniform cut, weight can be added to increase the pressure on the cutting surface.

Electrical discharge machining is a manufacture method that is also known as spark machining or spark eroding. This technology is based on a dielectric break down when the electric field intensity is greater than the material strength of dielectric. In this project, the electrode is a wire. Compared to the gravity wafering saw, this method can make a more parallel cut which can save work later when polishing. Furthermore, this method will also apply almost zero stress on the object sample, which can be critical for sample preparation when research is focused on a few micrometres close to the surface.

2.5.2 Polishing

To obtain a reproducible surface for irradiations and observations, each sample was polished to a mirror finish. Initially the sample was ground to make two flat and parallel sides using a sequence of grinding paper P400, P800, P1200, P2000. This was then refined using 5µm, 3µm and 1µm diamond suspension lapping polish. All polishing suspensions were water based, and each sample was cleaned between each step to eliminate the effect of residue suspension. A Buehler polisher was used with the sample held in a specially designed holder applying uniform pressure, whilst keeping the sample flat. During the polishing process, a flat ruler and optical microscope were used to inspect the flatness and surface finish. Once all the samples were polished and finished, they were stored in a capsule to avoid scratching and contamination.

2.6 Experimental Work

All the prepared samples were divided into groups to preform various irradiations with different ions and energy. The group and label of each sample are shown in the table in the appendix.

2.6.1 Ion Implantation

In this PhD, various ions were proposed to be implanted into the target material, to simulate radiation damage from within the nuclear reactor core. Although the real scenario inside nuclear reactor core will be more complicated with differing species, across a large kinetic energy range, giving rise to a high dose. Three ion sources were originally selected, Ni, Au and He. Nickel and Gold were chosen as a damaging species as in these systems as they can provide a good proxy for neutron induced damage. They have sufficient atomic mass to interact and stop at suitable range within each high entropy alloy material selected and is easy to utilise on an ion beam. However, due to the impacts arising from Covid and the lockdowns, it was not possible to complete the work with Gold. Helium was selected as it is a light species, which at the end of the damage process can give rise to He bubble formation within the alloy. This provided a second process that could be investigated, gas bubble formation in HEAs. The two ion species could also be compared in the levels of damage they introduced, while having different interactions with the alloys themselves.

To estimate the degree of radiation damage from ion beam irradiation, the equation below can be applied.

$$\mathrm{dpa} = \frac{\mathrm{Vacancies} \times \mathrm{Fluence}}{\mathrm{atomic\ number\ density}}$$

Where dpa is displacement per atom, i.e., the number of times of each atom has on average been displaced within the sample. The vacancies are found using a SRIM simulation of damage, fluence is the ions implanted per unit area, and the atomic number density is the average number of atoms per unit volume.

The ion implantation is performed using an ion beam accelerator, which accelerates charged particles to high velocities which are then targeted onto a sample. The accelerator has several sections, ion source chamber, acceleration chamber, sample sitting chamber, with the entire system pumped to vacuum during operation to eliminate air. The ion source provides the ionised element. This source material is usually a solid or gas, that is ionised and then accelerated into the acceleration chamber. Inside the acceleration chamber, an electric filed is applied with the ion species being accelerated to the desired charge state and energy. These ions are then energy filtered, focused and directed onto the sample being irradiated. When passing through this stage to the sample, the beam passes through a measuring device, often called a Faraday cup, which is used to quantify the beam. In these samples, the target was masked with a protective sheet with a shaped window to allow the ion pass though. The number of ions irradiating the sample can be determined by the current generated during the implantation process.

$$\text{total ion impacting sample} = \frac{\text{the total numbers of electron pass conductive wire}}{\text{change state of ion}}$$

When ions impact the sample, the sample will become charged, arising from the +ve cation being used to irradiate the sample. To achieve an electrically neutral state, the sample will either release or absorb electrons though a conduction pathway from the sample to the metallic mount.

The Ni ion implantation in this project was performed at the Dalton Cumbrian Facility, using the Pelletron, which has a maximum energy of 5 MeV. The He ion irradiation was performed at Leonard Kroko Inc which have the maximum energy of 190 keV with Varian medium current medium energy ion implanters CF4 and A2F.

2.6.1.1. Nickel and Gold SRIM Simulations

The nickel and gold ion irradiations were set up with same energy (3 MeV) and fluence for each sample. The dose was chosen to give an appreciable depth of damage, as nickel and gold ion implantation will interact more with the samples, thus travel shorter ranges within the material. If the range was too deep, TEM analysis would be difficult due to much longer ion milling process required. If the range was too shallow, the microstructure feature of post irradiation area would be significantly affected by the geometric conditions of the sample surface. The fluences used in the implantation were $1\text{x}10^{15}$, $2.5\text{x}10^{15}$ and $5\text{x}10^{15}$ ions per cm^2, with the degree of damage being different whilst the damage depth remaining similar.

2.6.1.2. Helium ion irradiation

The helium ion irradiation setup was different from that used for Ni, to obtain wider observation windows. Multiple He implantation with differing energy, but with same fluence were performed. As shown in Figure 2.1, the energies chosen were 40 keV, 100 keV, 160 keV each at a fluence of 2x10^{16} ions per cm^2. The reasoning behind this relates to the nature of the helium ion. Helium has an atomic mass 4.002 amu, which during ion implantation, gives rise to the helium ions passing through to a much deeper penetration than the nickel. At the same time due to the relative lightness of the ion, the degree of damage will be much less. This gives rise to an observation window which is very short with observation of He damage being difficult to observe. To get round these three irradiation energies were chosen, designed to overlap the expected damage depth, making it more visible. According to simulation, the peaks of this damage were located at depths of 200 µm, 350µm and 450µm from surface. These three peaks overlap to form a larger 200 µm wide radiation damage zone which allowed for more reliable observation within a TEM or EDX in next stage.

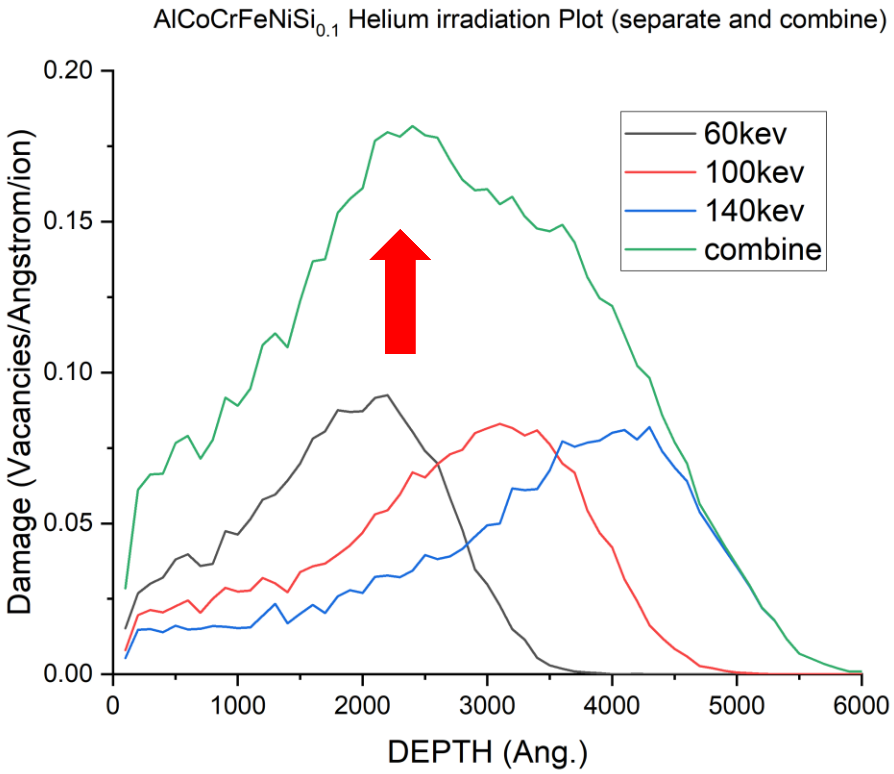

Figure 2.1- Example of helium ion implantation SRIM simulation, the special designed implantation plan creates wider range of observation the three peeks are

merged.

2.6.2 Annealing

Annealing is a common heat treatment in alloy production. The main purpose of annealing is to adjust grain size, release internal stress etc. During the annealing process, the material is held at a certain temperature for a designed time period. It will allow the atoms to relax and achieve the relative equilibrium state. For a conventional alloy, current research can estimate the resulting mechanical properties post annealing alloy through the use of detailed phase diagrams. For high entropy alloys, due to their cocktail effect a phase diagram for high entropy alloy is not simple to obtain, so it is difficult to predict either the annealing condition or post annealing result. In this project, the annealing temperature is 900 ˚C for 12 hours with additional 10 hours slow cooling. This setup is unified for all four systems. This temperature is estimated based on the melting point of each element used within the high entropy alloy being fabricated. The purpose of this experiment was to observe the microstructural shift of the annealed high entropy alloy. Therefore, it is not focused on the optimization of the resulting mechanical properties but has more focus on ensuring all the atoms have sufficient energy to diffuse where necessary. However, the annealing conditions cannot be optimised for each high entropy alloy due to the range of compositions being studied.

2.7 Sample Characterisation

Once fabricated all samples were characterised, both before and after the irradiation.

2.7.1 Scanning Electron Microscopy (SEM)

As shown in Figure 2.2, scanning electron microscopy or SEM is an imaging technology using focused beams of election to scan across a sample surface, combining the position of beam and intensity detected to produce an image of the surface. In this project the SEM is not the primary observation technique but will be combined with other examining methods to gain various data linked with the microscope image.[68]

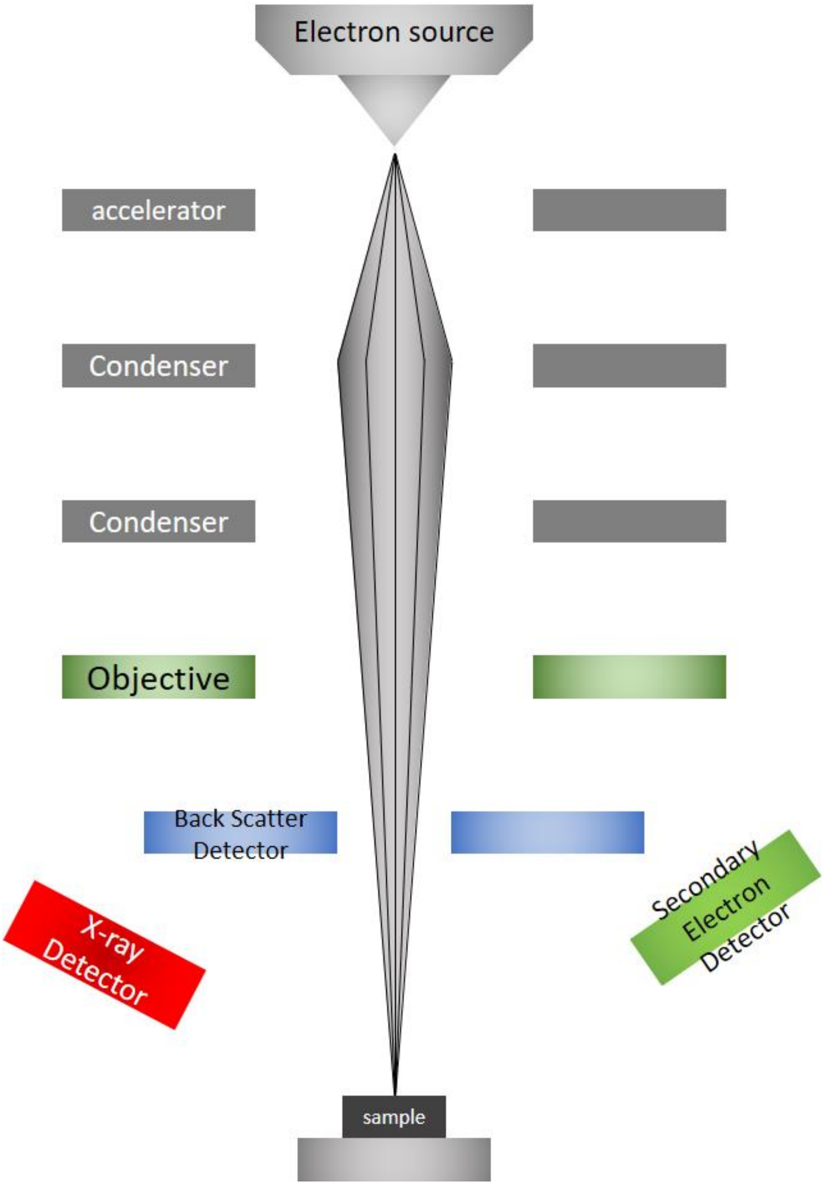

Figure 2.2 - Schematic of a Scanning Electron Microscope (SEM)

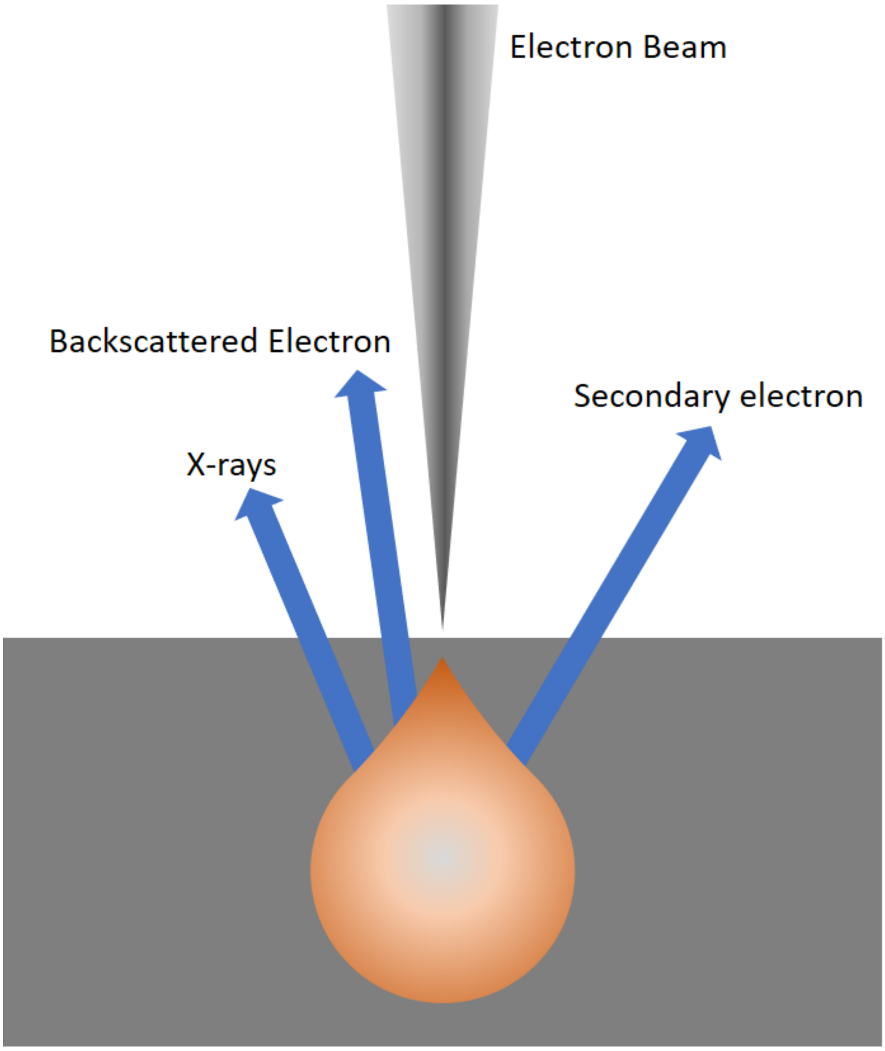

Figure 2.3 - Schematic of the relationship of major observation modes within SEM

2.7.1.1. Secondary Electron Imaging

This imaging technique uses the secondary electron ejected from the sample material which induced by the primary electron insert. As outlined in Figure 2.3, the secondary electron emission involves series complex interaction between the local atom and insert electron. Not only the secondary electron is emitted but also the characteristic X-ray which can be used to be processed as EDX analysis.

2.7.1.2. Backscattered Electron Imaging

This imaging relies on the backscattered electron which keeps significant amount of energy which is positively related to the atom mass of the element interacted with electron inserted. Considering this property, backscattered electron imaging is suitable to the observe the grain and phase difference inside material.

2.7.1.3. Energy Dispersive X-ray Spectroscopy (EDX)

Energy-dispersive X-ray spectroscopy also known as EDS or EDX is an element analysing technology. As shown in Figure 2.4, it collects various sources of excited X-ray to plot peak pattern, then identify the element by compare with standard peak pattern date base. The fundamental mechanism of this method is that each element has unique electromagnetic emission spectrum pattern due to its unique atom structure. The EDX can help determine the element content present on the sample surface. Combined with SEM, it can review detail on specific area, for example, inside the grain element composition shift. Combine the element composition data and image, it can easily determine the character of each different grain and phase. [69]

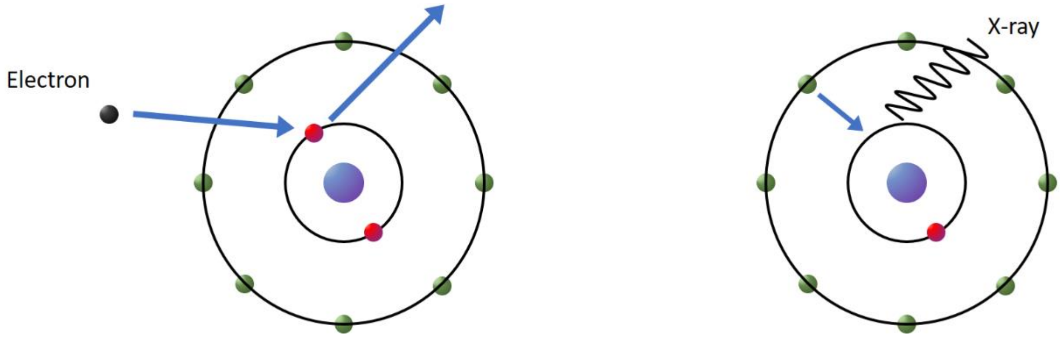

Figure 2.4 - Schematic of characteristic X-ray emission processes.

2.7.2 Transmission Electron Microscopy (TEM)

Transmission electron microscopy is also known as TEM, as described in Figure 2.5, which has electron beam transmitted through the observation sample to form image on the observation screen. Due to extremely small de Broglie wavelength of electron, TEM allows to review much more detail, even on atomic level. Using the diffraction contrast, TEM is able to detect the crystalline structure within specific spot. In this project, more advanced Scanning TEM is applied to investigate the various properties of samples. The application of the TEM has multiple reasons. First it has great amplification rate to observe the atomic level detail of piece material. Second in order to observe the change of crystalline shift along the depth change, TEM is very proper option, due to X-ray unable to reach such depth and metal is not transparency. Also, high magnification images allow element deposition to be observed such as helium bubble and implanted ion accumulation. The detailed image can act as direct evidence of experiment result.[70]

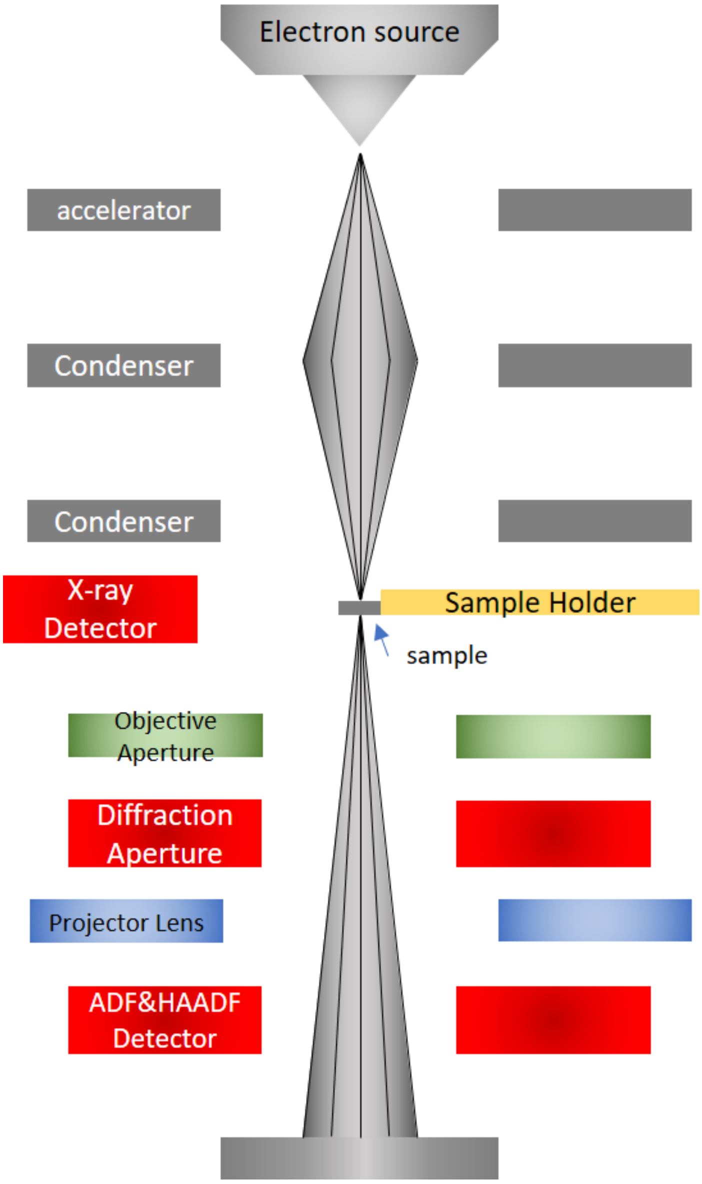

Figure 2.5 - Schematic of Transmission Electron Microscope (TEM)

2.7.3 Focus ion beam analysis (FIB)

Focus ion beam or FIB is a method that can be used to obtain samples, through the ablation of material, and can be used to produce suitable thickness samples for TEM analysis. The equipment used here was a FEI Nova 600i Nanolab. As shown in Figure 2.6, it contains a high-resolution SEM coupled with a focused beam of gallium. The ion beam allows FIB to sputter and mill material at a specific site.[71] The normal requirement for the TEM sample is thickness less than 100 nm. Using FIB a specific portion of the sample can be precisely lifted out, saving time and sample. However, FIB also comes with other problems, the ion beam source used here was gallium, with the observation that no matter how precise the operation is, there will be some gallium left in sample and of course some induced irradiation damage. Normally this does not affect the result, but for samples that would be post irradiated after FIB lift out, the observations could be impacted.

There are numbers of methods using FIB that can be used to make TEM sample. The method used in this project is modified from the fundamental process. As outlined in Figure 2.7, this method contains four main stages, masking, trenching, lift out and polishing.

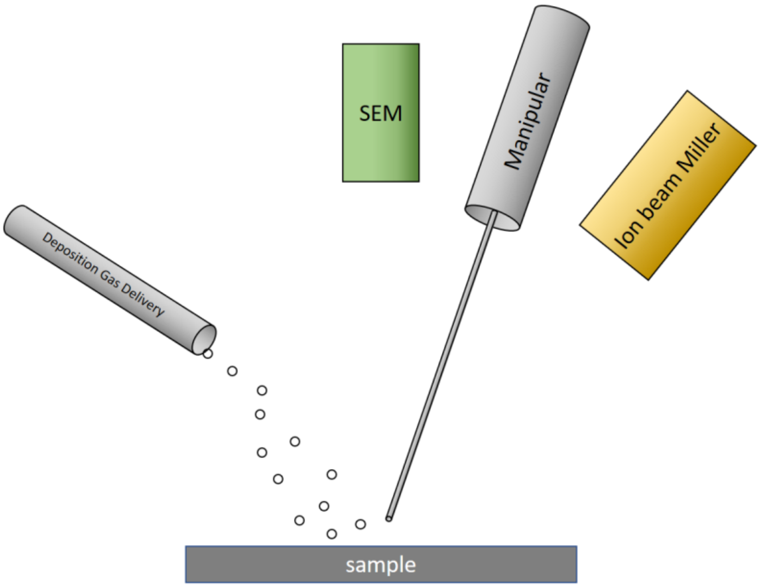

Figure 2.6 - Schematic of operation equipment within FIB workstation

In the masking stage, the target area is masked with carbon and platinum to protect the selected material beneath the surface. The first layer of mask is made by carbon deposition, using an electron beam. The thickness of this layer is designed to be 0.2 µm with an emission energy of 20 KV and current of 21 nA. The second layer is platinum which is made by the ion beam with emission energy of 30 KV and 2.1 nA of current. The thickness of this layer is 2.8 µm with a total thickness of 3 µm. The mechanism of element deposition is using the high energy particle to decompose an organometallic-based platinum and carbon material and coating the material. The reason of deposition carbon is to further protect the potential ion beam damage from the direct ion beam platinum deposition. Also, the carbon layer will significantly reduce the platinum dripping down during the polishing stage which is referred to as ‘curtaining’. The platinum layer provides two main purposes. One is to protect the material from gallium irradiation damage during ion milling. The second is to mark the surface line present under TEM inspection. The final masking parameter is 5 µm wide, 30 µm long and 3 µm hight.

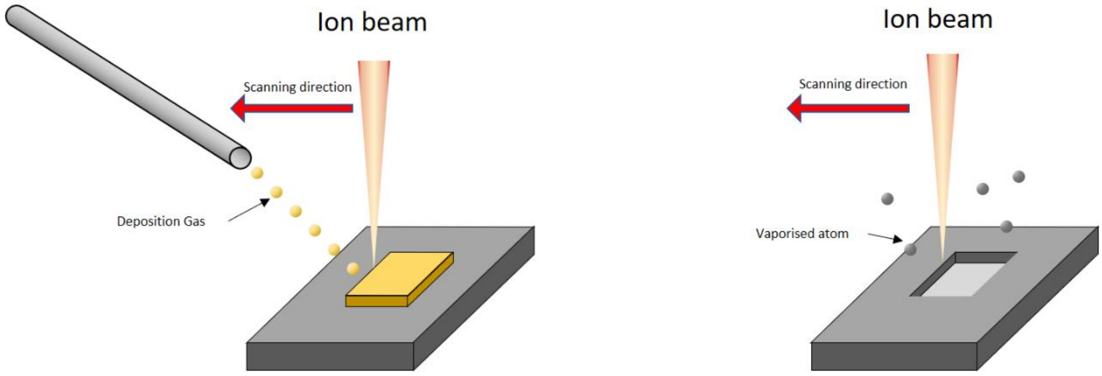

Figure 2.7 - Schematic of two main processes carried out during the TEM sample making left) protection mask deposition, right) the ion milling

The trenching process is used to expose the TEM sample billet from high entropy matrix by ion beam. Two trenches are created on both sides of the sampled area, along the long side of mask. The trench is ~33 µm of length, ~15 µm width with a maximum depth of ~10 µm. The bottom of trench is slopped, the minimum depth is less than 1 µm which is almost flat with actual surface. The slop has the maximum depth close to TEM sample billet site. The cross-section views of this stage result are very close to the shape with ‘W’. After the trench has been dug, the TEM sample billet is thinned down until the thickness approaching around 1 µm. The emission energy and current are alternated in different steps. For the initial trench digging, the emission energy can be set up to 30 KV with a current around 9 nA. Such high energy and current will reduce the focus of the ion beam which means the control of ion beam is reduced and the boundary of milling area is blurrier. Therefore, when the operation approaches the size of the TEM sample billet both the emission energy and current are reduced to enhance the manipulation of ion beam. During the cleaning and thinning process, the emission energy and current are set to 20-30 kV and 0.23-2.1 nA depending on the speed and the controllability required in each milling sequence.

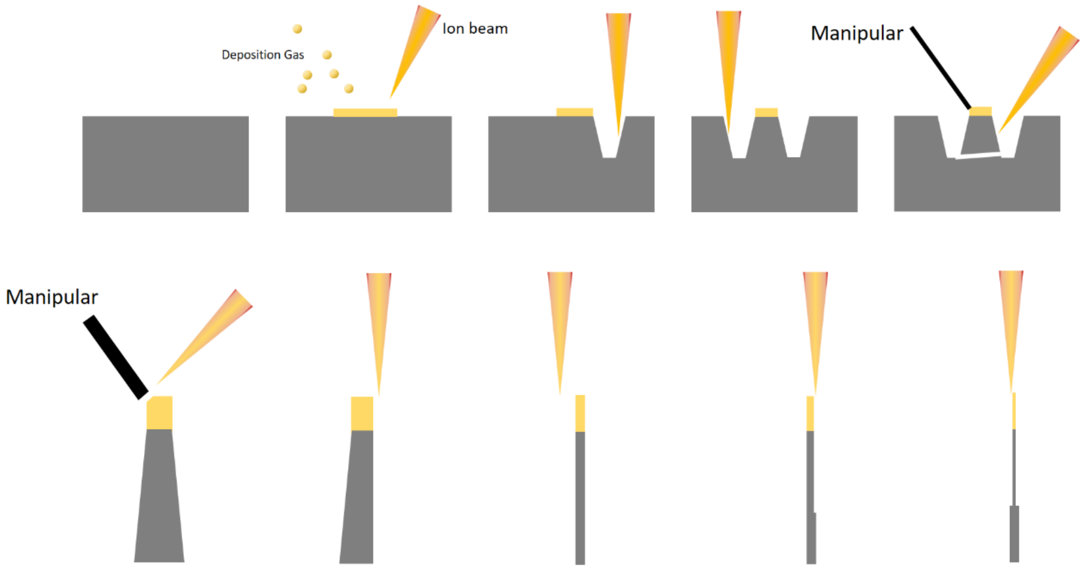

Figure 2.8 - Schematic of TEM sample making process, the main concept is about dig out a section of material and mill it down below thickness around 100 nm

As shown in Figure 2.8, the lift out process is the procedure of taking out the TEM sample billet from the high entropy alloy sample matrix. The TEM sample billet from the last stage is in a thickness ~ 1 µm and sat in a hole with two slopping sides. Due to the position set of electron beam gun and ion beam gun, the entire process needs to cooperate with both gun and movement of platform. To lift out the TEM sample billet, the first step is to perform a standard process called "J-cut".

One side and the bottom side of the TEM sample billet is fully cut by milling away small parts of material. The other side has also been cut with small bands but there is still a connection with the TEM sample billet. At this point, the TEM sample billet is barely staying in position. The second step is welding the OmniProbe on the TEM sample billet and removing the last bit of material connected to the matrix. The TEM sample billet is then carefully "lifted out" from the hole which is the two trenches combined. The third step is transporting to the TEM sample holder, which in this project is a copper C shape TEM sample holder. When the TEM sample billet is in touch with the TEM sample holder, it then welds onto the holder and the part connected to OmniProbe is cut. The TEM sample billet will then stay on the TEM sample holder and transfer to the next stage.

The final stage is the polishing stage. The target thickness for the final TEM sample is around 100 nm or even thinner. The TEM sample billet is tilted parallel to the ion emission direction. Through modification of the angle formed between the TEM sample and the ion beam, it can achieve a very precise control of milling process. The milling process carefully progressed on both sides of the TEM sample billet to reduce the thickness. With decreasing thickness, the requirement of ion beam focus is increased which means the emission energy and current need to be adjusted lower. When the thickness approaches 100 nm, the polishing process is switched to the finishing process. With very low emission energy and current, two sides of TEM sample are further milled down with extremely small amounts of material removed. It is to finalize the surface of TEM sample and remove the potential irradiation damaged zone by ion beam. The finished TEM sample will allow electron pass through and form images in TEM analysis.

2.7.4 Nano-indentation Analysis

The nano-intender is a common hardness test across a very small length scale. There is often no significant difference between a conventional hardness test and a nano-intender test, which inserts a tiny object onto sample surface and applies a uniform load. It then determines the size of indentation by an in-built atomic force microscope. Through measuring the size and combining with loading data it can determine the hardness of a sample surface. The difference in a nano-intender is that insertion distance and load are precisely controlled, but more importantly are small. For example, in a normal nano-intender test the insertion depth is ~ 100nm and the load is of the order of μN. Therefore, in many specialist research areas, such as coatings and films, these properties across a small depth range can be examined more clearly. The nano-intender can be further combined with Dynamic Mechanical Analysis (DMA), a technology able to record the stress and strain as temperature varies during a test to calculate multiple mechanical properties, for example, the complex modulus. Through these combinations, properties which routinely need large scale testing can be performed on small samples, saving both time and sample. However, focusing on a small depth can limit the effectiveness of result for further inside sample. [72]

In this project, the nano indentation replaces the regular physical property tests. Also, the property tested focuses on hardness rather than more a comprehensive experiment. The reason behind this design is this. Firstly, there is only a limited amount of sample synthesised in this project, with each sample ingot weighing around 30-50g. There is simply not enough material to preform full scale mechanical test. Secondly, the synthesis process does not involve any wildly recognised standard to unify the thermal process and reforming process to regulate the sample product. Therefore, in order to understand the original properties within the high entropy alloy, the as casted ingot is normally formed without applying any further mechanical process to avoid potential effects on the test result. The third reason is that the irradiation affected zone is limited on very shallow area in the sample surface, which is problem for post irradiation properties test. From the macro view, the irradiated material formed a thin film with a thickness ~ 1 - 5μm on the surface of the original sample matrix. Such thin film is not able to perform common mechanical testing. Therefore, a thin film mechanical test is employed as the main test method, with the nano intender used as the main test. The nano intender is designed to test the mechanical properties of the coating layer on the sample. It is able to collect the various data to review the various properties. However, the main assessed properties are micro hardness of the top layer material. This test is performed on both pre and post irradiated sample to ensure the consistency of test result for comparation. The reason for this hardness test is that the nano intender analyses the sample surface by micro probe, which is fundamentally similar to the majority of hardness test, so using hardness data will provide maximum credibility to future analysis process. The particular module used in this project is able to provide the consistent date of hardness with the depth increase. It gives a range of data across the potential irradiated zone which allows the continues observation of hardness changing. In this analysis, under the situation that most of bulk mechanical test is unable to be performed, the selection of the test property should represent the key mechanical property to the maximum extent possible. For the nuclear industry, strength is one of very important design specification for the materials. it affects multiple qualities like working load, flexibility and etc. The strength within one material is ultimately reflect the resistance of fail under the outer system load. In all the data that nano intender collects, the hardness is one property that most relates to such a property. Although hardness cannot present strength for a material in any meaning, the changing trend of hardness is able to indicate the trend of strength shifting. Through analysing the hardness shift, it is able to assess the overall strength shift within the material. However, as a compromised test method, micro hardness testing allows the smaller scale of observation and ensure the project can be proceed, but it also brings numbers of challenge to it. The most important problem is that the nano intender equipment has its trust data range of depth between 30-150nm which is far smaller than the estimated irradiation affected zone even for the gold ion. It means that only part of the irradiation affect zone will be examined during the test. From the simulated results, the investigated will be located at the increasing stage on the range of irradiation damage accumulation. Also in such range, the data collection does not cover the maximum damage area. Therefore, the peak value of actual hardness and simulated damage cannot be analysed together to exam the consistency of theoretical simulation. A second problem is that the method is largely reliant upon the reading of the micro probe, which is the connection between the sample and the sample holder. The binding between the sample and holder needs to be strong enough to prevent sample slip away from the sample holder when the test probe indents the sample surface and the force applied on sample is off centre. However, the binding material should not be swell or change its volume during the "hardening" process, as changing in binding material volume can break the alignment of sample surface to the test platform. Also, sponge tape cannot be the adhesive, as during test the compressing of tape might snap the tip of micro probe. In this particular case, "Correction fluid" is used as adhesive to place the sample to the platform. It is basically a mixture of titanium dioxide and thinner agent which is not an ideal adhesive in any aspect, but it is easily obtained and meets most of the requirement in the application

2.7.5 Magnetic Hysteresis Analysis

The high entropy alloy samples selected in this project contain iron, cobalt, and nickel all of which are magnetic, with the magnetic properties of the bulk material largely dependent on the arrangement of magnetic moments, which in turn is defined by both the electron configuration and equilibrium state. Therefore, it is necessary to understand the magnetic behaviour of such samples before applying electron microscopy-based analysis, as they involved charge particles which will be affected by the magnetic field. The equipment for this analysis applies a strong magnetic field to the target sample, to determine the magnetic properties, such as coercivity and magnetic remanence. The collect data is then plotted as a function of magnetic moment against induced magnetic field, as shown in Figure 2.9, forming a hysteresis loop. In this work it was used to determine if the samples were magnetic before analysis.

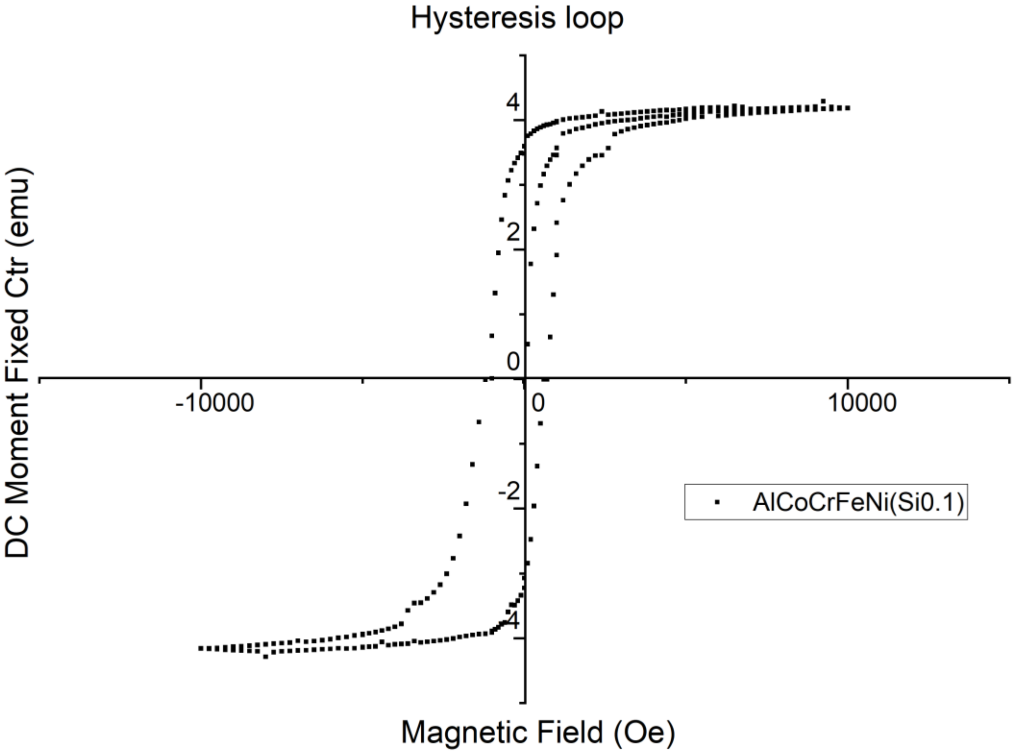

Figure 2.9 - An example of hysteresis loop test result, it shows significant magnetic saturation and small magnetic residue

Chapter 3 - Fabrication and Bulk Analysis

3.1 Sample synthesis

For each sample, the optimum volume fabricated was ~10 × 10 × 2 mm, providing sufficient material for experimental work, and analysis. To minimise waste each sample was cut after irradiation, with pieces used for analysis. The detailed calculation for masses is listed in Table 3.1.

Table 3.1 - Masses used in the synthesis of samples for analysis

$Co_{1.5}CrFeNi_{1.5}Ti_{0.5}Mo_{0.1}$						
element	Co	Cr	Fe	Ni	Ti	Mo
Batch mass(g)	8.8436	5.2017	5.5868	8.8076	2.3943	0.960
moles	0.150	0.100	0.100	0.150	0.050	0.010
TaNbHfZrTi						
element	Ta	Nb	Hf	Zr	Ti	
Batch mass(g)	17.991	9.2372	17.746	9.07	4.7592	
exist mol	0.0994	0.0994	0.0994	0.0994	0.0994	
$AlCoCrFeNiSi_{0.1}$						
element	Al	Co	Cr	Fe	Ni	Si
Batch mass(g)	3.193	7.050	6.220	6.680	7.021	0.336
exist mol	0.1196	0.1196	0.1196	0.1196	0.1196	0.011
CoCrCuFeNi						
element	Co	Cr	Cu	Fe	Ni	
Batch mass(g)	7.420	6.546	8.001	7.031	7.389	
exist mol	0.125	0.125	0.125	0.125	0.125	

The element material applied as ingredient is selected with pure element material with an average purity of 99.99%-99.9999%. The materials were purchased from Advent, Alfa-Aesar and GoodFellow (detailed purchase list in appendix.). High purities were chosen to reduce impurity effects in the final product, as the composition distribution of element is associated to the degree of the high entropy state within high entropy alloy. The synthesis process of high entropy alloy was the same in all the samples used in this project. The manufacturing of high entropy alloy need several conditions to ensure the quality of the sample and the safety of the action. The first was that using high purity elements were used as high purity element control the composition of element in the final alloy, helping to ensure the formation of alloy in the first place. However, using pure elements can be dangerous due to most of transition material is very reactive in their pure form as powders. Also, the smelting process is involving very high temperature which could lead the ignition of material or even explosion. Therefore, majority of the high entropy alloy synthesis process take place under vacuum or a low pressure of protection gas, such as Ar. The second issue is the melting temperature can be very high, not only because some of material element have high meting points, but also to compensate the heat lose through the crucible wall and ensure all the material is in the liquid form to guarantee complete mix. In this project a vacuum arc-furnace was used to synthesis all the samples. The reason for this method is that it has suitable capacity of making sufficient amount of samples required. The indirect contact electrode produces a high voltage electron arc capable of generating sufficient heat to melt all the components and avoid contamination at the same time. All material is loaded in the water cooled crucible, after they been weighted and sectioned into suitable batch. The operation chamber is vacuumed and slowly pumped with protection argon gas. The high voltage arc introduces heat into material and melts all the material, with magnetic stirring mixing the pool of melting metal. The melting time is limited to prevent evaporation of metal under low pressure. When mixing is finished, the high voltage arc is stopped, and the alloy allowed to solidify quickly into an ingot. The formed ingot will then be turned over and a second melt performed. The second melt is minimised un-melted material. The solidified alloy ingot is removed from the crucible and quenched in air. All sample fabrications were preformed using the same synthesis route. As shown in Figure 3.1, all the ingots formed as button-like shapes with diameter around 30 mm. Due to the restriction of vacuum arc-furnace, the powdered form of silicon was discarded from the planed synthesis of $AlCoCrFeNiSi_{0.1}$, which while having an impact on the performance of the final product, it would not affect the high entropy formation.

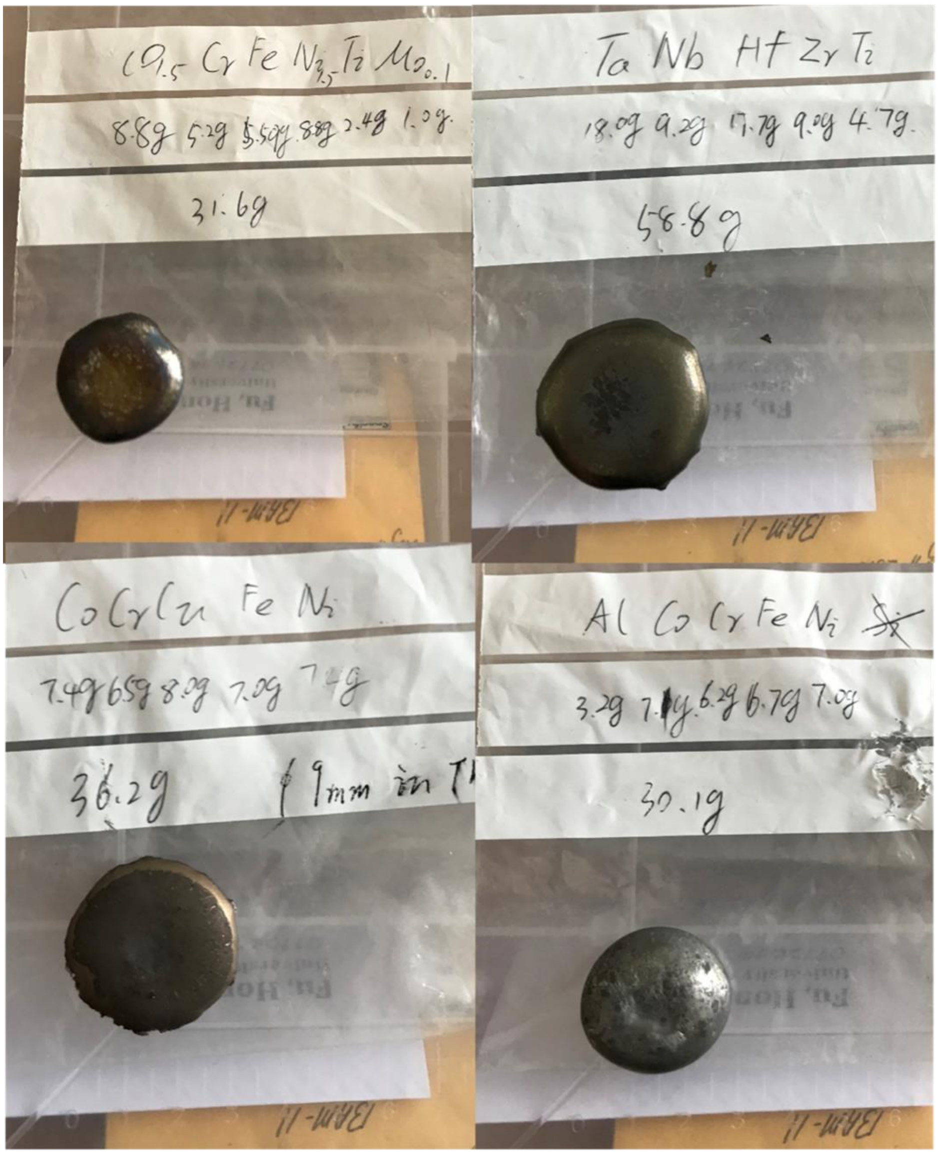

Figure 3.1 – Images of as formed ingots of HEA after melting in the arc melter.

All the button ingots have a similar surface geometry, with a small dent in the centre of each ingot, likely due to the fast cooling causing uneven shrinkage across the sample, arising from the outer ring of the ingot solidifying faster than the centre part. All samples had a level of oxidation on the surface. From observation, this oxidation phenomenon seemed to not happen after the sample came in contact with air, but before the melting chamber breached vacuum. This oxidation could have arisen from existing oxidation layers in the source material. Once melted, this oxidation layer would float to the surface, similar to that found in steel making. The resultant mass of each element was close to the estimated mass of the product, indicative of the high yield from the arc furnace.

Once the ingots had cooled, they were sectioned with the pattern shown in Figure 3.2, with the initial half cut being made by gravity saw, with the other sections by wire spark erosion. Due to the size and cutting technology, each sample produced more than 10 testable samples. Each sample was then ground and polished down to a 1 µm finish. The cut surface showed metallic sliver colour indicating the alloys did not significantly react with air.

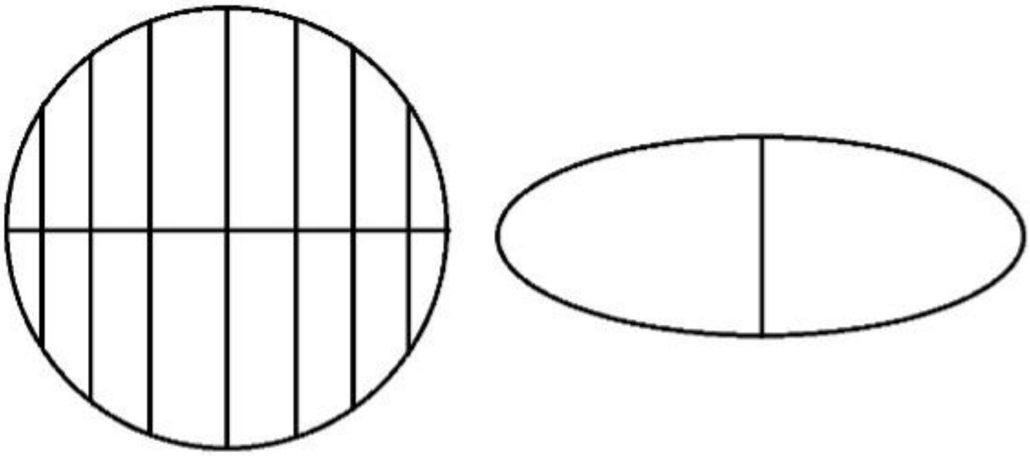

Figure 3.2 - Schematic sectioning pattern of HEA ingots

3.2 SRIM Predictions of Damage and the ion impanation set up

Simulations were performed to estimate both the ion deposition range, and the irradiation effected zone for each sample under various ion source radiation. The Stopping and Range of Ions in Matter (SRIM) simulates the damage and range of ions into matter. [24]

The ions selected for the simulations were gold, helium, hydrogen and nickel, which were chosen as they simulate damage within a reactor core. The simulations predict a range of paths for each ion within the target material, based on interactions within the target, which are then recorded and analysed. Through analysis of the data, an estimation of the damage range and magnitude can be made. The numerical results are shown in Table 3.2, which shows the peak damage depths for each of the simulations. and graphically in Figure 3.3.

The displacement energies for each of the metallic species were 25eV, with each simulation running for 3000 ions. The density for each sample was taken as that being estimated by SRIM, which is based on the relative atomic masses in a unit volume.

System	4.5 MeV Au	3 MeV Ni	4 MeV He	6 MeV H
$Co_{1.5}CrFeNi_{1.5}Ti_{0.5}Mo_{0.1}$	15.6	2.5	0.024	0.007
TaNbHfZrTi	13.4	2.4	0.012	0.003
CoCrCuFeNi	16.9	3.8	0.023	0.005
$AlCoCrFeNiSi_{0.1}$	10	2.4	0.018	0.005

Table 3.2 - Calculation of the estimated peak damage of each ion implantation as vacancies per Angstrom per ion

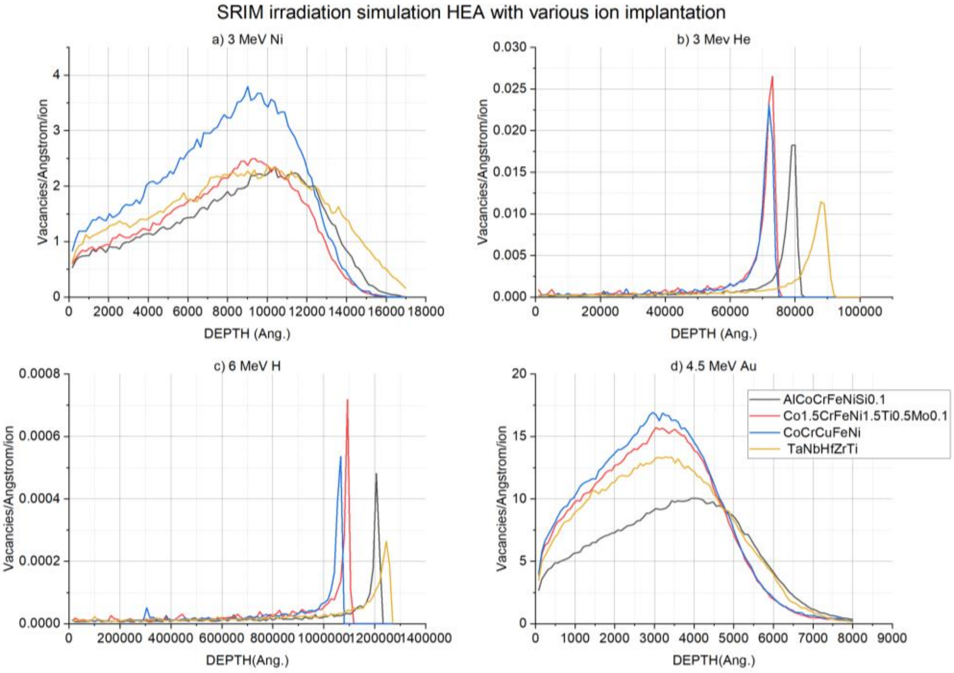

Figure 3.3 - The SRIM simulated damage profile of four different elements on each high entropy alloy sample, a) 3MeV Ni, b) 3MeV He, c) 6MeV H, d) 4.5 MeV Au

The energy for nickel irradiation was chosen to be 3 MeV, shown in Figure 33(a). From the simulations CoCrCuFeNi would be expected to show the most damage, whereas $AlCoCrFeNiSi_{0.1}$ would be expected to show lower levels of damage. The energy for gold irradiation was chosen to be 4.5 MeV, with the simulation showing the peak in interaction/damage occurring at a depth of ~200-400 nm, below which the level begins to drop, until the end of simulation at 800 nm. The simulations indicate that $AlCoCrFeNiSi_{0.1}$ was predicted to show the lowest level of damage, shown in Figure 33(d), when irradiated by gold at 4.5 MeV. By comparison with nickel irradiation the damage range from 3 MeV Ni is deeper than would be expected from 4.5 MeV Au.

The energy chosen for helium and hydrogen irradiations were chosen to be 4 MeV and 6 MeV respectively, shown in Figure 33 (b) and (c). Due to the nature of the He and H ions and the energies chosen, the expected interaction within the solid was much less than for Ni and Au, but over a much longer range. As expected, the predicted damage is much lower, but also goes much deeper. In this case the peak damage is expected to be ~ 0.03 for $Ca_{1.5}CrFeNi_{1.5}Ti_{0.5}Mo_{0.1}$ with 4 MeV He whereas for 3.5 MeV Au, the peak damage was 15 vacancies per Angstrom per ion. The nature of the damage profile was also changed. In the He/H cases the peak damage is expected to be localised in a narrow window, whereas in the Ni/Au cases the damage was over a much longer depth range. This is typical of the nature of the irradiations and agrees with both other simulations and experimental work. One of the mechanisms behind this set up is that for the nature of the high energy ions impacting the target material, the ions have two characteristic interactions electronic and nuclear.[73] In the initial stage of impacts, the stopping process of an ion is dominated by electronic interactions due to the high speed of the ion and the charge it carries. As the ion continues and transfers energy, the interactions change to become more nuclear in nature. Due to the large difference, in mass/energy between each implanted species, these two mechanisms occupy different ranges in the overall stopping process.

To increase the volume of damage when irradiating with He ions and make it closer to the surface for aiding analysis, simulations were run where the energy for the incident ion was changed, rising from 60 keV to 140 keV, using SRIM. This was undertaken in preparation for lower energy He irradiations being undertaken, and graphically shown in Figure 3.4.

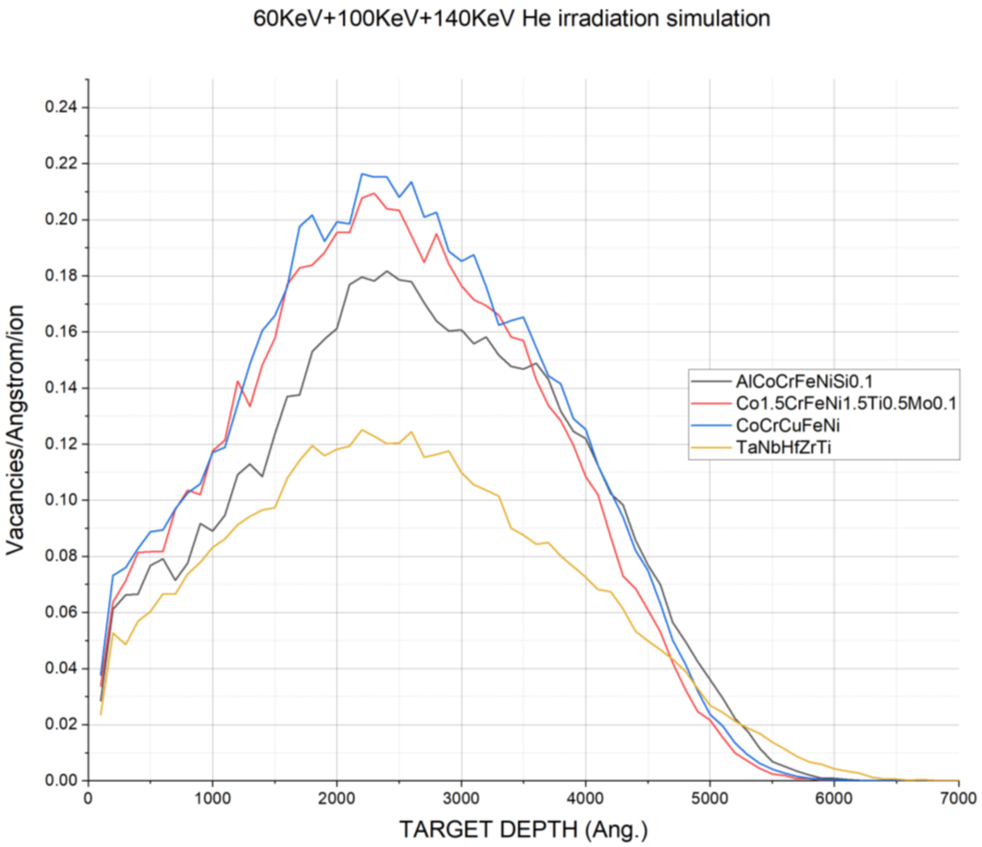

Figure 3.4 - The plot of combined overlap helium irradiations predicted for each sample

Simulation gives an indication of the interaction between the incident ion and atomic structure which directly links with the focus of this project. In order, to investigate any change in microstructure after undergoing ion beam irradiation, the observation site should be chosen carefully. These simulations give an estimated range for where damage/displacement has occurred, leading to a higher possibility of visibility. Due to the limitations of methods such as TEM, reducing the observation window has a huge benefit in increasing the efficiency of analysis.

The vacancy data collected from SRIM, is also used to give an estimated dpa value for the designed ion implantation dose, both overall and within the observation windows.

Irradiation set up	4.5 MeV Au			3 MeV Ni		
Ion dose (x 10^{15} ions cm^{-2})	1	2.5	5	1	2.5	5
$Co_{1.5}CrFeNi_{1.5}Ti_{0.5}Mo_{0.1}$	184	460	920	29	73	146
TaNbHfZrTi	266	665	1329	47	118	236
CoCrCuFeNi	194	486	972	43	109	218
$AlCoCrFeNiSi_{0.1}$	122	306	612	29	72	143

Table 3.3 – Estimated dpa values for the ion fluences for gold and nickel irradiations

What should be noted under these irradiations, is that whilst the total level of damage changes with total fluence, the range of damage is not expected to change significantly as this is related to the change in energy. This can be seen in Table 3.4 where the He ion energy is changed.

Irradiation set up	60 keV	100 keV	140 keV	Total Damage(dpa) at peak
$Co_{1.5}CrFeNi_{1.5}Ti_{0.5}Mo_{0.1}$	10.83	9.73	9.60	30.17
TaNbHfZrTi	11.99	10.52	9.28	31.79
CoCrCuFeNi	12.29	11.59	10.41	34.29
$AlCoCrFeNiSi_{0.1}$	11.28	10.13	10.00	31.41

Table 3.4 - Estimated dpa values for the He irradiations, at each energy and as a total

Ion implantations were planned for Au and Ni irradiations at room temperature to three fluences, 1 × 10^{15}, 2.5 × 10^{15} and 5 × 10^{15} ions cm^{-2}., at the Dalton Cumbrian Facility without temperature control. However, due to issues arising from the Covid lockdown it was not possible to complete the Au irradiations, with only the Ni irradiations being completed. For He irradiation, the sample was step wise irradiated to 1 × 10^{16} ions cm^{-2} at the three energies previously outlined, i.e., 60, 100 and 140 keV. This irradiation was undertaken at the Leonard Kroko Inc again without temperature control. During the ion implantation process, all four entropy alloy samples are aligned to perform the same ion implantation on one stage, shown in Figure 3.5

The choice of nickel and gold ion was to create suitable damage within each set of experiment. Combined with 3 difference fluences of ion implanted, it can provide damage from ~30 dpa to ~1000 dpa. It covers a large range of damage allowing for a comprehensive investigation on the relationship between irradiation damage accumulation and property change. Helium ions can cause damage in metals, along with He gas bubble formation. The set of overlaid ion implantation with relative low emission energy increases the observation window, reducing the observation that helium ions tend to leave a very narrow observation window.

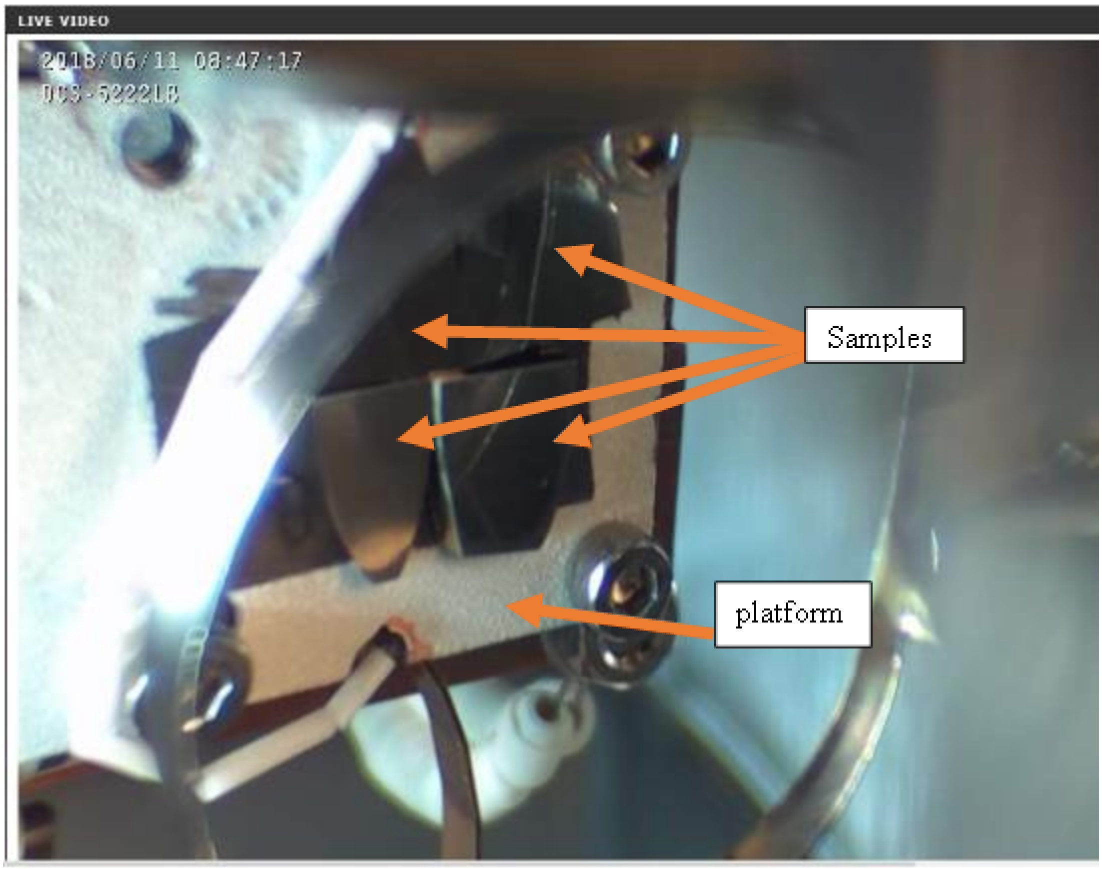

Figure 3.5 – Photograph of the layout for each set of ion implantations.

3.3 Post Irradiation Examination

After implantation the HEA samples all showed a slight colour shift within the irradiation affected zone. For example, under heavy ion, the irradiation affected zone turned darker. This colour shift was proportional to the fluence, as with increasing fluence the colour became darker. For the helium ion implantation, the irradiation affected zone turned a yellow-brown colour. As shown in Figure 3.6, there were clear marks for the irradiation zone at a fluence of 5×10^{15} ions cm^{-2}. However, this mark was less visible in the 1×10^{15} ions cm^{-2} samples.

This change in colouration could come from multiple sources. It could for example arise from impurities within the sample migrating to the surface as part of the irradiation, or the colour change could come from contamination within the sample environment. In either case, the surface coating was not strongly bound, and could be wiped clean easily.

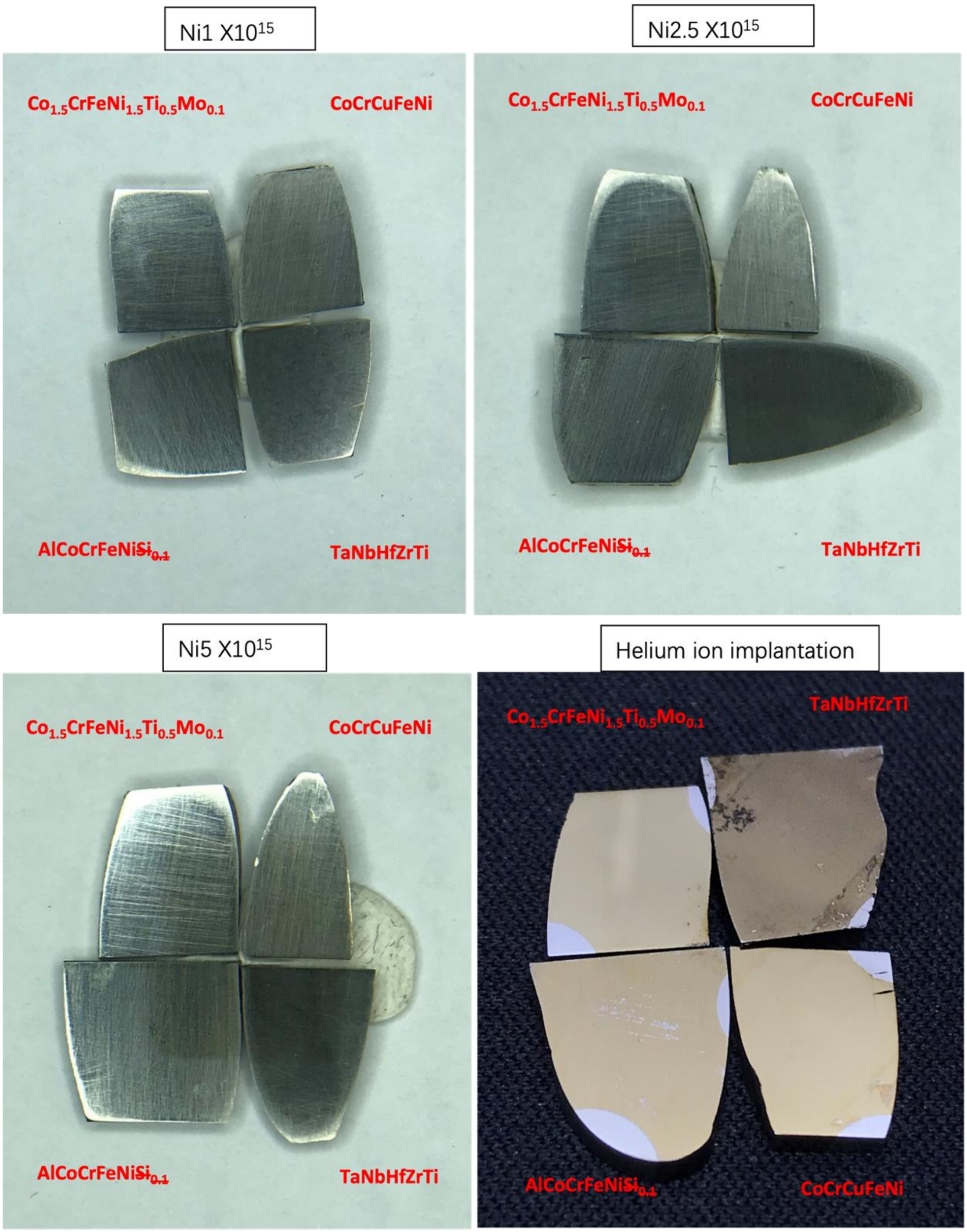

Figure 3.6 - The close sample image of each batch sample irradiated

3.3.1 Nano-Indentation Tests

Nano-indentation tests were performed on each sample, both pre- and post-ion implantation, to determine the relative change in hardness for each HEA being studied. During the testing, the sample was fixed on the test platform with very weak adhesive which in this project is a white paint. It can provide sufficient bonding without applying extra mechanical force on the surface which can cause physical damage. Alternately, as the nano-intender is an extremely sensitive test, the sample and platform should be hard connected, as any contraction or deformable adhesive material will affect the data collected from nano-intender. Therefore, considering the efficiency in use of experimental time, the white paint was used as the adhesive to fix the sample to the stage.

For nano-indentation collection a Bruker Hysitron TL 980 Triboindenter was used with a triangular tip, with in-situ scanning probe microscopy, allowing for a range of surface features to be observed. In this analysis the data has a trustable range of between 20 and 150 nm in depth.

3.3.1.1. $Co_{1.5}CrFeNi_{1.5}Ti_{0.5}Mo_{0.1}$

For the $Co_{1.5}CrFeNi_{1.5}Ti_{0.5}Mo_{0.1}$, shown in Figure 3.7, it can generally be seen that with increasing radiation damage, hardness decreases. The non-irradiated sample has the highest hardness compared to other irradiated samples. The helium ion irradiated sample presents a huge drop in the hardness with the depth raised. Two of the nickel ion irradiated samples shows similar trend of hardness shift, and 2.5×10^{15} ions cm^{-2} of nickel ion inset which has higher irradiation damage has generally lower hardness. Although there is a shift in the relative hardness of ~ 0.5 GPa, the hardness as a function of depth is similar for each. As the only difference between the two irradiations is the level of damage, this may indicate that the ion irradiation has an impact at these depths, with the magnitude of damage being different.

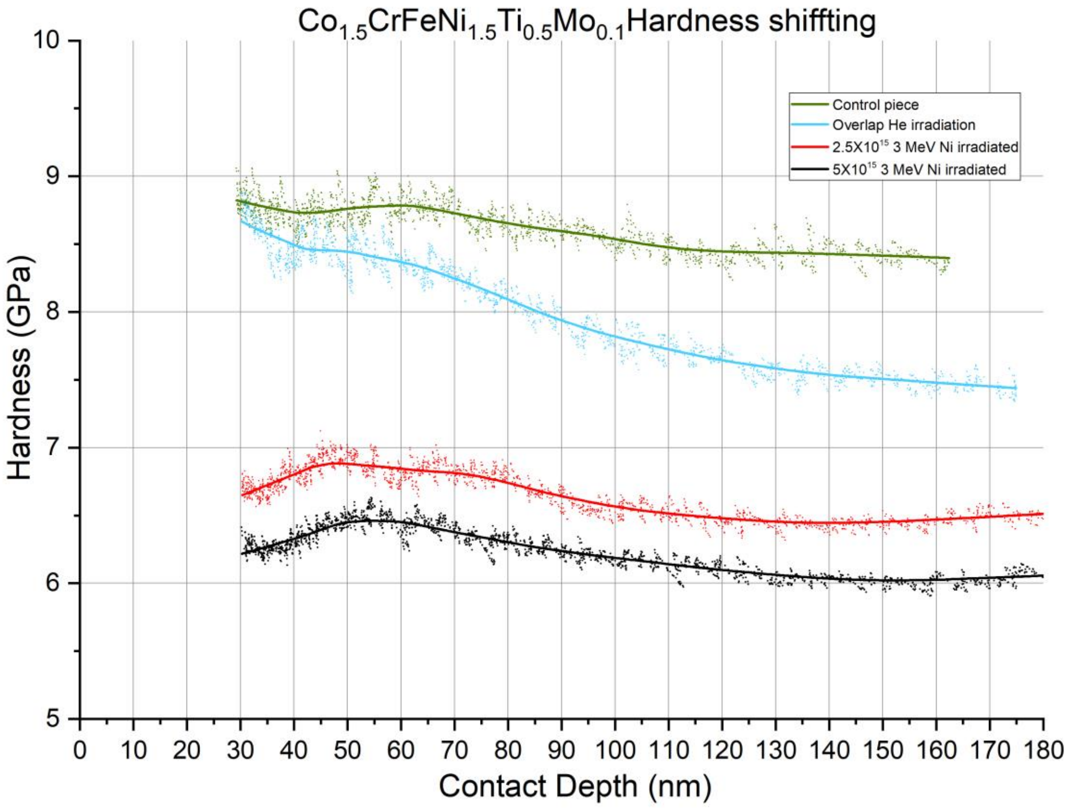

Figure 3.7 - Plot of hardness profile as a function of depth for each irradiation of $Co_{1.5}CrFeNi_{1.5}Ti_{0.5}Mo_{0.1}$

For the helium irradiation, the hardness shift of the irradiated sample followed a descending pattern with increasing depth. This agrees with the expected damage range of the helium being deeper but at a much lower level of damage. In this case the helium irradiation, given the nature of the interaction, i.e., mainly electronic in nature, has possibly annealed any pre-existing stress/strain from the formation of the sample.

3.3.1.2. CoCrCuFeNi

CoCrCuFeNi responded similarly to $Co_{1.5}CrFeNi_{1.5}Ti_{0.5}Mo_{0.1}$, shown in Figure 3.8, as under irradiation the hardness reduces as the damage builds up. The un-irradiated sample shows a significant drop in hardness from the surface with increasing depth, with the drop being sharper than for other samples. The sample irradiated with 5×10^{15} ions cm^{-2} while showing the lowest recorded hardness increases as a function of depth. The hardness reduction is related to the damage level. At this depth, the irradiation damage is increasing with depth and increasing with the ion implanted dose.

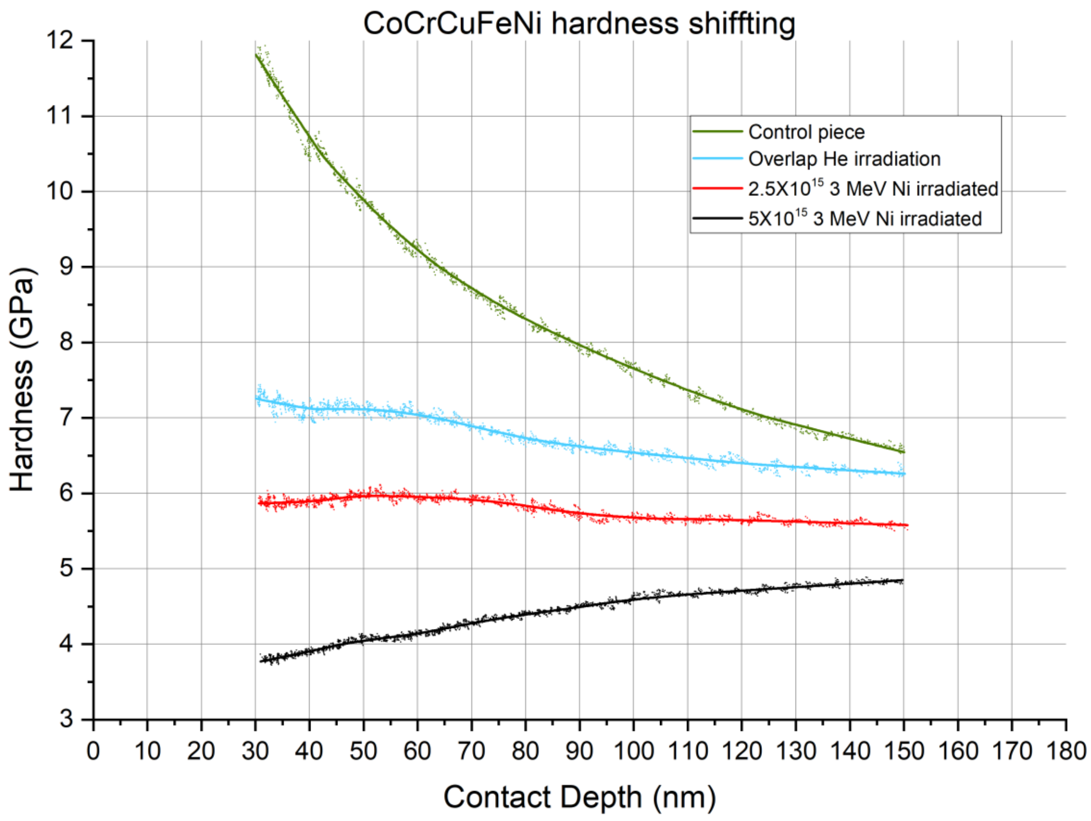

Figure 3.8 - plot of hardness profile as a function of depth for each irradiation of CoCrCuFeNi

The helium ion irradiated sample does not show a large reduction in hardness, when compared with the heavy ion irradiated samples. It appears similar to the 2.5 × 10^{15} ions cm^{-2} Ni irradiated sample which show little variation in hardness with depth, with the overall change within 0.5 GPa.

3.3.1.3. TaNbHfZrTi

As shown in Figure 3.9, for TaNbHfZrTi the non-irradiated sample showed a decrease in hardness with increasing depth, whereas the 2.5 × 10^{15} ions cm^{-2} sample showed an initial increase in hardness between 30 - 60 nm, which continued to be harder than the unirradiated material at the depths being analysed. However, as with CoCrCuFeNi, when irradiated to 5 × 10^{15} ions cm^{-2}, the hardness again decreased, but still followed a similar trend. Different from Ni irradiation, the He irradiated sample shows an initial decrease in hardness, but with the hardness increasing with increase depth, till at ~110 nm it is harder than the initial sample.

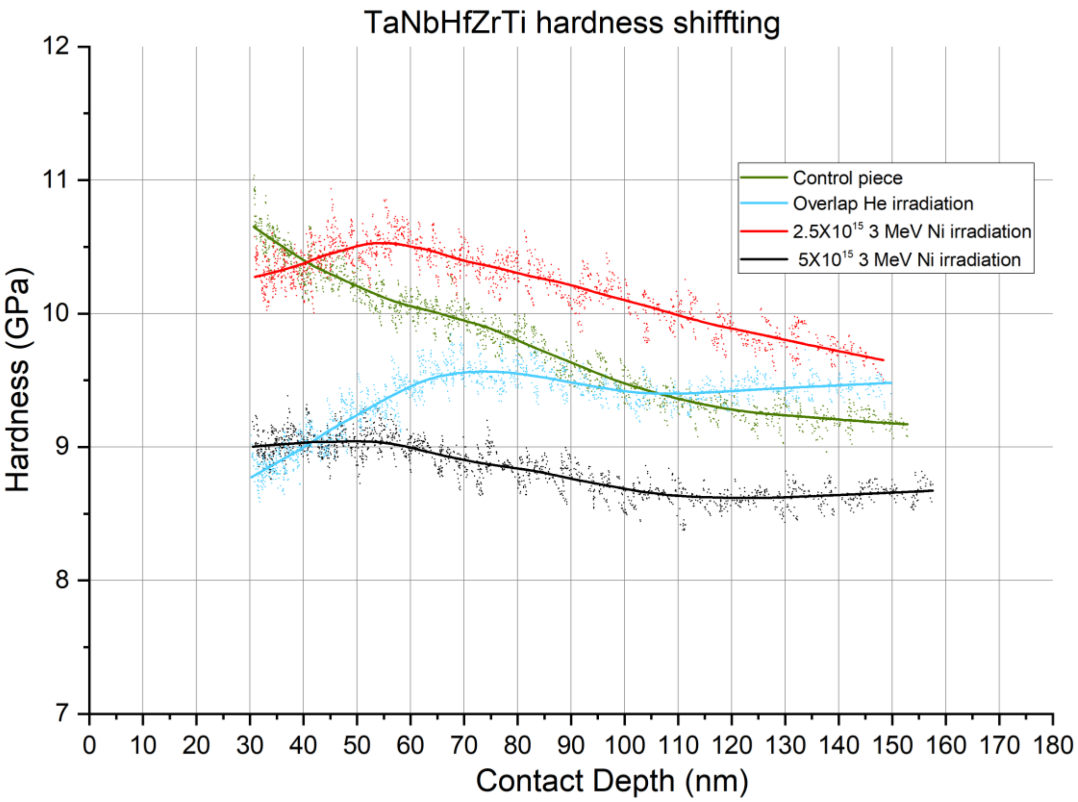

Figure 3.9 – Plot of hardness profile as a function of depth for each irradiation of TaNbHfZrTi

3.3.1.4. AlCoCrFeNi

AlCoCrFeNi shows a similar tendency to that seen in TaNbHfZrTi under Ni irradiation, shown in Figure 3.10, with irradiation by 2.5 × 10^{15} ions cm^{-2} giving rise to a sample which shows increased hardness. As with TaNbHfZrTi and for that matter $Co_{1.5}CrFeNi_{1.5}Ti_{0.5}Mo_{0.1}$ and AlCoCrFeNi at 5 × 10^{15} ions cm^{-2} show a substantial decrease in hardness, in this case moving to be softer than the unirradiated material.

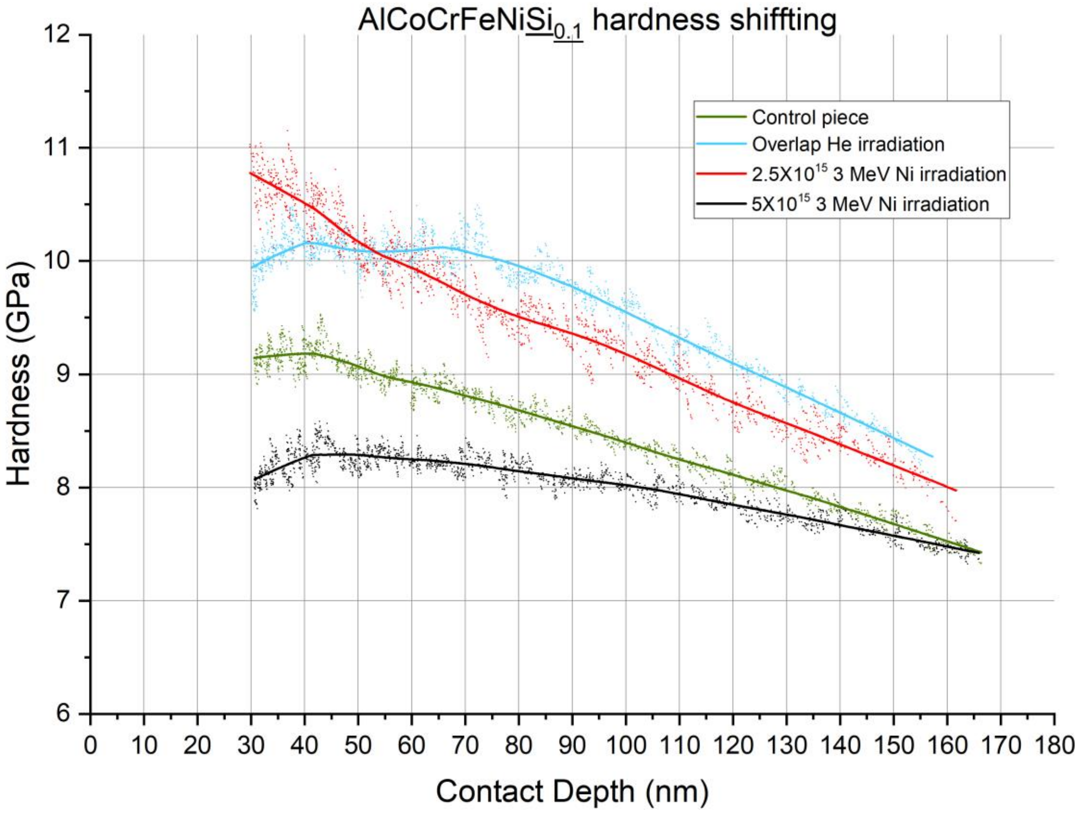

Figure 3.10 – Plot of hardness profile as a function of depth for each irradiation of AlCoCrFeNi

After He irradiation the sample showed an increase overall hardness, but as with the other measurements became softer with increasing depth.

3.3.2 Magnetic Hysteresis Analysis

Magnetic hysteresis loop tests were performed on each sample to determine their magnetic properties. Small amounts of sample were placed in the test equipment, and a strong magnetic field applied, the response to this magnetic field was then determined and plotted.

As shown in the Figure 3.11, these three samples have low magnetic coercivities and low magnetic remanence. CoCrCuFeNi has small response to the applied magnetic field, but quickly saturated with increasing magnetic field, and has zero magnetic residue, i.e., it is 'soft' nature. The other two systems, $Co_{1.5}CrFeNi_{1.5}Ti_{0.5}Mo_{0.1}$ and TaNbHfZrTi, show extremely low response to the applied magnetic field, with $Co_{1.5}CrFeNi_{1.5}Ti_{0.5}Mo_{0.1}$ effectively have a zero response.

As shown in Figure 3.12, by comparison, the AlCoCrFeNi sample has a much higher magnetic saturation and coercivity. Although the magnetic field remanence was still not large. This material could be magnetised, with saturation of ~ 4 emu, and will stay magnetised without an applied magnetic field, ie., implying a ‘hard’ magnetic material. [74]

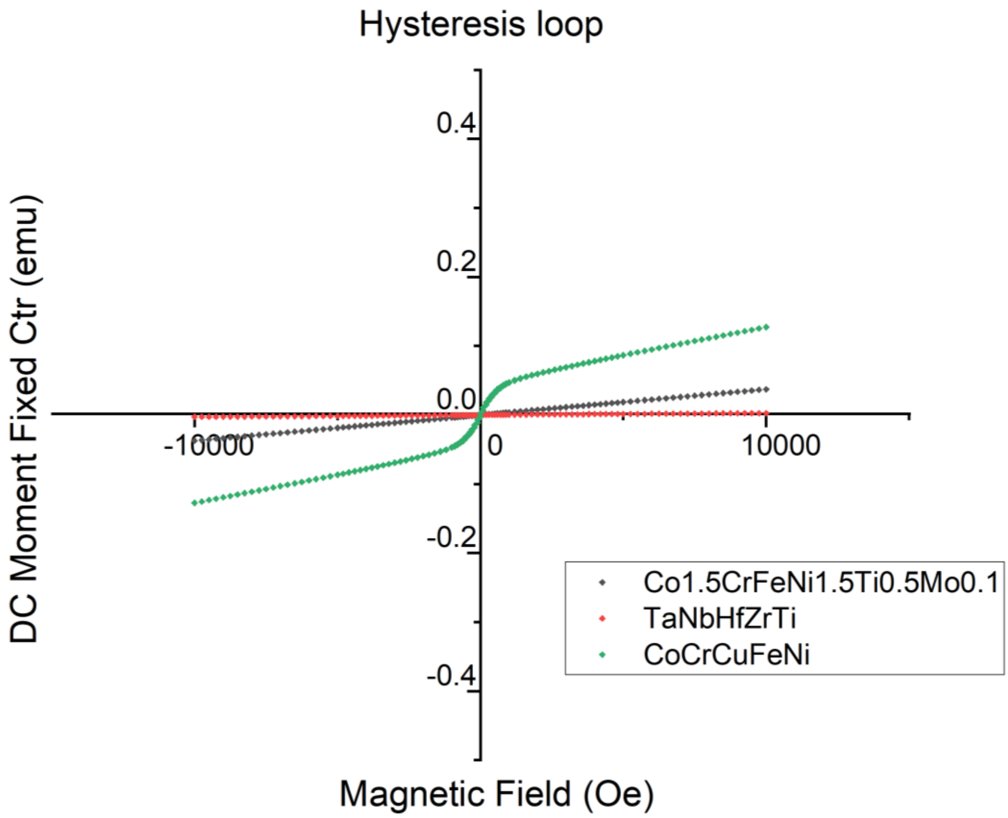

Figure 3.11 - Hysteresis loop test results for $Co_{1.5}CrFeNi_{1.5}Ti_{0.5}Mo_{0.1}$, TaNbHfZrTi and CoCrCuFeNi

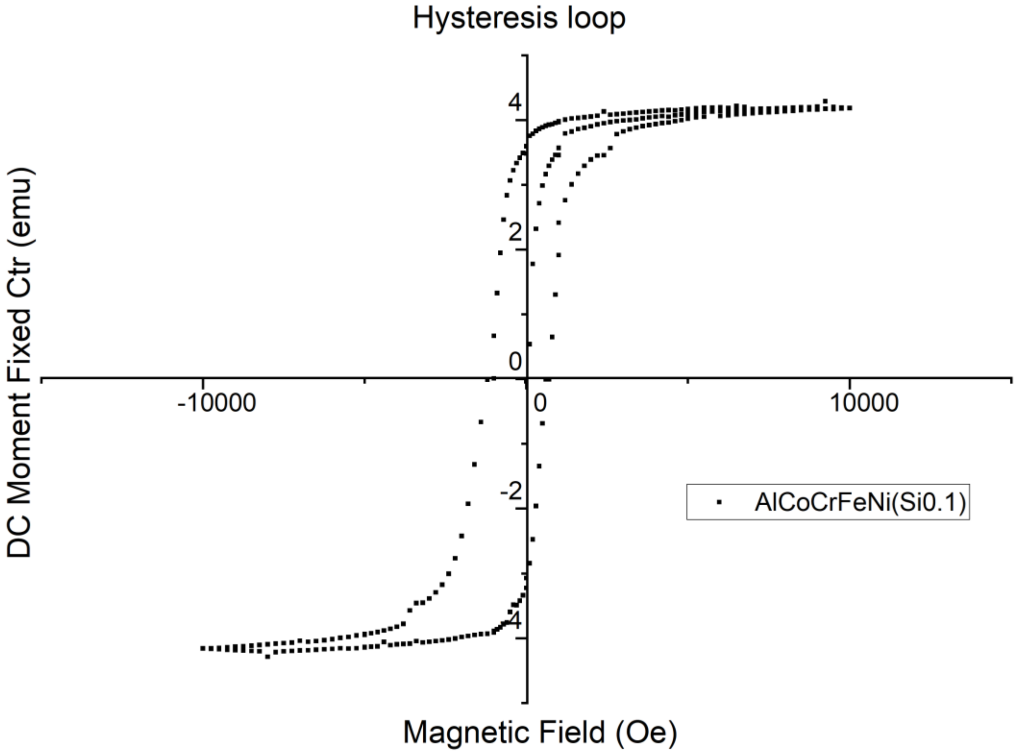

Figure 3.12 - Hysteresis loop test result for AlCoCrFeNi

Chapter 4 - Transmission Electron Microscopy (TEM), and Energy Dispersive X-ray (EDX) Analysis

TEM is an ideal for observing the microstructure of a material, with diffraction being used to visualise the crystal structure of selected area. Additional energy dispersive X-ray spectrometers help identify elemental composition, and their distribution in the observed location.

Sample preparation for TEM analysis was undertaken using FIB lift out of samples from areas of interest. The FIB lift out was undertaken using a FEI Helios Nanolab 600i Dualbem FIB/SEM, with a field emission electron accelerating emission voltage of 30 kV. The focused ion beam was gallium with an energy range of 0.5-30 kV, dependent on how the Ga was being used. Using the FIB/SEM allowed for control and manipulation of the sample being prepared for TEM analysis.

The TEM analysis was performed using a Jeol 2100+ TEM with a LaB6 electron source working at 200 kV accelerating voltage, with image/diffraction collection using a Gatan RIO camera with a resolution of 2k x 2k. EDX analysis used an Oxford X-MAX 65T SDD.

4.1 TEM Analysis of $Co_{1.5}CrFeNi_{1.5}Ti_{0.5}Mo_{0.1}$

4.1.1 Pre-Irradiation Analysis

Near the surface, as shown the Figure 4.1, the $Co_{1.5}CrFeNi_{1.5}Ti_{0.5}Mo_{0.1}$ shows layering with depth. At ~100 nm depth from the surface, there are visible a cluster of dark lines aligned in different directions, marked with a green line. There are several grains that can be spotted at this depth. The diffraction pattern shows the material in this area is effectively a single crystal. However, the spots in the diffraction pattern show a diffuse halo, near the central spot. This suggests that in this area, the high entropy alloy has formed a single structural form, but with formation of grains with slightly different crystal orientations.

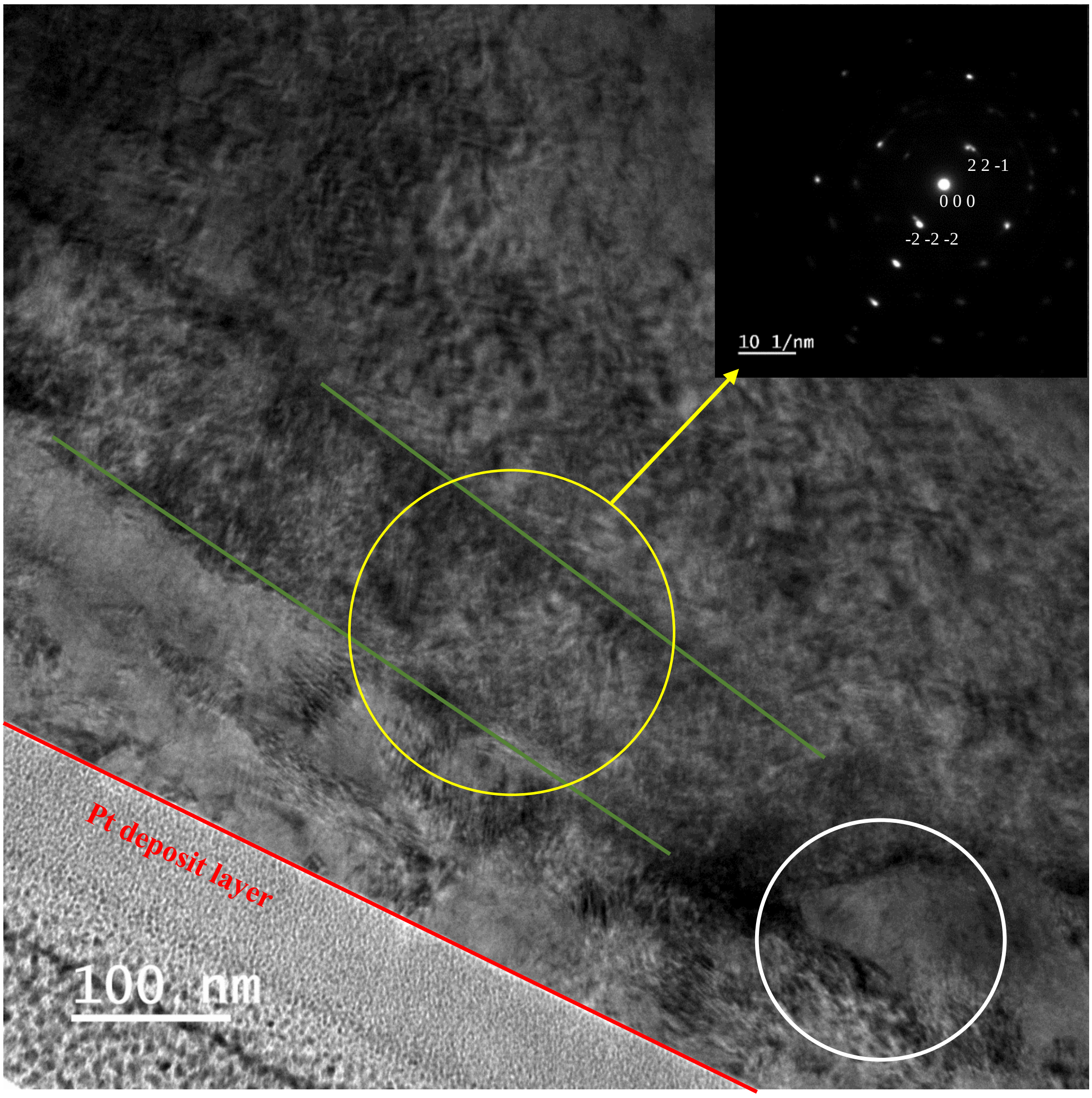

Figure 4.1 -TEM image on the surface site, the red line indicates the protecting Pt layer and sample surface, the green line is marking cluster grains, whilst the white circle is indicating the alternated orientation crystal structure. The yellow circle indicates where the electron diffraction image was taken.

At higher magnification, shown in Figure 4.2, near the surface, there exists evidence for parallel lines in the samples. These indicate there is some overlap between grains within the sample, but nevertheless still shows evidence for a high degree of crystallinity in the lattice. The diffraction image also indicates that this area has multiple grains, with differing orientations, with the diffraction pattern showing evidence for a polycrystalline structure. However, the diffraction pattern indicates that while there are multiple orientations visible, there is a degree of ordering in the lattice.

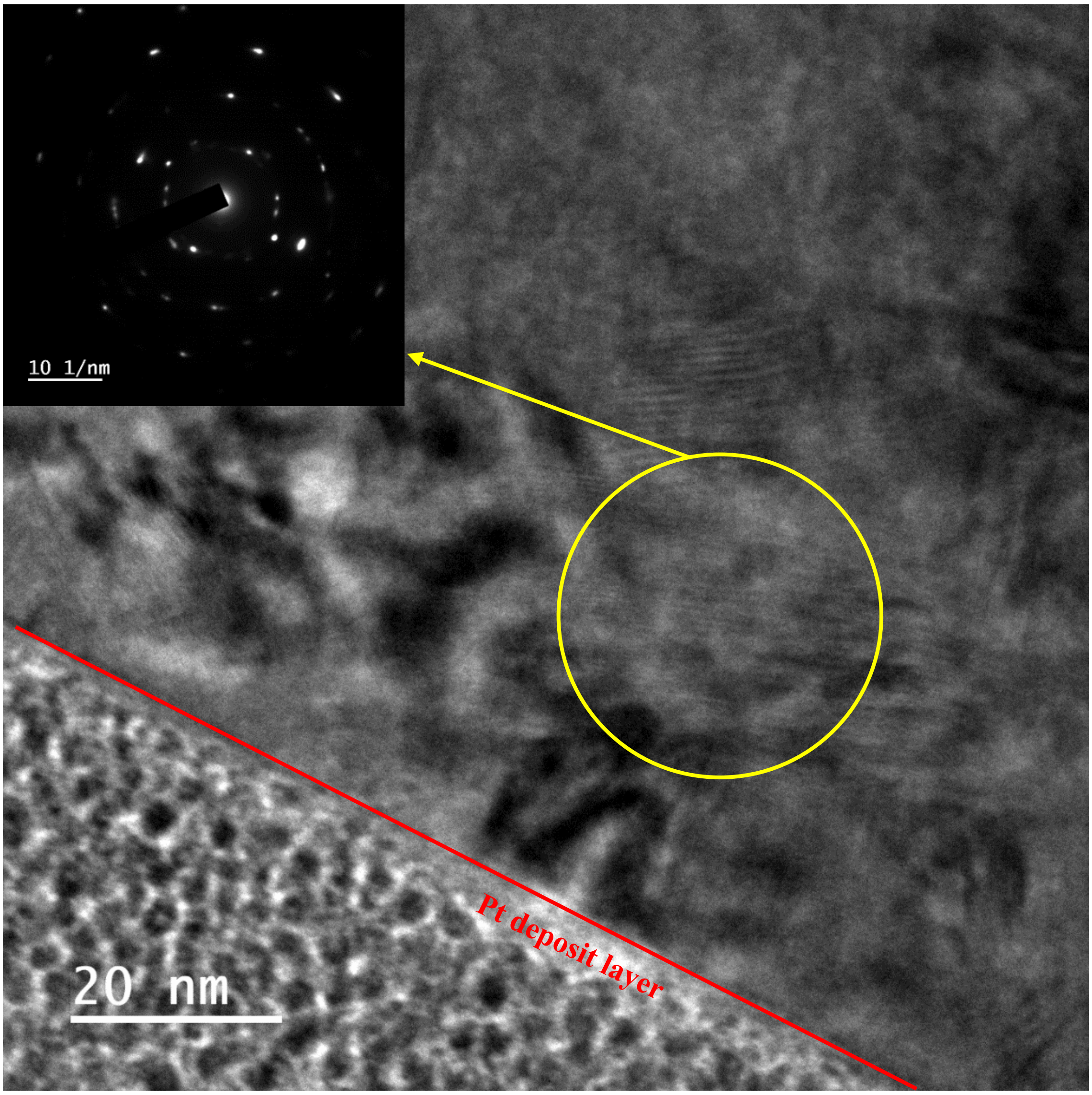

Figure 4.2- High magnification image near the surface area, the red line is the Pt protection layer, in the yellow circle there is interference pattern present. The yellow circle indicates where the electron diffraction image was taken.

When analysed at a depth of ~ 300nm depth, the TEM images, shown in Figure 4.3, show a structured atomic arrangement, with evidence for structural domains having formed. The grain boundary between these gains is not sharp, indicating a diffuse type of boundary is present. The diffraction image from this region suggests the grains are again single crystal structure in nature. This thinner sample has less interaction from the other parts of the material which have different orientations. The electron diffraction pattern, additionally shows less diffusion around the central spot, indicating, at least in this analysis there is less inherent disorder in the lattice at this depth.

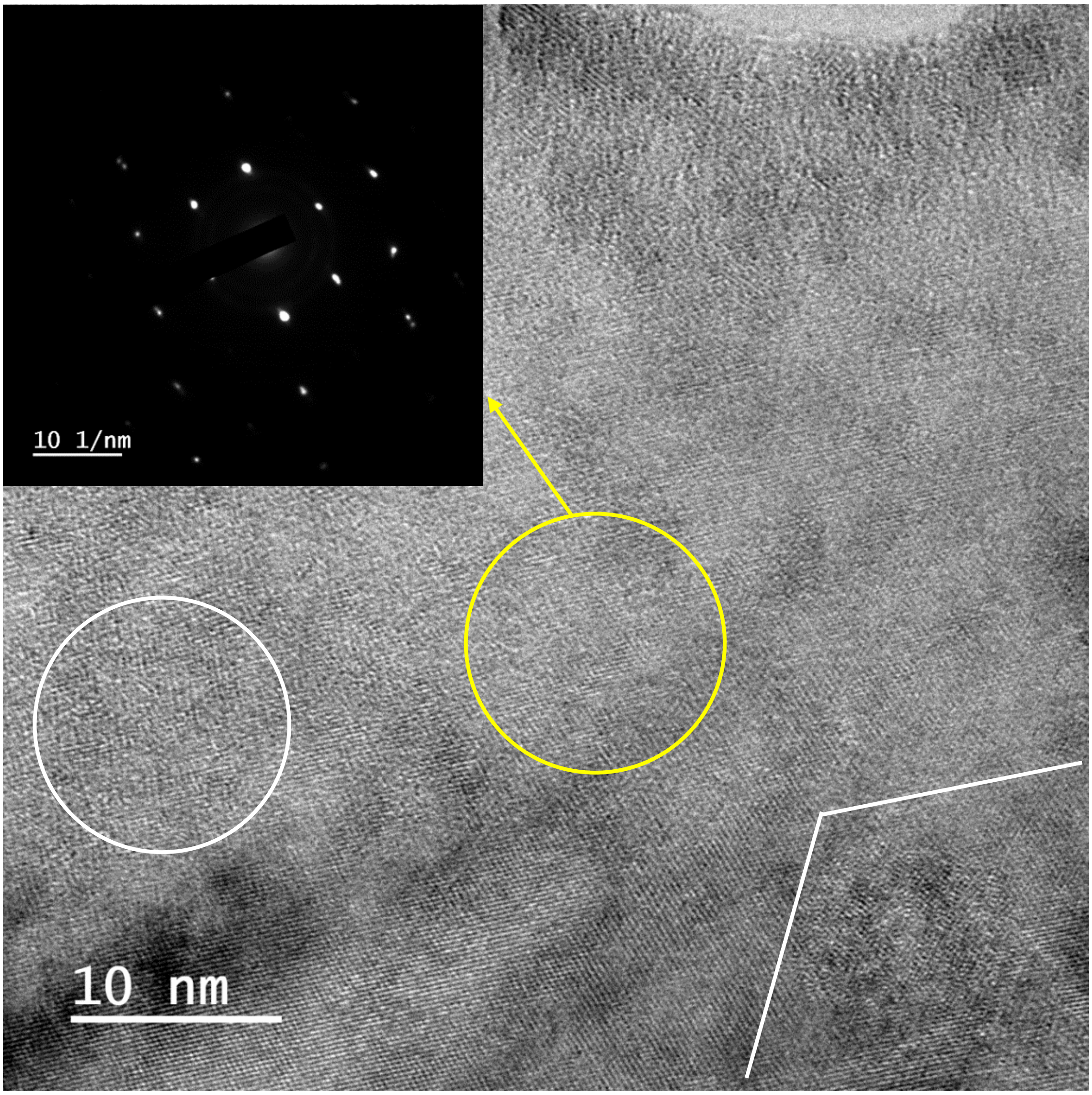

Figure 4.3 - TEM image from a depth of ~ 300nm, the white circle is showing the cross alignment of atom on this plan of view, the white line is indicating the transferring of crystal orientation from one direction to another. The yellow circle indicates where the electron diffraction image was taken.

4.1.2 3 MeV Ni ion implantation with 5 x 10^{15} ions cm^{-2}

Figure 4.4 shows a series of images taken from surface to a depth of approximately 2µm. Each section has the diffraction pattern image taken from the centre area as the selected area. It allows the tracing of microstructural shift with increasing depth, as with increasing depth the level of interaction with the ion beam will be different. As shown in the combined image, in the initial part (0 nm – 800 nm) the microstructure appears to be broadly crystalline in nature, with a diffraction pattern that shows a crystalline pattern, but with evidence for a weak diffuse ring pattern, indicating a level of disorder. In the deeper range (800 nm – 900 nm) the microstructure has shifted orientation with the diffraction spots starting to diffuse along the linear axis, at deeper depths the diffraction pattern remains similar until it reaches a grain boundary with a grain richer in Fe and Cr.

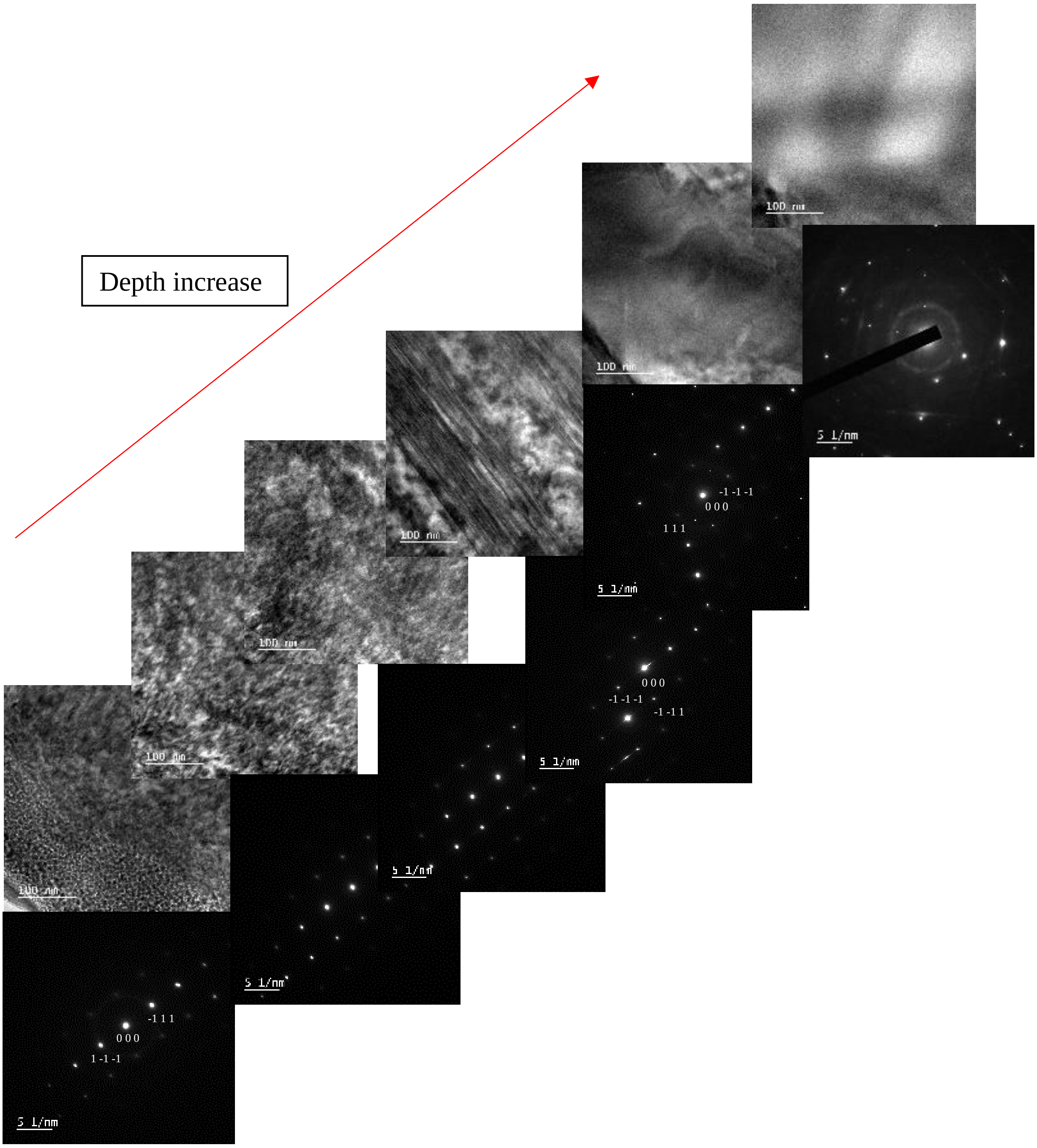

Figure 4.4 – Depth series of TEM images and electron diffraction patterns from the surface of 3 MeV Ni irradiated Co$_{1.5}$CrFeNi$_{1.5}$Ti$_{0.5}$Mo$_{0.1}$

Near the surface, and shallow depths, compared to the non-irradiated sample, the microstructure has significantly shifted as a consequence of the nickel ion implantation, shown in Figure 4.5. The multi-grain nature has vanished, indicating that the small grains which appeared in the non-irradiated sample have been removed. In the diffraction pattern, a diffuse ring has appeared, indicating the formation of a polycrystalline structure. This is key evidence of the high energy ions damaging the local microstructure.[30]

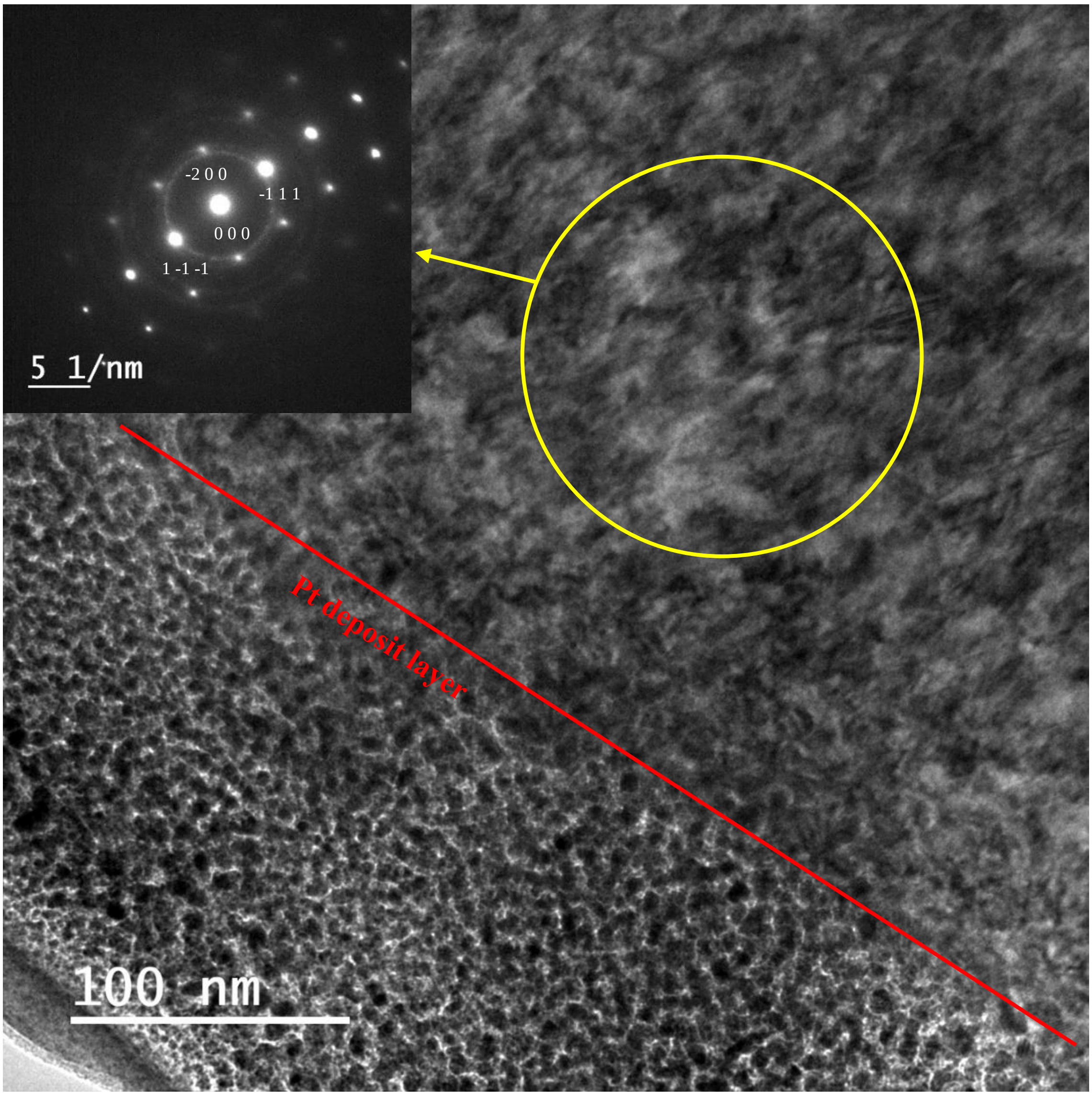

Figure 4.5 - TEM image from near the surface of Ni irradiated $Co_{1.5}CrFeNi_{1.5}Ti_{0.5}Mo_{0.1}$, the red line is Pt protection layer, and the yellow circle indicates where the electron diffraction pattern was recorded.

4.1.3 He overlap irradiation

He irradiation can induce a build-up of He within the sample, in the TEM image shown in Figure 4.6, tiny round spots are visible in the sample, which are not present in the unirradiated sample. This suggests the potential formation of small He bubbles within the lattice. The diffraction pattern again shows a diffuse ring around the central spot which indicates the formation of disorder within the lattice.

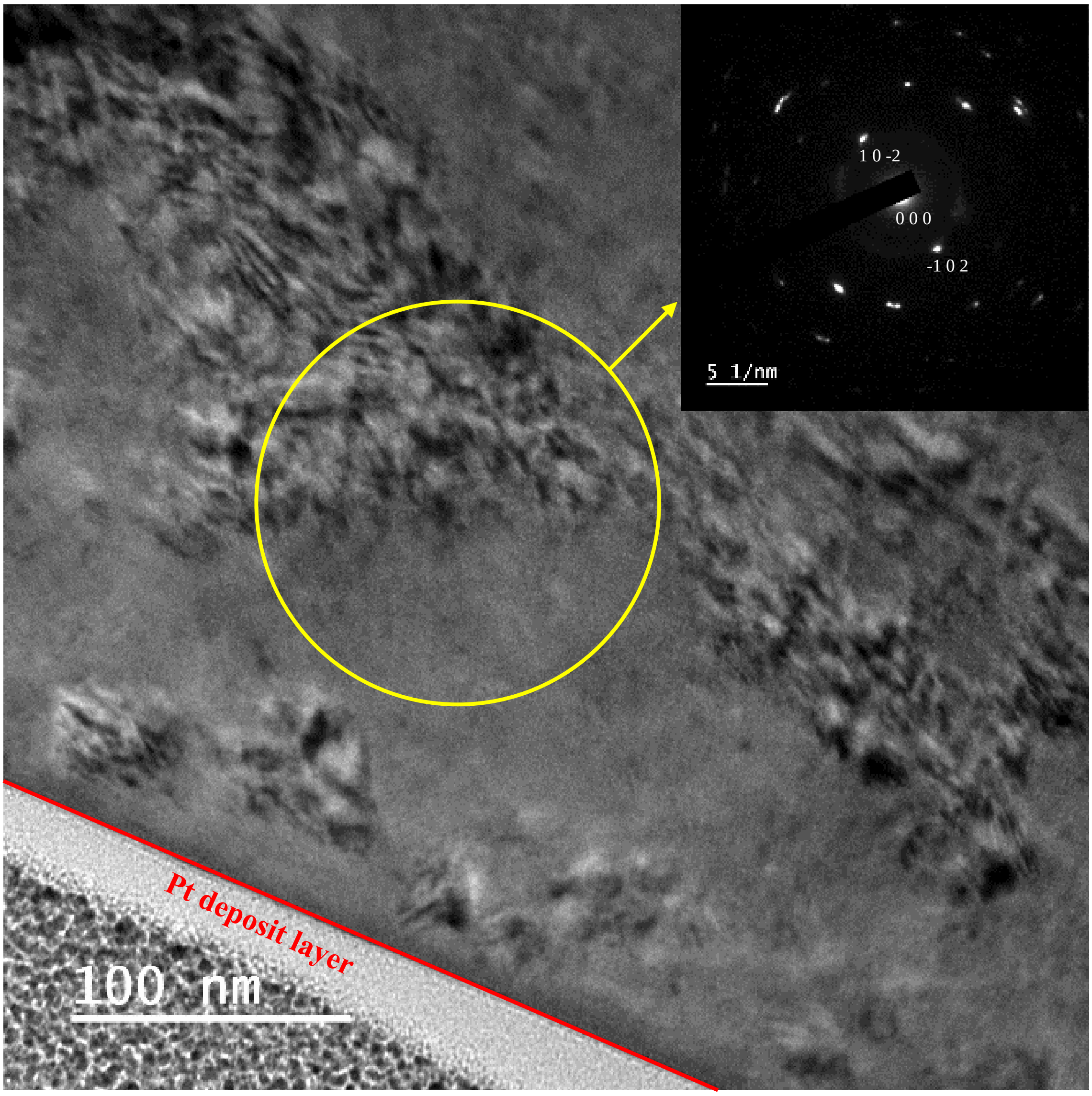

Figure 4.6 - TEM image recorded near the surface of He irradiated $Co_{1.5}CrFeNi_{1.5}Ti_{0.5}Mo_{0.1}$, the red line is Pt protection layer, and the yellow circle indicates where the electron diffraction pattern was obtained.

4.1.4 Energy Dispersive X-ray Analysis of $Co_{1.5}CrFeNi_{1.5}Ti_{0.5}Mo_{0.1}$

As can be seen in Figure 4.7, the EDX map indicates that the composition of the sample before irradiation is broadly homogenous. After irradiation by 3 MeV Ni, the EDX map Figure 4.8 again shows a broadly homogenous distribution of elements, although there is some evidence for banding within the sample that corresponds to a region that is Ni rich and Cr poor, although this change is only minor. After He irradiation, in Figure 4.9, He is not directly visible. However, in contrast, there are regions of Fe-Cr rich areas. This is unlikely to arise directly from He irradiation, rather from zoning during the initial sample melting during fabrication.

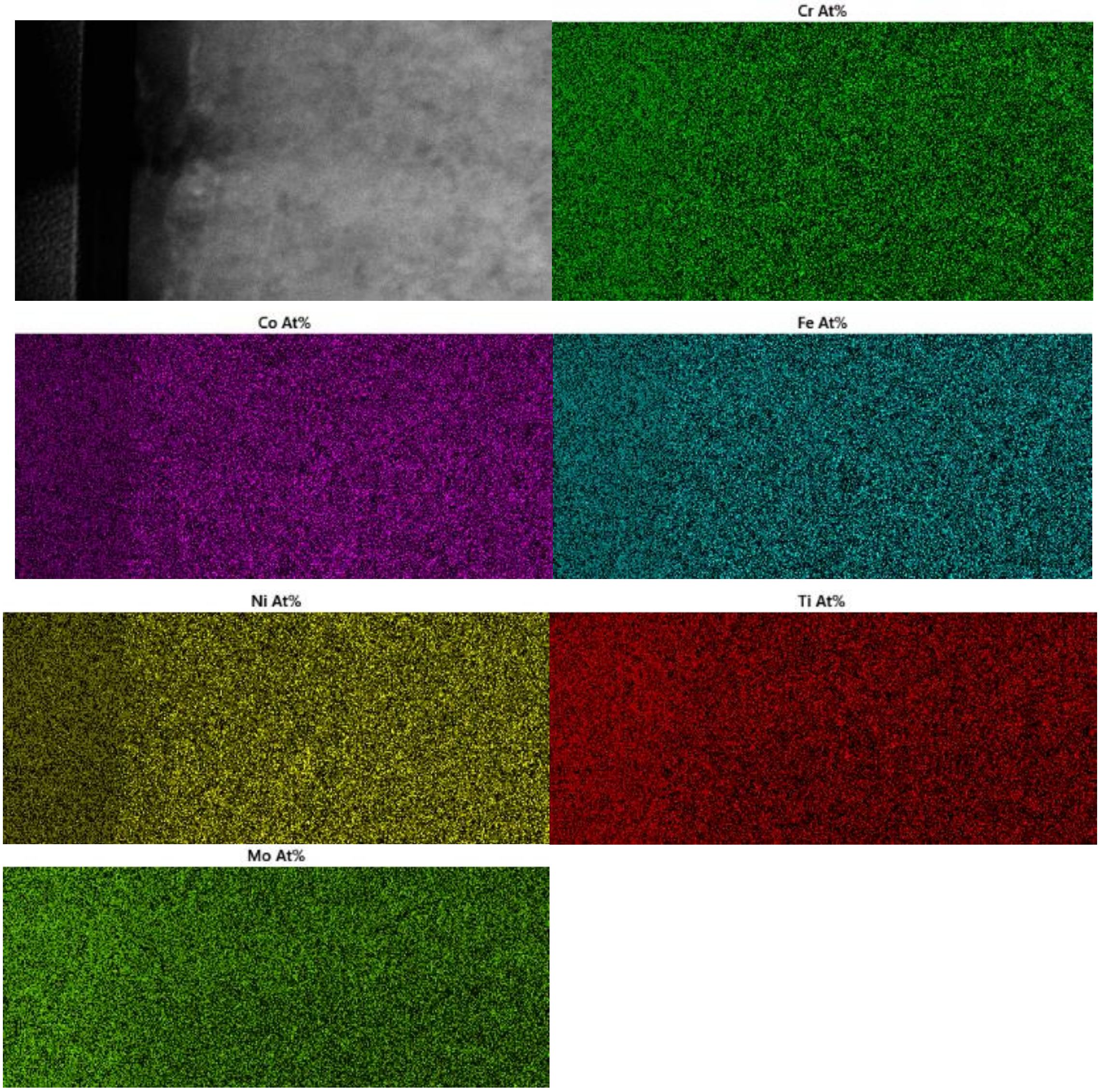

Figure 4.7 - EDX mapping of $Co_{1.5}CrFeNi_{1.5}Ti_{0.5}Mo_{0.1}$ prior to irradiation, the sample surface is on the left side

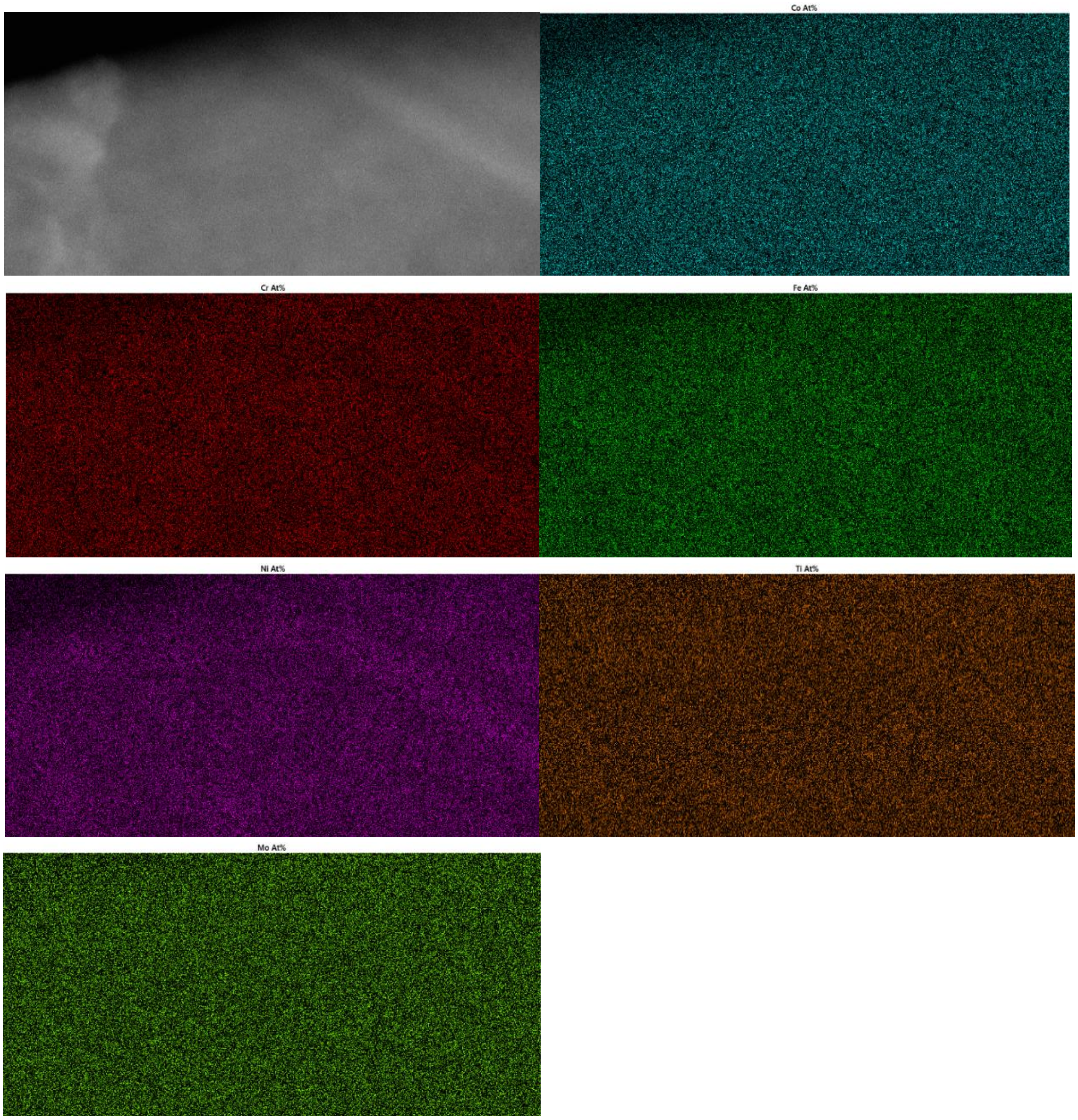

Figure 4.8 - EDX mapping of $Co_{1.5}CrFeNi_{1.5}Ti_{0.5}Mo_{0.1}$ after irradiation with 3 MeV Ni, the sample surface is on the left side

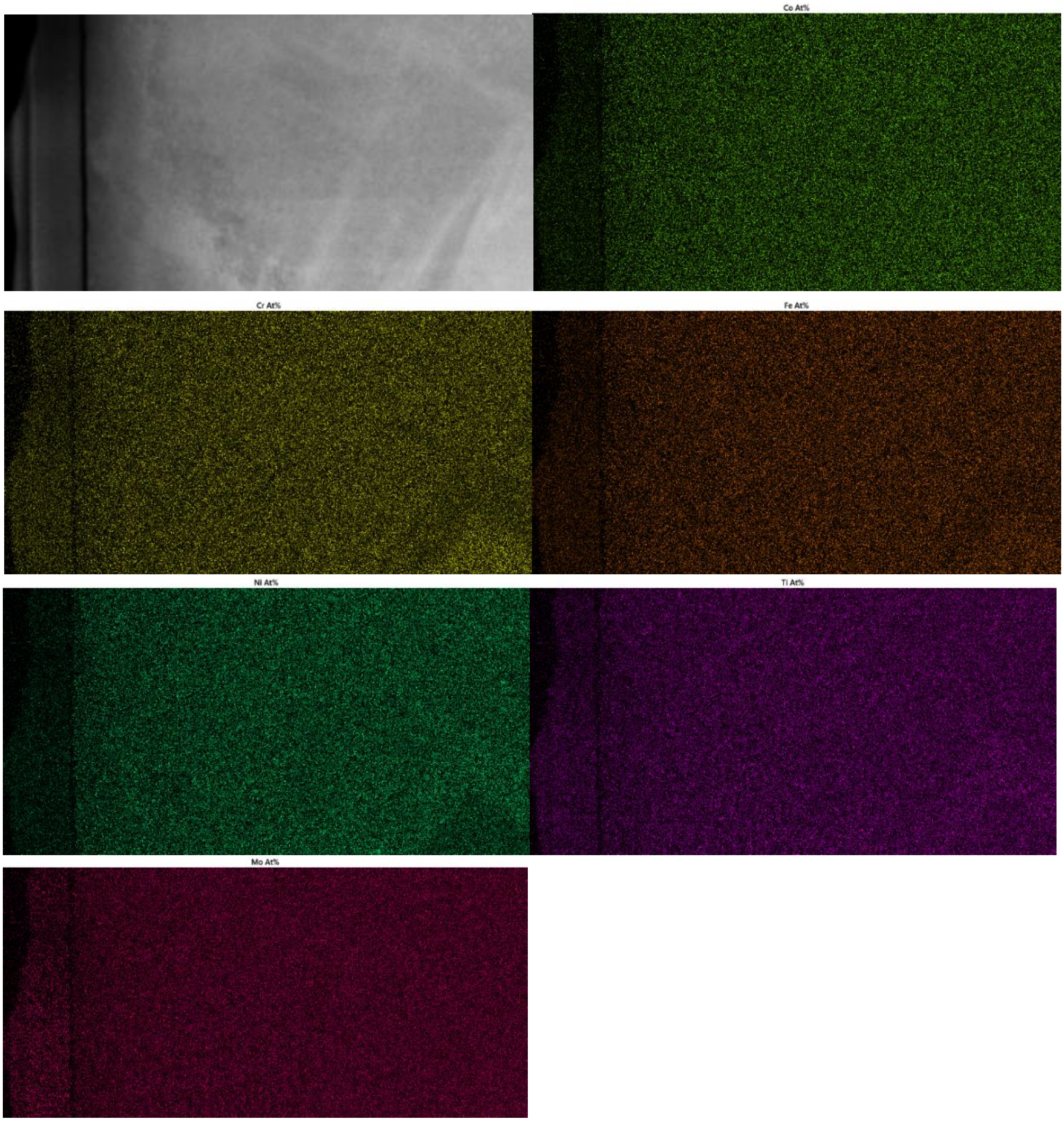

Figure 4.9 - EDX mapping of $Co_{1.5}CrFeNi_{1.5}Ti_{0.5}Mo_{0.1}$ after He irradiation, the sample surface is on the left side.

4.2 TEM analysis of CoCrCuFeNi

4.2.1 Pre-Irradiation Analysis

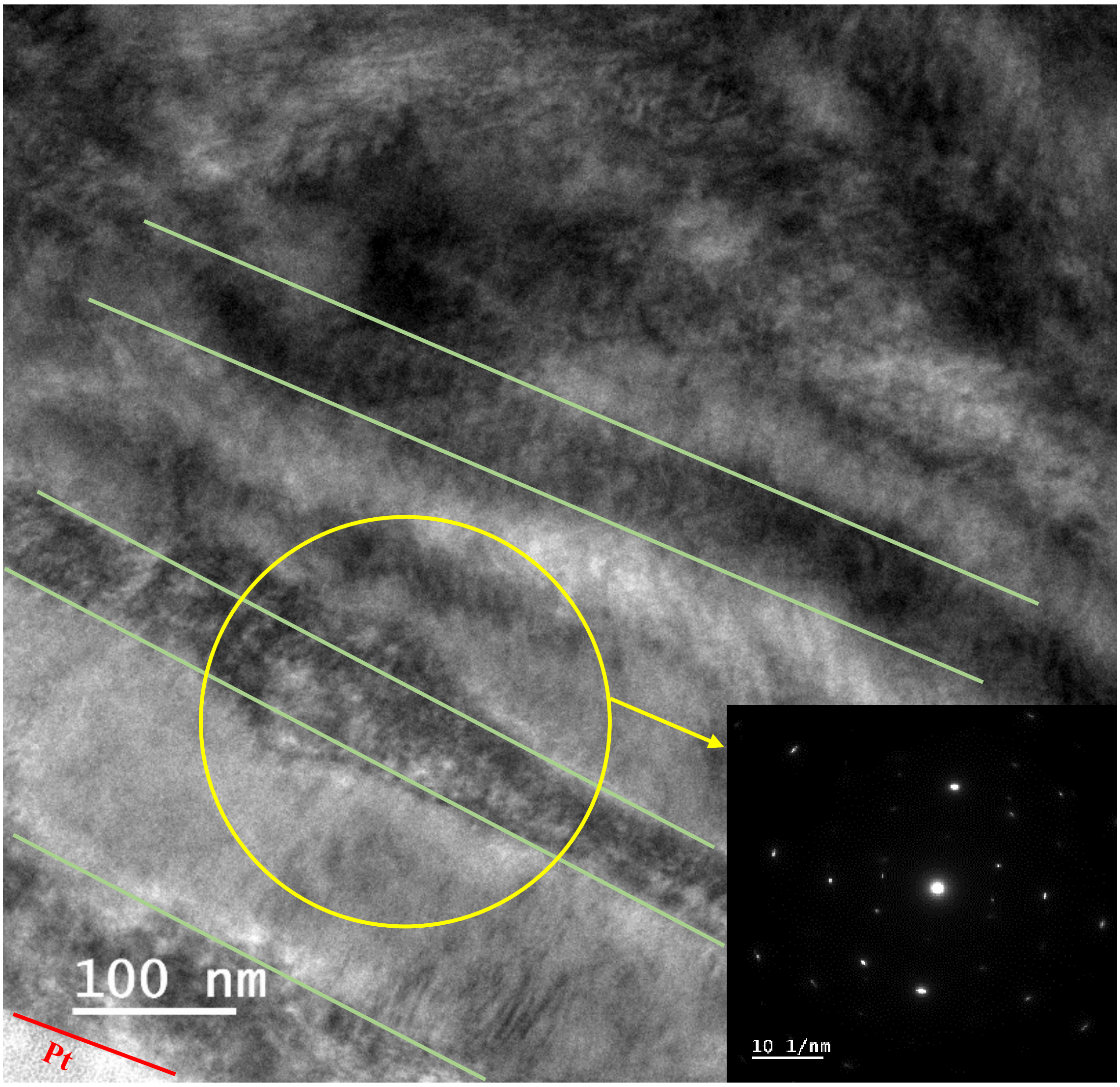

Figure 4.10 - TEM image recorded near the surface from CoCrCuFeNi, the red line is Pt protection layer, and the yellow circle indicates where the electron diffraction pattern was obtained.

The original CoCrCuFeNi sample shows evidence for elemental enrichment, as in Figure 4.10, with banding appearing between about 240 nm and 640nm. The electron diffraction shows evidence for two overlapping patterns. These observations could arise from multiple sources, such as an uneven distribution of elements during, or arising. From synthesis, or from mechanical damage during the polishing process.

4.2.2 3 MeV Ni ion implantation with 5 x 10^{15} ions cm^{-2}

After irradiation with 3 MeV Ni ions TEM analysis shows the formation of tiny crystals from near the surface to ~400 nm inside the material, Figure 4.11. The diffraction pattern shows diffusion radially, indicating there are multiple small grains of similar orientation but which may slightly differ in composition, shown by the diffuse nature of the spots. This phenomenon also can be found in the T.Nagasa' research. [75]

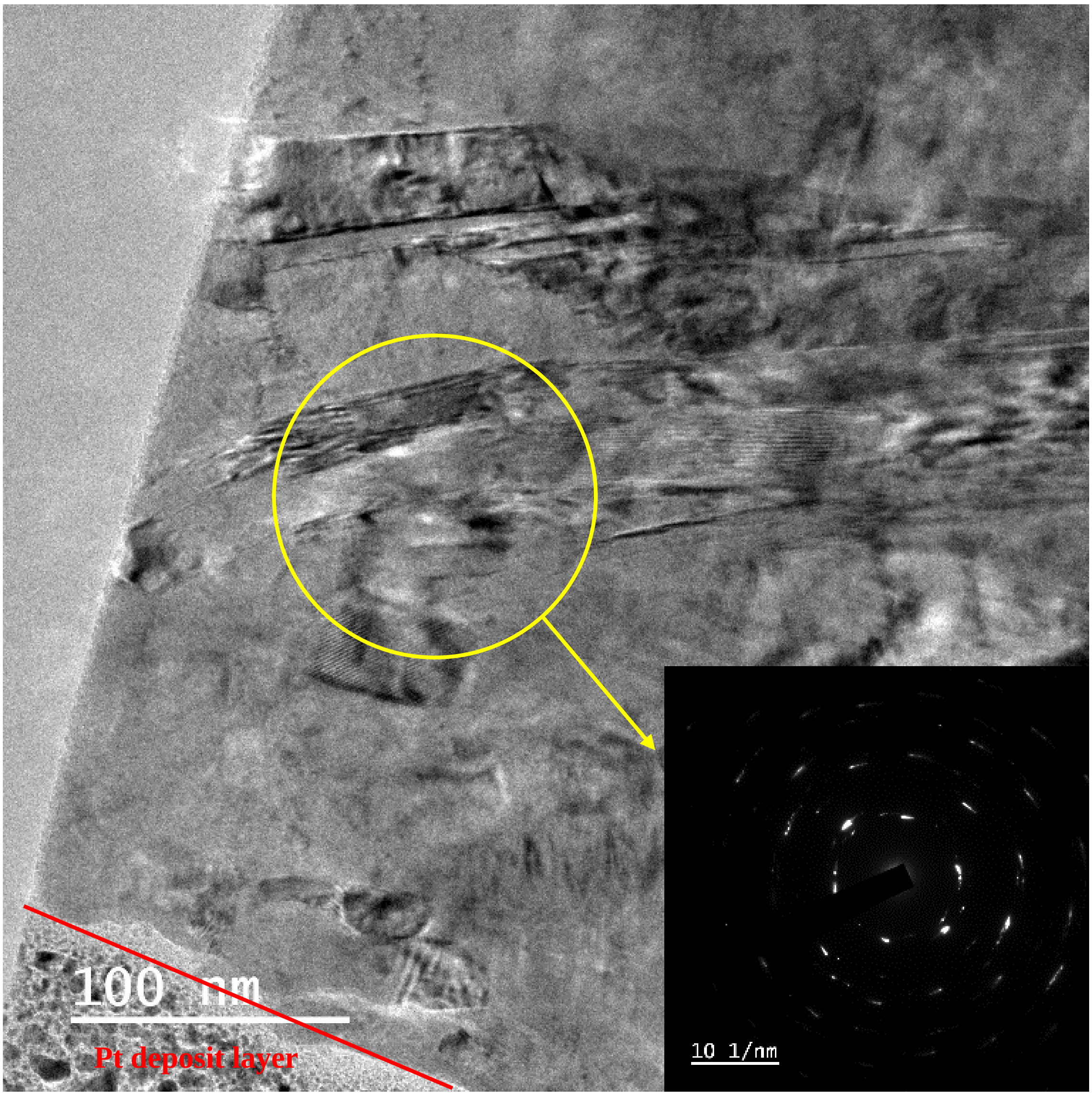

Figure 4.11 - TEM image recorded near the surface of Ni irradiated CoCrCuFeNi, the red line is the Pt protection layer, and the yellow circle indicates where the electron diffraction pattern was obtained.

If a darkfield image is compared with a brightfield image in Figure 4.12, there are significant numbers of small crystals, near the surface. These grains seem to form a mosaic, polygonal rather than rounded in shape, with a size range from 20 × 80 nm, through to 50

× 120 nm. These grains then appear in the diffraction patterns, giving rise to both pattern overlap, and sub-dot formation in individual diffraction spots. [75] These again show that the system has formed grains which are close in orientation but show evidence for damage and disorder.

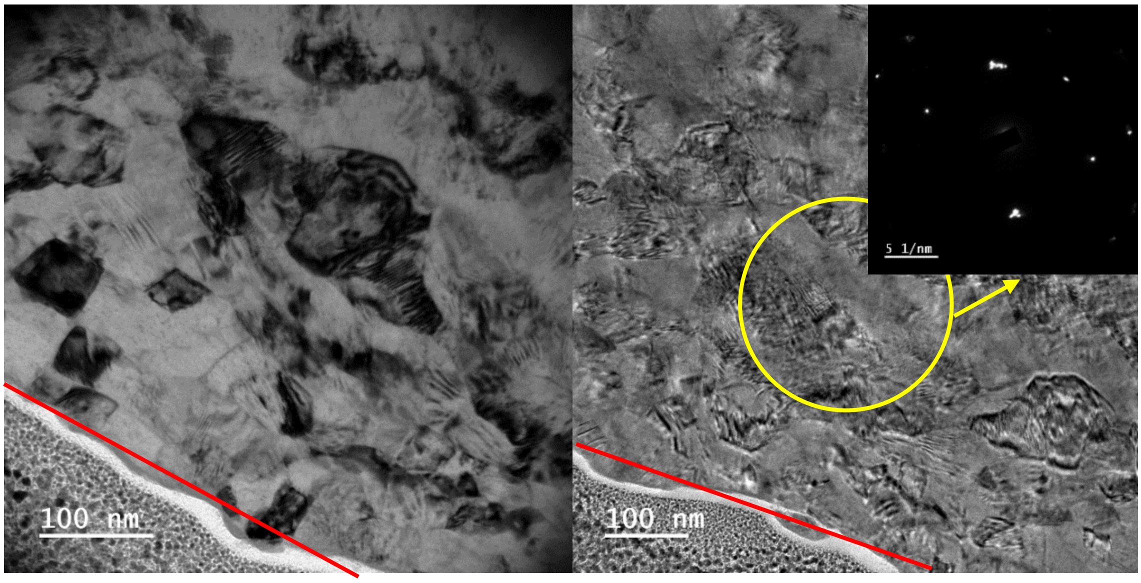

Figure 4.12 - TEM image recorded near the surface from Ni irradiated CoCrCuFeNi, the red line is Pt protection layer, and the yellow circle indicates where the electron diffraction pattern was obtained.

4.2.3 He overlap irradiation

As with other samples, there is evidence for small spots within the TEM image, again indicating the potential for He bubble formation during irradiation, as showing in Figure 4.13. However, there is no sign of the formation of the multiple tiny crystals, similar to that found after Ni irradiation. The diffraction pattern showed no evidence for diffuse scattering and compares well with that from an unirradiated sample.

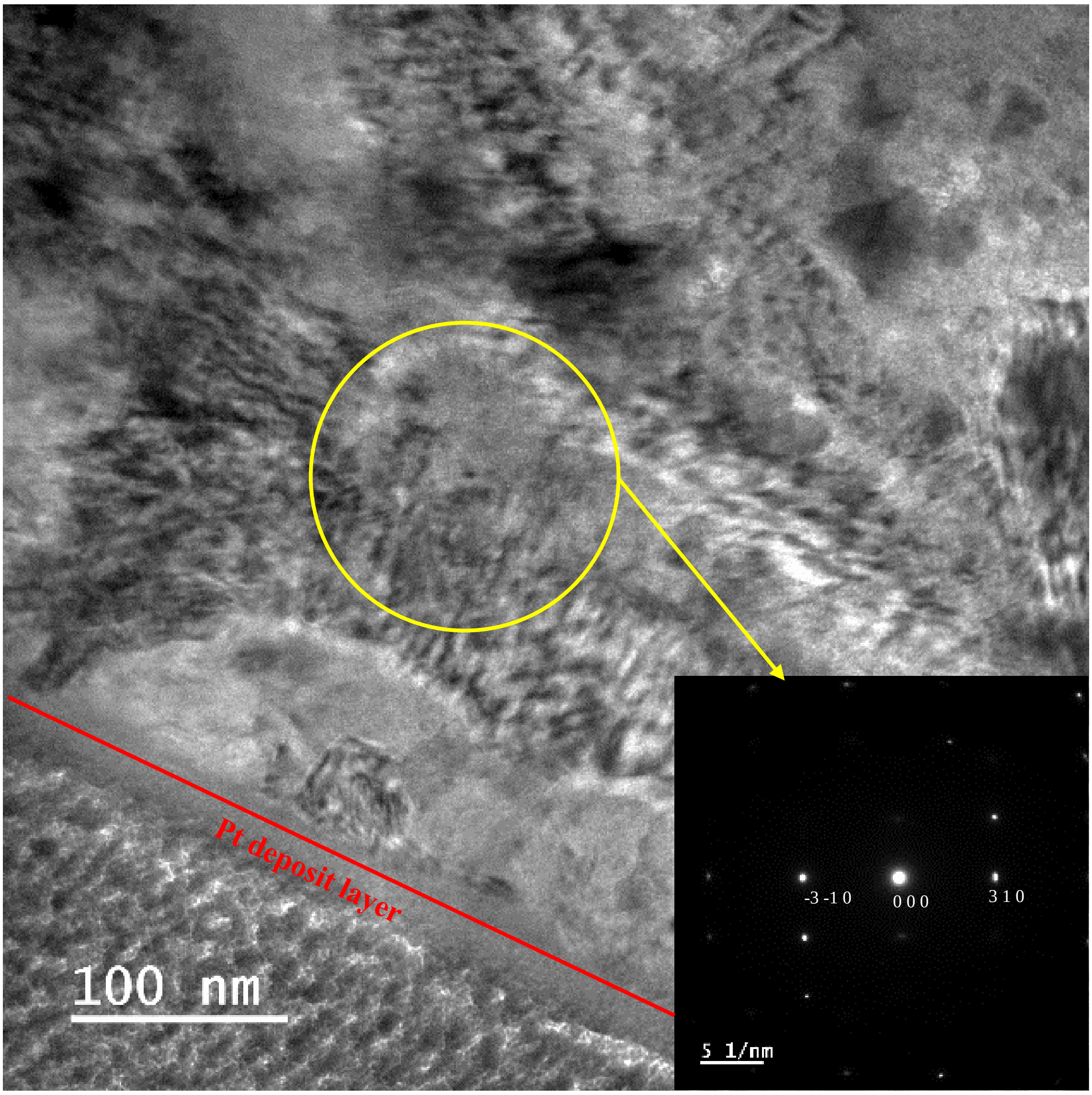

Figure 4.13 - TEM image recorded near the surface from He irradiated CoCrCuFeNi, the red line is Pt protection layer, and the yellow circle indicates where the electron diffraction pattern was obtained.

4.2.4 Energy Dispersive X-ray Analysis of CoCrCuFeNi

The original sample of CoCrCuFeNi, Figure 4.14 shows that the distribution of elements is not fully homogenous across the sample, with a region rich in Cu and slightly deficient in Fe. Judging by the shape it was not formed by a eutectic formation, rather through insufficient mixing and melting during the synthesis process. After irradiation with Ni, as showing in Figure 4.15, a different area of the sample showed a more homogenous distribution of elements, with no noticeable shifting through the irradiation affected zone. Even with the formation of multiple grains at ~ 300nm from the surface, they still share a similar elemental composition. After He irradiation, several dark round shape shadow regions appeared on the He irradiated sample, Figure 4.16. However, within the EDX mapping, this area has a seemingly uniform distribution of elements. Which when compared to the original sample, except for the Cu rich area, the distribution of elements is the same both before and after the He irradiation.

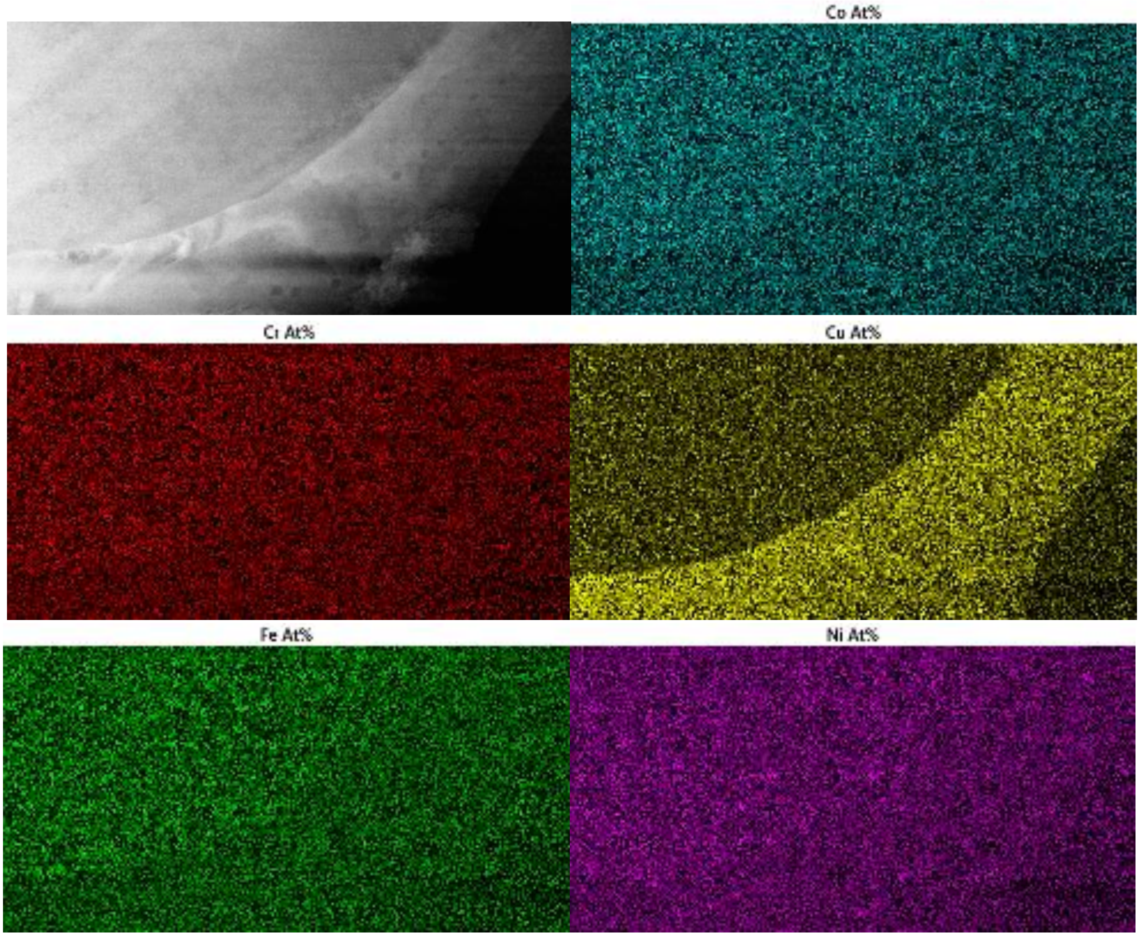

Figure 4.14 - EDX elemental maps of CoCrCuFeNi prior to irradiation, the sample surface is on the left side

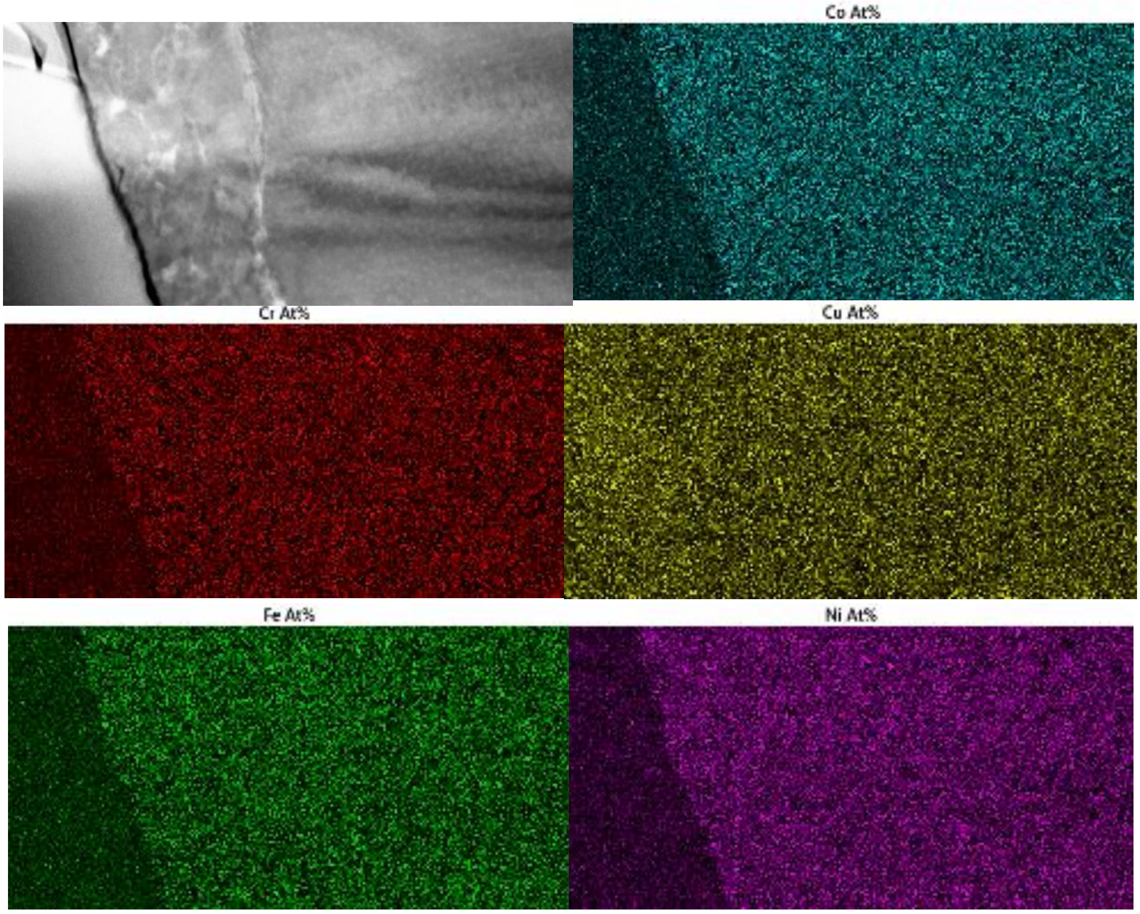

Figure 4.15 - EDX elemental maps of CoCrCuFeNi after irradiation with 3 MeV Ni, the sample surface is on the left side corner

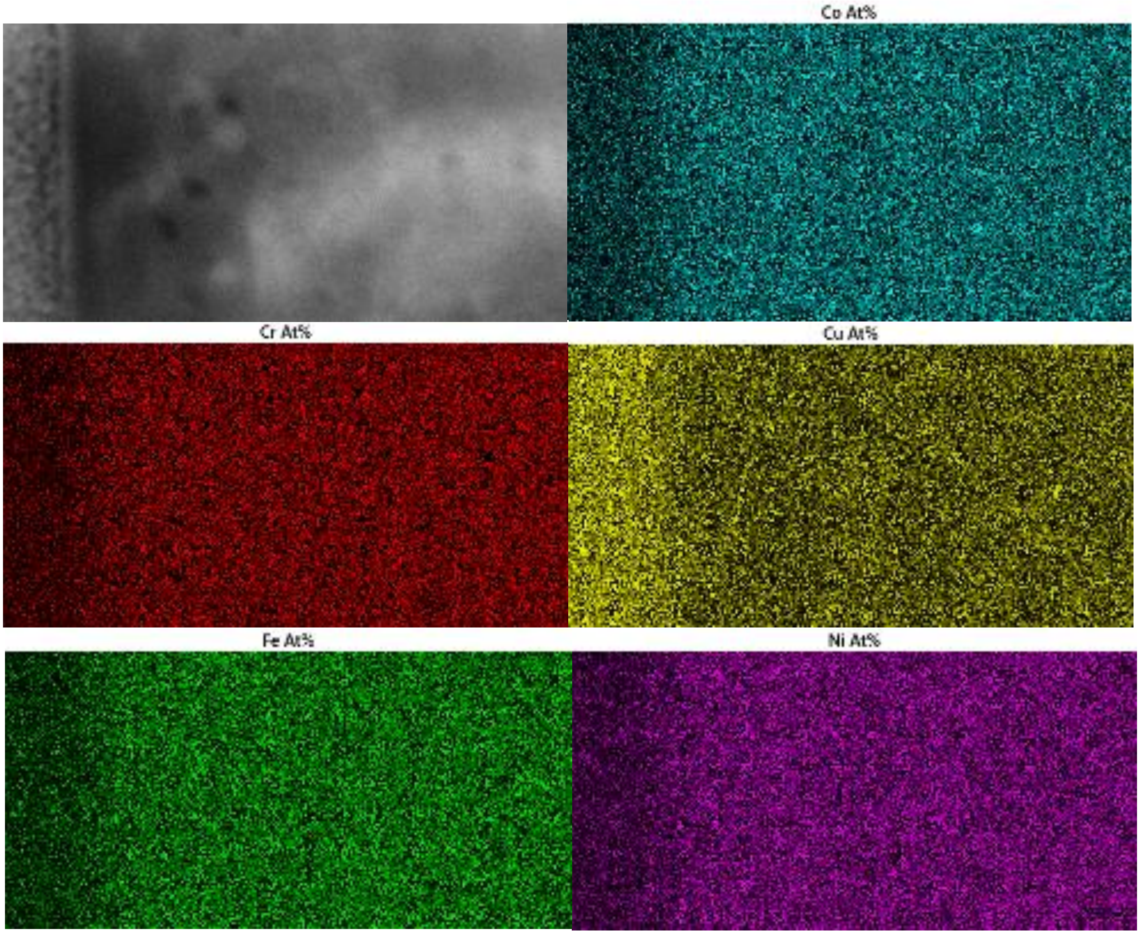

Figure 4.16 - EDX elemental maps of CoCrCuFeNi after He irradiation, the sample surface is on the left side

4.3 TEM analysis of TaNbHfZrTi

4.3.1 Pre-Irradiation Analysis

For a non-irradiated sample of TaNbHfZrTi, as in Figure 4.17, there was no clear difference between the surface and deeper depths. There was however a line shape shadow visible at ~ 200 nm. The diffraction pattern from near the surface area however is clean, with no evidence for diffusion. [76]

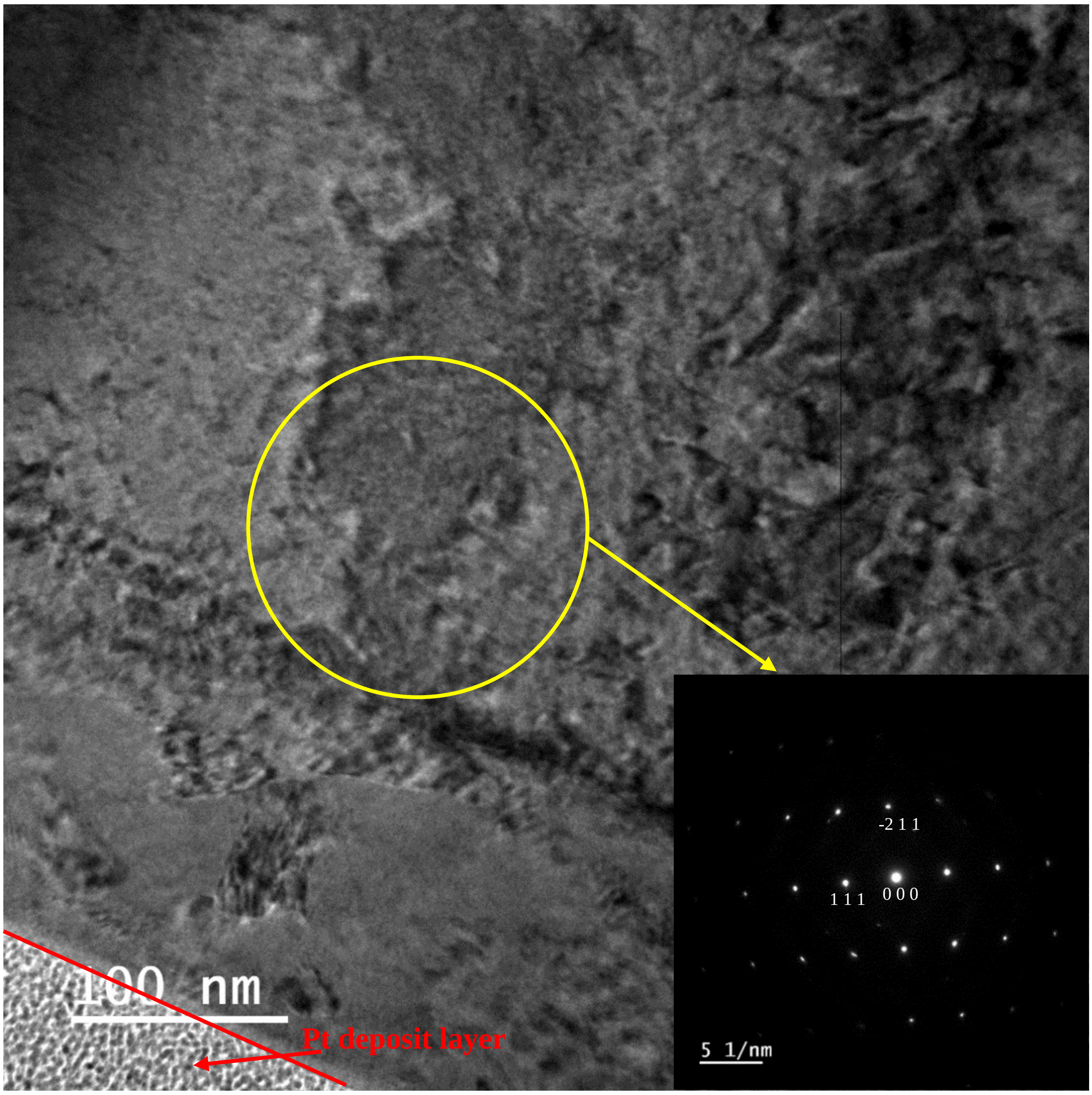

Figure 4.17 - TEM image recorded near the surface from TaNbHfZrTi, the red line is the Pt protection layer, and the yellow circle indicates where the electron diffraction pattern was obtained.

In an alternative image from another part of the sample, Figure 4.18, the sample appeared more uniform. However, the dark line, this time at ~ 125nm is still present, seemingly across the sample. With the help of the beam stop applied to the diffraction image, linear diffusion connecting the spots around the centre spot can be seen. This diffusion could be compositional or ordering in nature. However, without further information it would be difficult to identify the exact nature of the diffusion. [76]

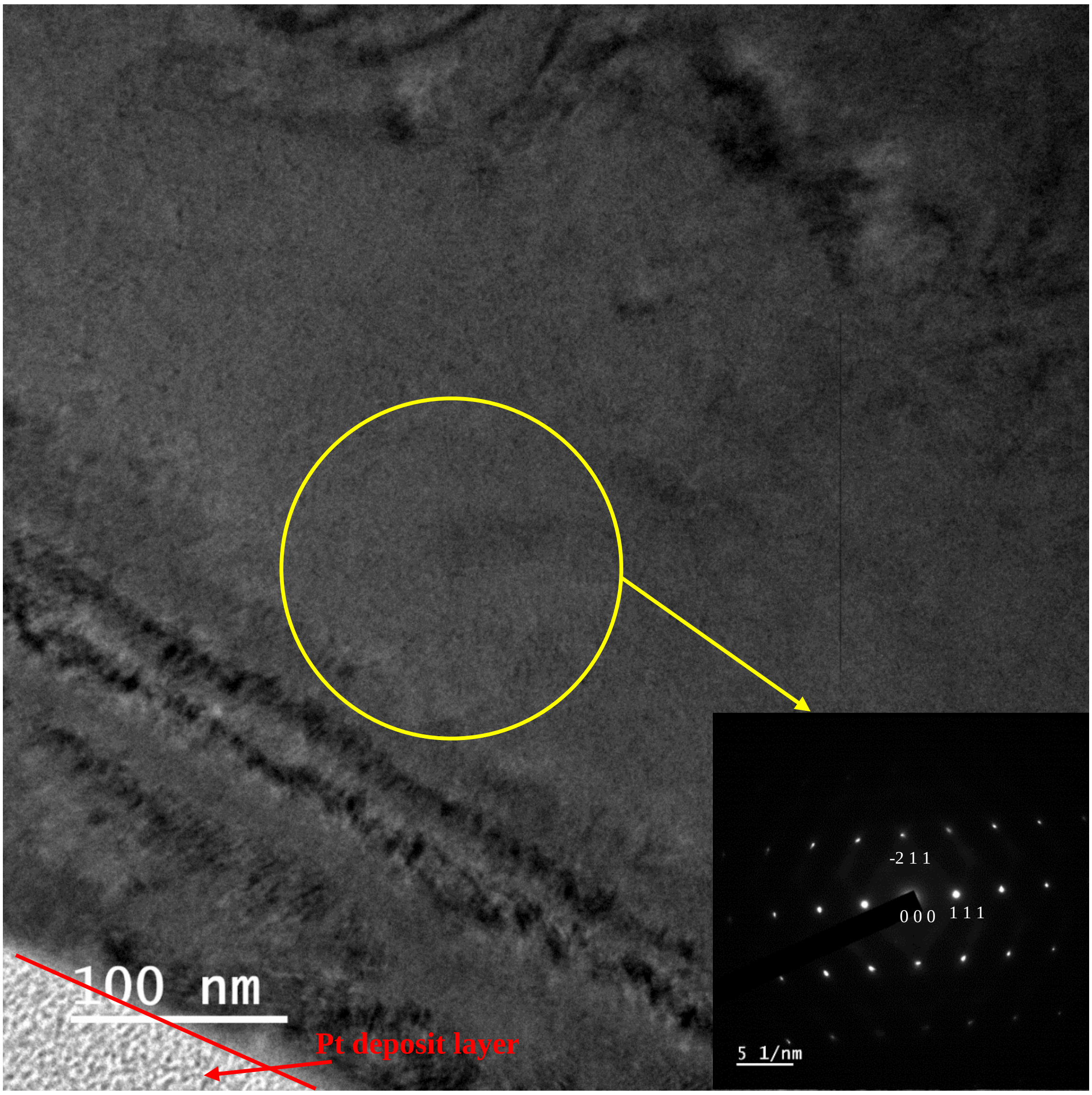

Figure 4.18 - TEM image recorded near the surface, the red line is Pt protection layer, and the yellow circle indicates where the electron diffraction pattern was obtained.

4.3.2 3 MeV Ni ion implantation with 5 x 10^{15} ions cm^{-2}

After irradiation with Ni ions, there were significant numbers of small grains found in the irradiation zone, in Figure 4.19. Compared to the as-cast sample, the homogeneity of the Ni irradiated sample was significantly reduced. The dark line which appeared in the as-cast sample can no longer be spotted in the Ni irradiated sample. This vanishing could indicate that the original orientation of atoms has been significantly modified by the irradiation by Ni ions. The diffraction image shows a different pattern from the as-cast sample, with a pattern indicating multiple grains/orientations having been formed, with a significant degree of disorder. This disorder is indicated within the pattern as diffuse lines formed in the pattern.

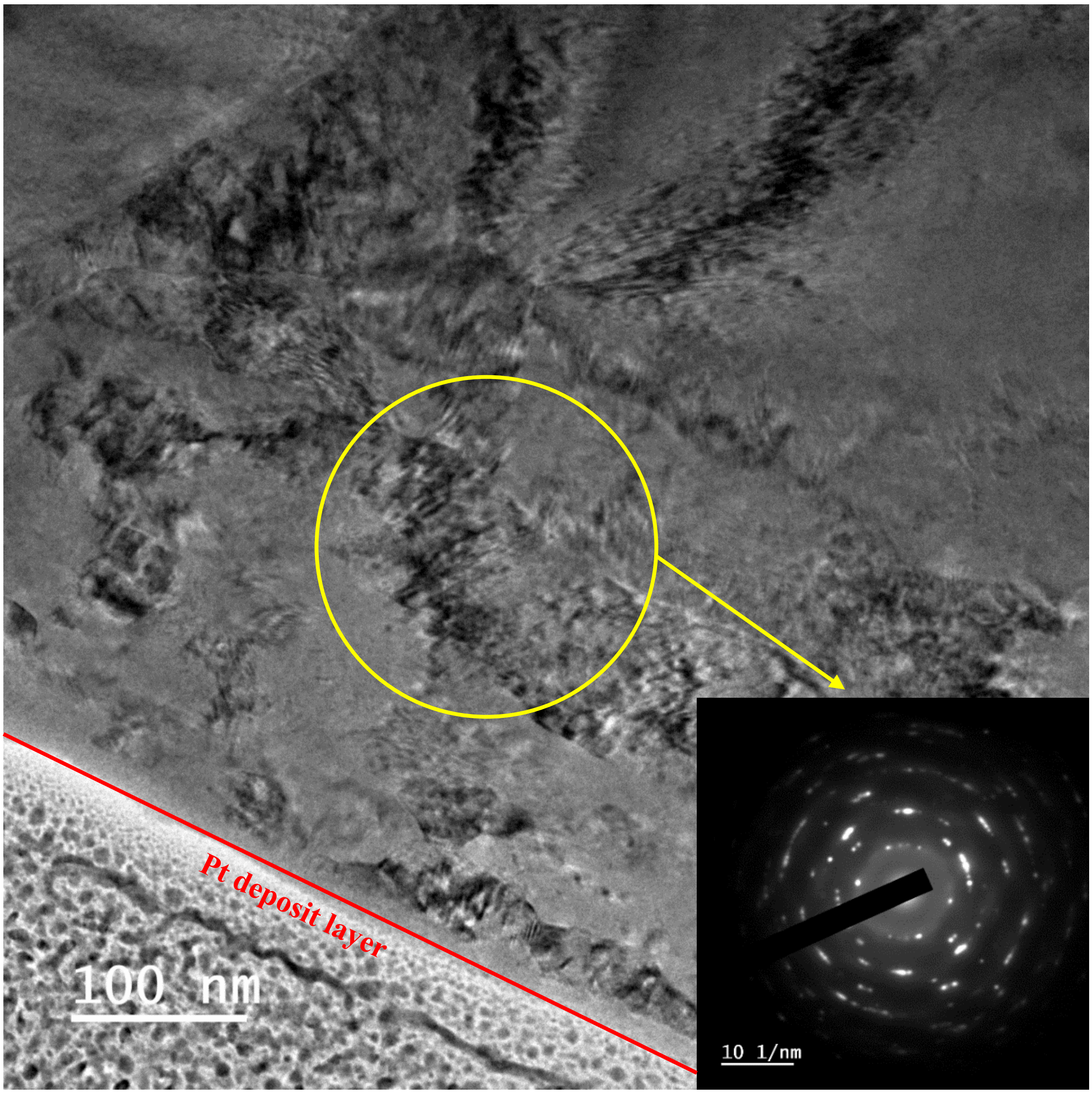

Figure 4.19 - TEM image recorded near the surface from Ni irradiated TaNbHfZrTi, the red line is Pt protection layer, and the yellow circle indicates where the electron diffraction pattern was obtained.

4.3.3 He overlap irradiation

It was difficult to identify direct evidence for He induced change near the surface, present in Figure 4.20, there was also no evidence for grain overlay seen in other irradiations either.

The diffraction pattern shows similar trends to the as-cast sample. There is some evidence for diffuse scattering, but this is faint, and possibly indicates a very low level of disorder has formed within the lattice.

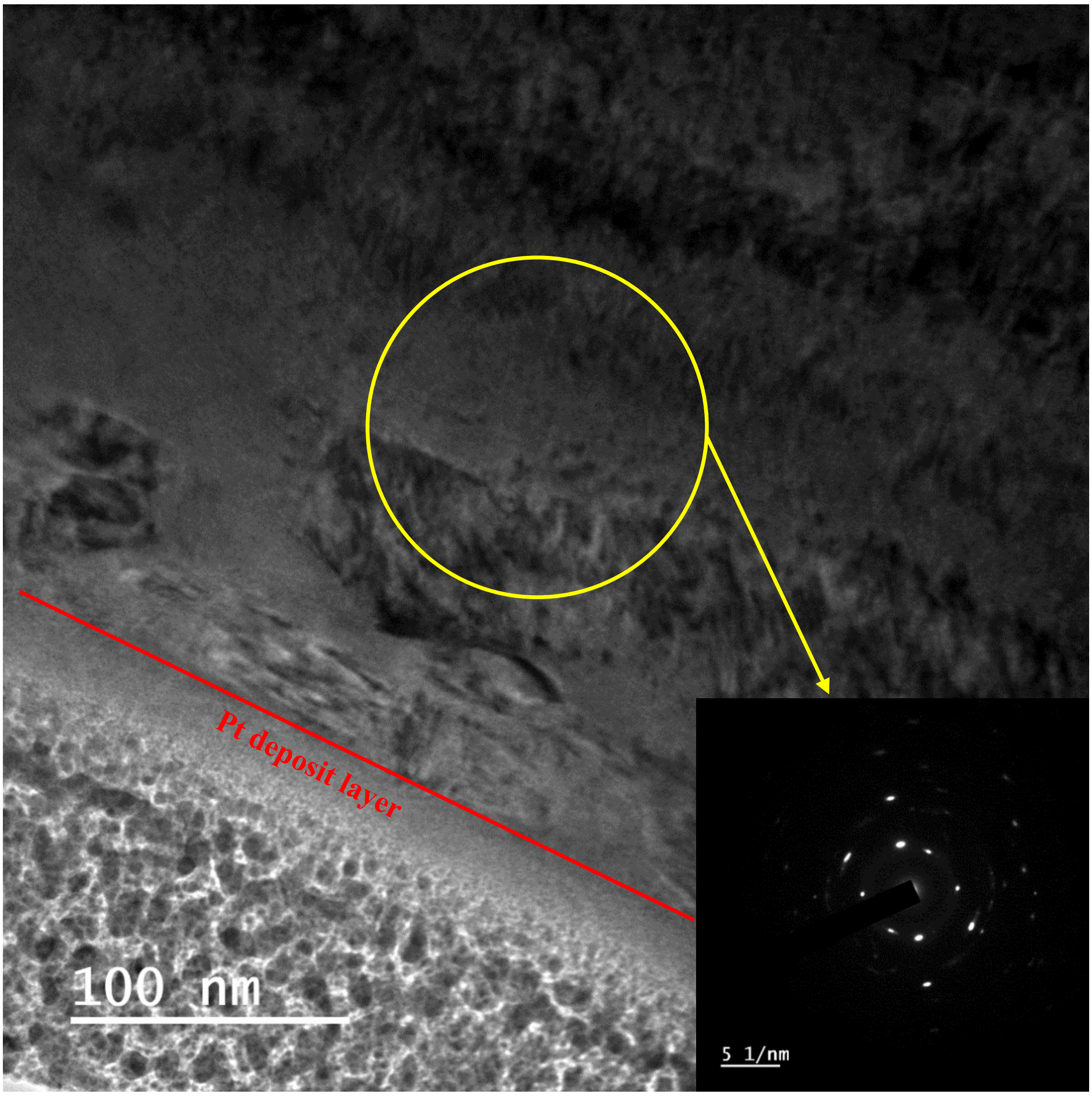

Figure 4.20 - TEM image recorded near the surface of He irradiated TaNbHfZrTi, the red line is Pt protection layer, and the yellow circle indicates where the electron diffraction pattern was obtained.

Upon close inspection, at a higher magnification, in Figure 4.21, the round shape similar to the other He irradiated samples was found. Again, in the diffraction pattern a weak diffuse ring was visible, indicating that some disorder might be present, but it would be difficult to say it was a large volume.

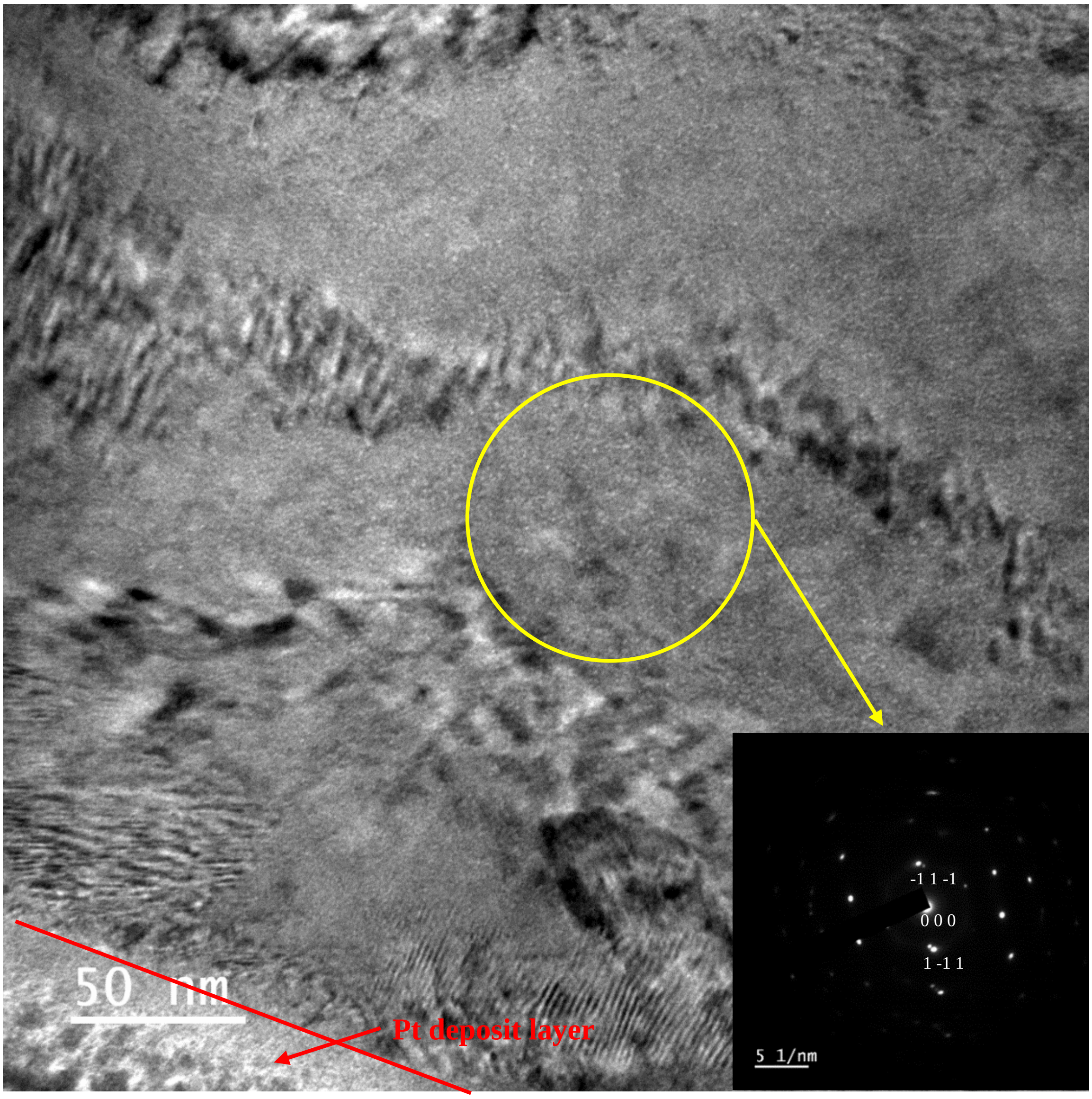

Figure 4.21 - TEM image recorded near the surface, from He irradiated TaNbHfZrTi, the red line is Pt protection layer, and the yellow circle indicates where the electron diffraction pattern was obtained.

In a second sample examined, there is significant formation of round shape features within the He irradiated sample. However, it was not easily identifiable as direct evidence of formation of the helium ‘bubble’, even after analysing with a through focus series, of under, on and overfocus analysis.

4.3.4 Energy Dispersive X-ray Analysis of TaNbHfZrTi

As can be seen in Figure 4.22, prior to irradiation, this sample shows a uniform distribution of element across the observed area. After irradiation with 3 MeV Ni, in Figure 4.23, there is evidence for some partitioning due to the formation of Hf-Zr rich regions, that can be favoured in formation. Similar phenomena have been spotted in the literature, and could arise from insufficient mixing during synthesis, as Hf has a high melting point (2233 ˚C) which may not have fully melted [45]. However, other than this Hf-Zr region, the remainder of the sample was homogenous in nature. After irradiation with He, in Figure 4.24, similar to the Ni irradiation, the composition inside the irradiation affected zone shows no noticeable change in the EDX image. Although the equipment is unable to detect the He directly, the irradiation itself does not leave any evidence for changes in element distribution.

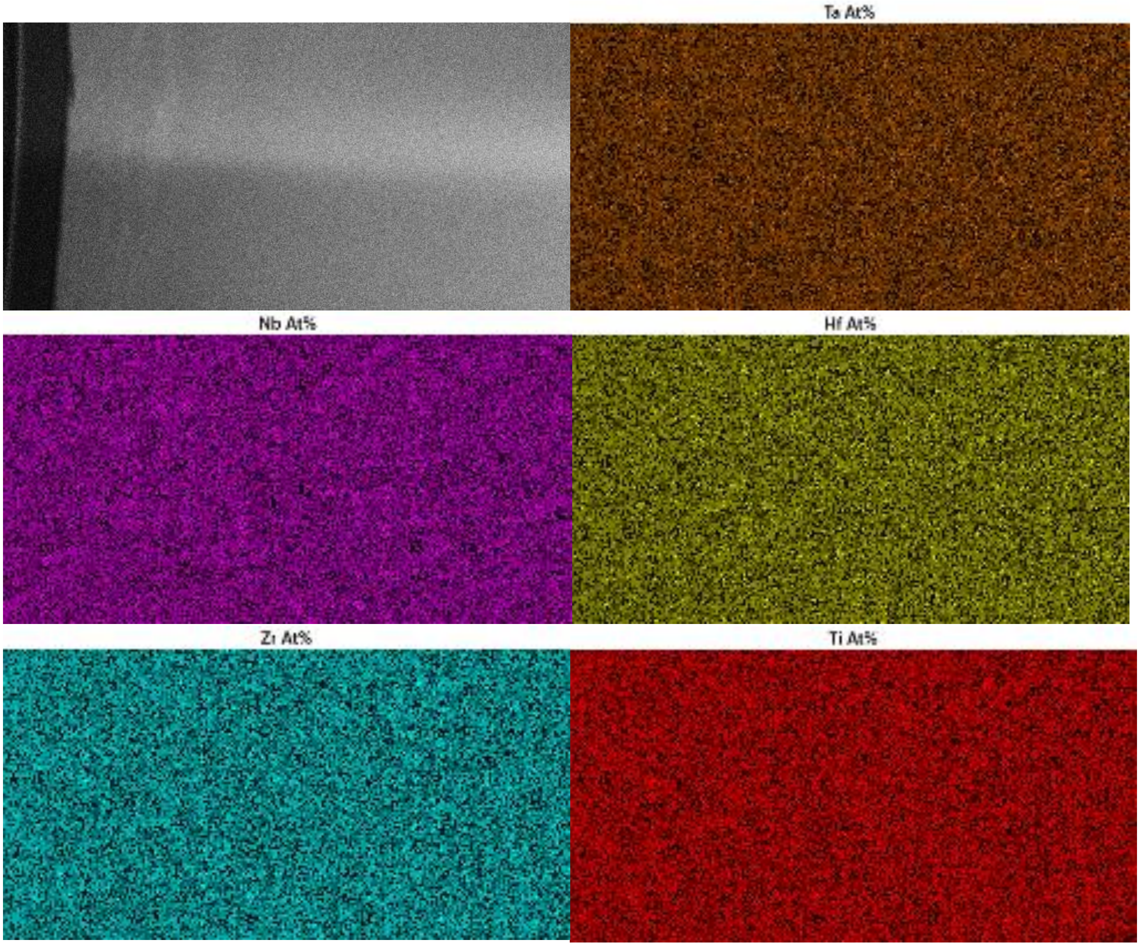

Figure 4.22 - EDX elemental maps of TaNbHfZrTi prior to irradiation, the sample surface is on the left side

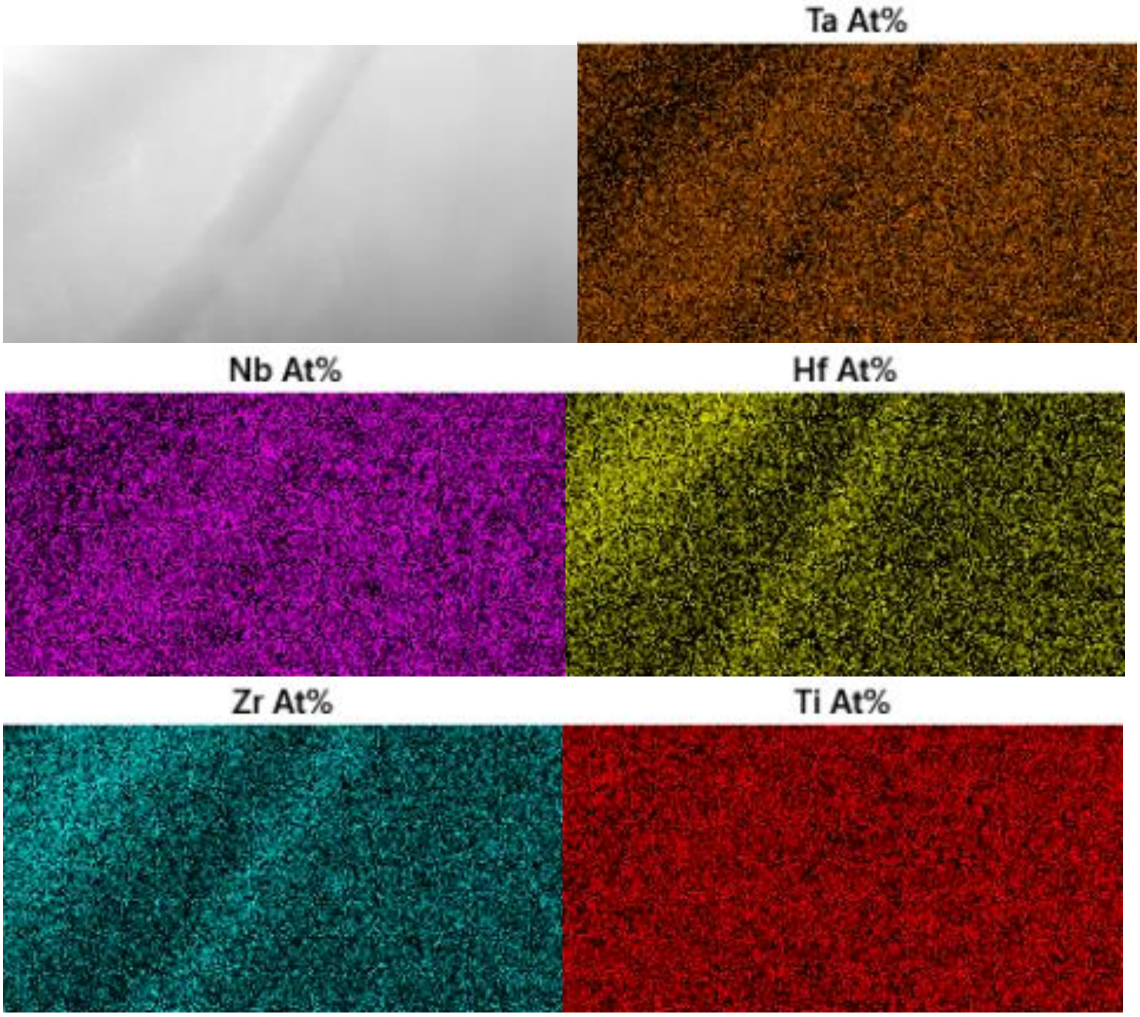

Figure 4.23 - EDX mapping of TaNbHfZrTi after irradiation with 3 MeV Ni, the sample surface is on the left side.

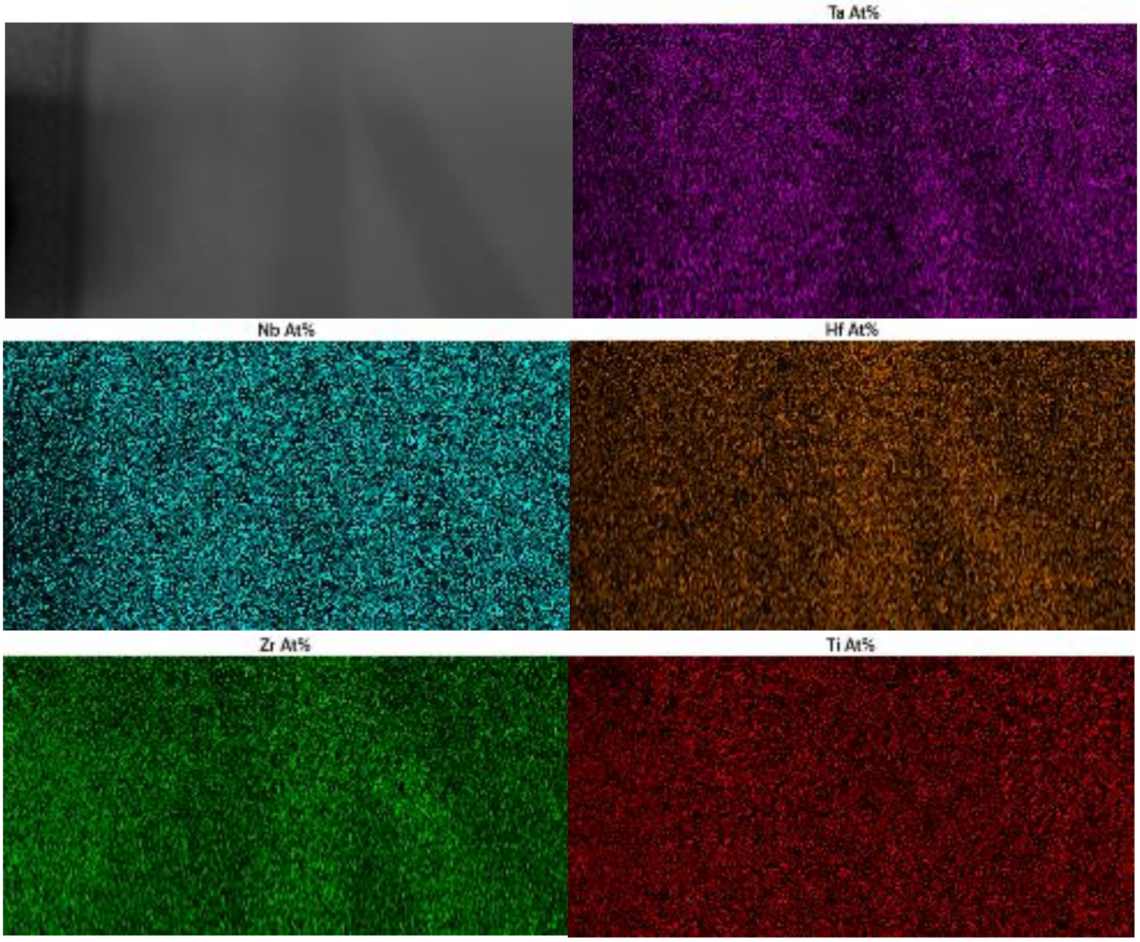

Figure 4.24 - EDX mapping of TaNbHfZrTi after irradiation with He, the sample surface is on the left side

4.4 TEM analysis of AlCoCrFeNi

4.4.1 Pre-Irradiation Analysis

In the original sample of AlCoCrFeNi, near the surface, in Figure 4.25, there was little evidence for the sample being polycrystalline. However, there was evidence to suggest that there may be damage from the diamond polishing prior to analysis. The diffraction pattern shows multiple grains, but it was not possible to get a single zone axis.

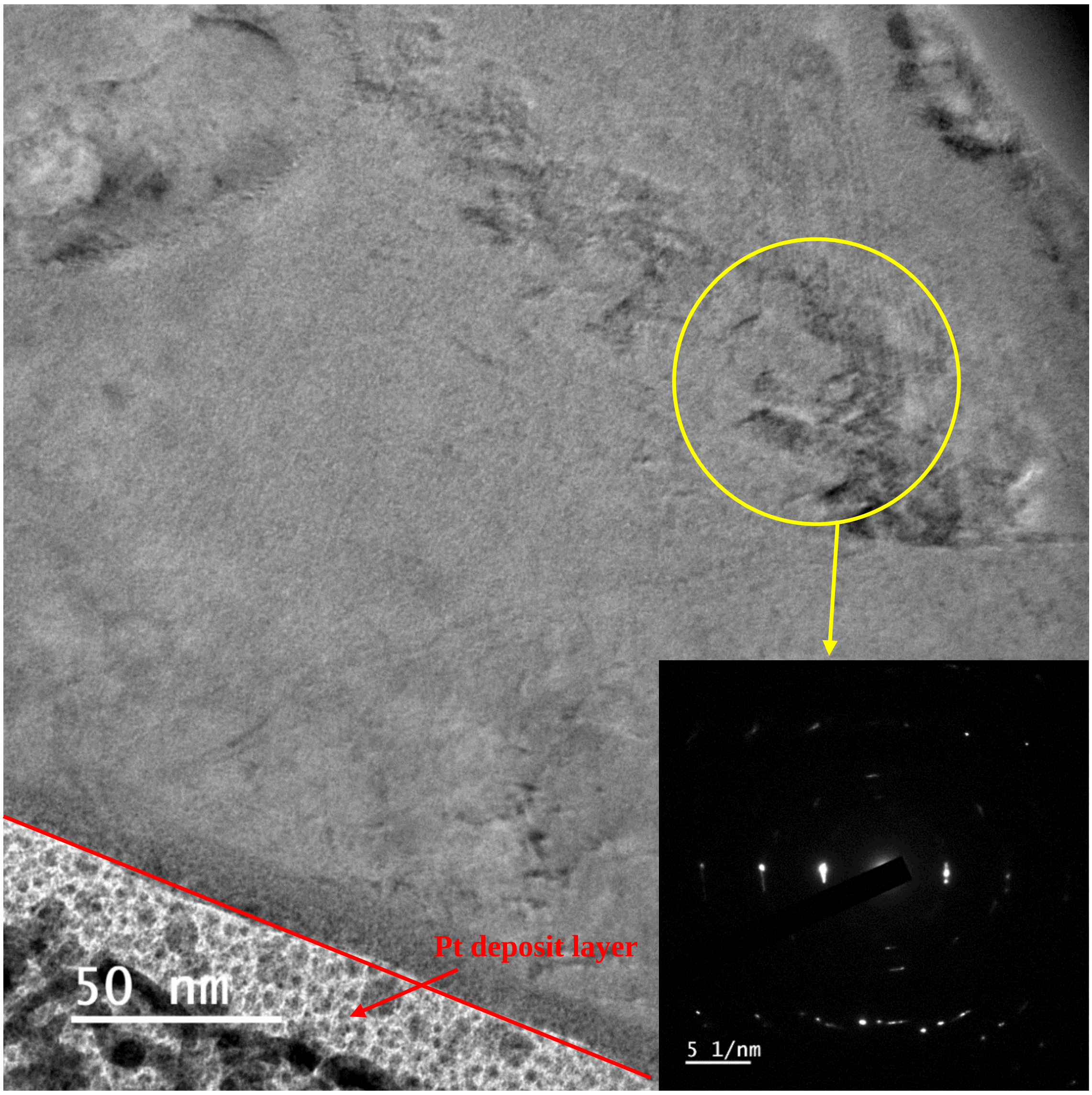

Figure 4.25 - TEM image recorded from AlCoCrFeNi near the surface, the red line is Pt protection layer, and the yellow circle indicates where the electron diffraction pattern was obtained.

4.4.2 3 MeV Ni ion implantation with 5 x 10^{15} ions cm^{-2}

After irradiation, the TEM image, in Figure 4.26, shows crystal domains near the surface. The diffraction pattern recorded from this sample was inconclusive, as it showed that damage has occurred, with only a pair of spots visible within a faint ring, indicating that significant damage has occurred.

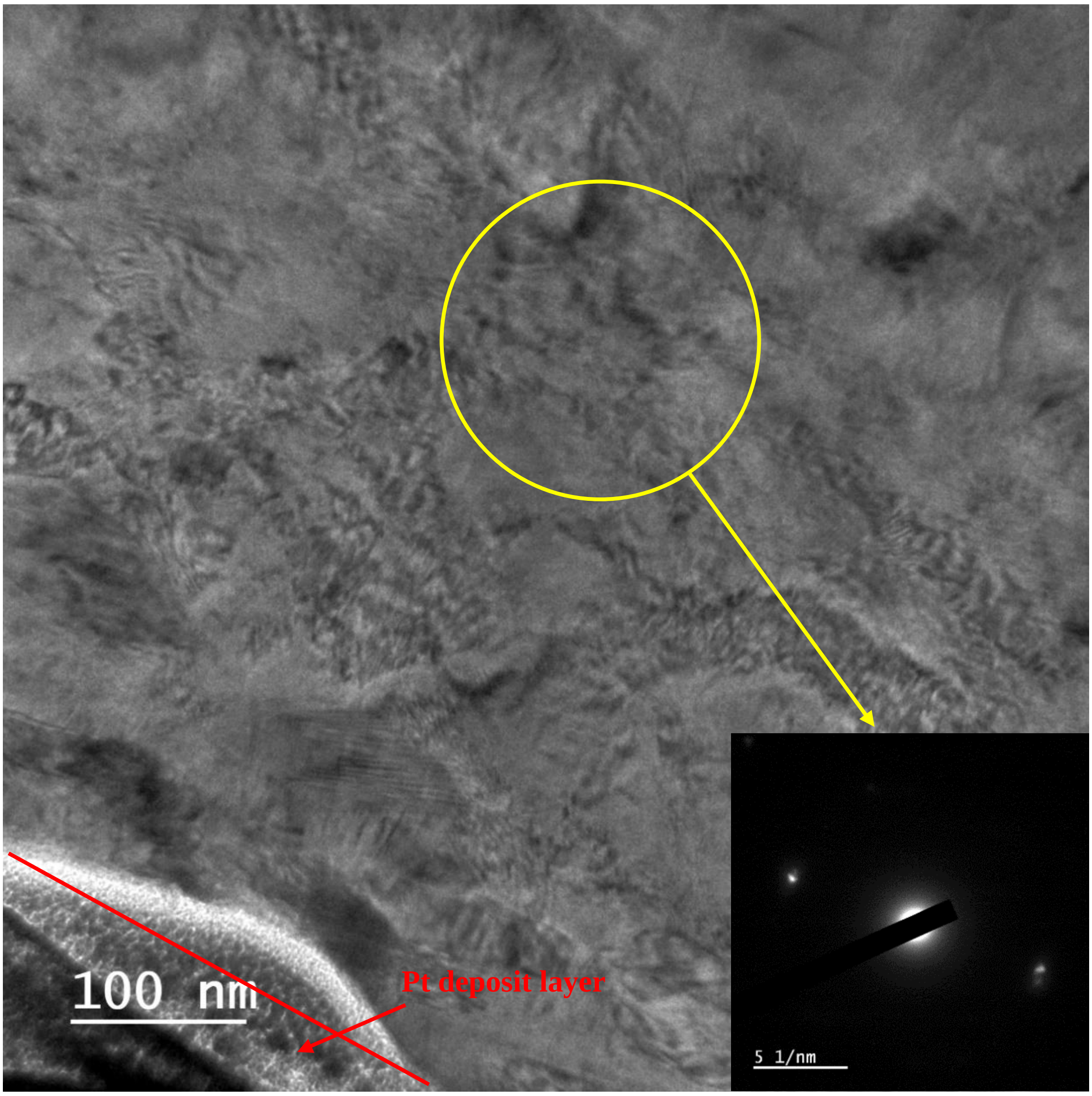

Figure 4.26 - TEM image from near the surface of Ni irradiated AlCoCrFeNi, the red line is Pt protection layer.

With modification of both brightness and focus, in Figurer 4.27, large rings of ~ 100nm diameter can be seen within the sample. These rings, or "bubbles", are enriched in Fe and Cr and have a clear boundary visible within the matrix. It was not possible to find any evidence that indicates that this local matter has interacted with heavy ion impact, and surprisingly the diffraction pattern remained the same. This observation is matching that found from S.Xia's research.[65]

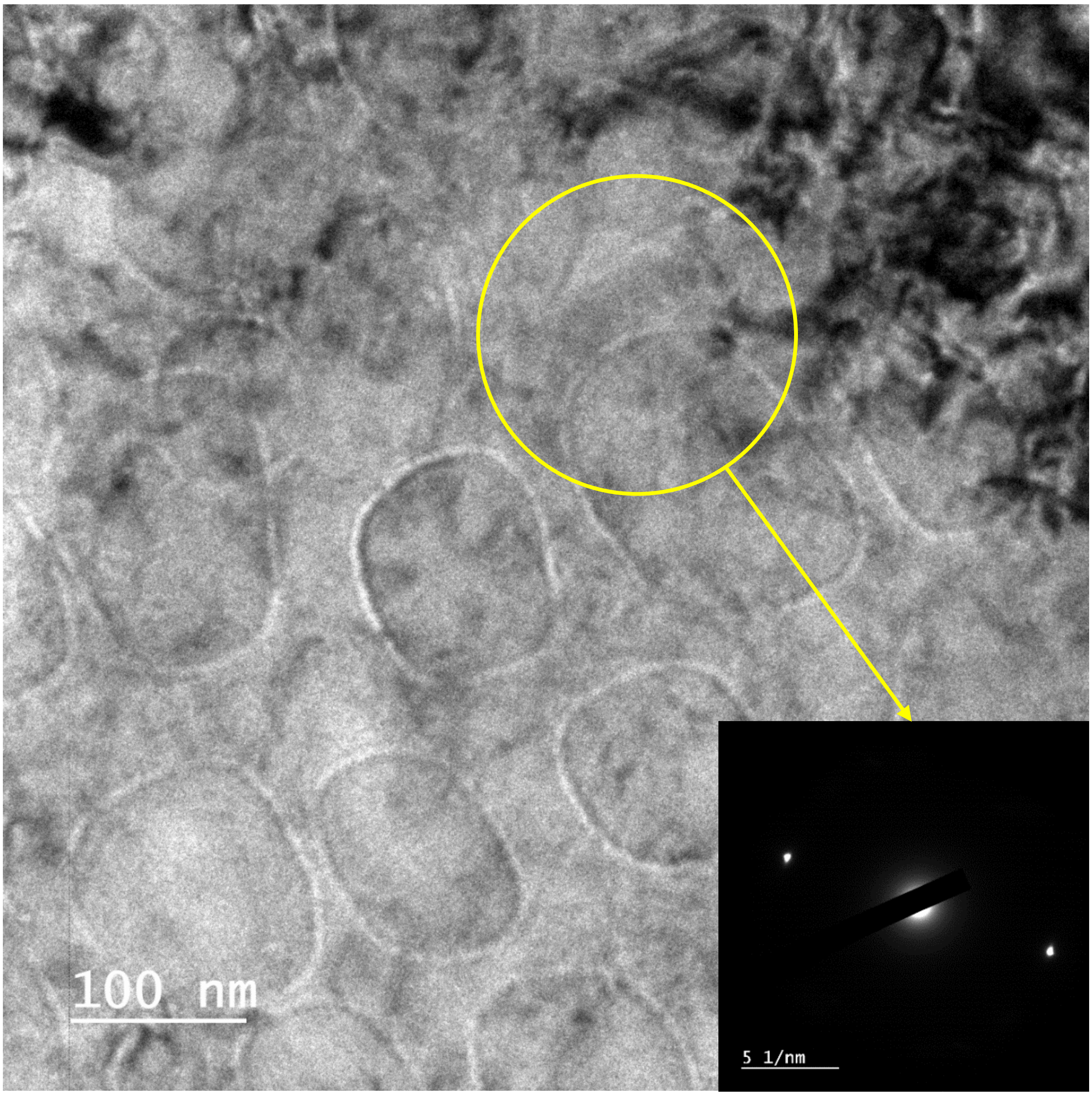

Figure 4.27 – Modified imaging conditions from, highlighting the round shaped grains formed within the sample.

4.4.3 He overlap irradiation

Examination of the helium irradiated sample, in Figure 4.28, showed there was evidence for damage near the surface, with what seems to be a band of bubbles formed just beneath the surface. Bubbles can also be found deeper. However, the distribution is not uniform along the depth, instead they tend to be accumulated where helium has been implanted. Examination of the diffraction pattern suggests there is no significant difference between the crystal structures, with multiple diffraction pattern visible, with sharp spots, and little evidence for a diffuse nature.

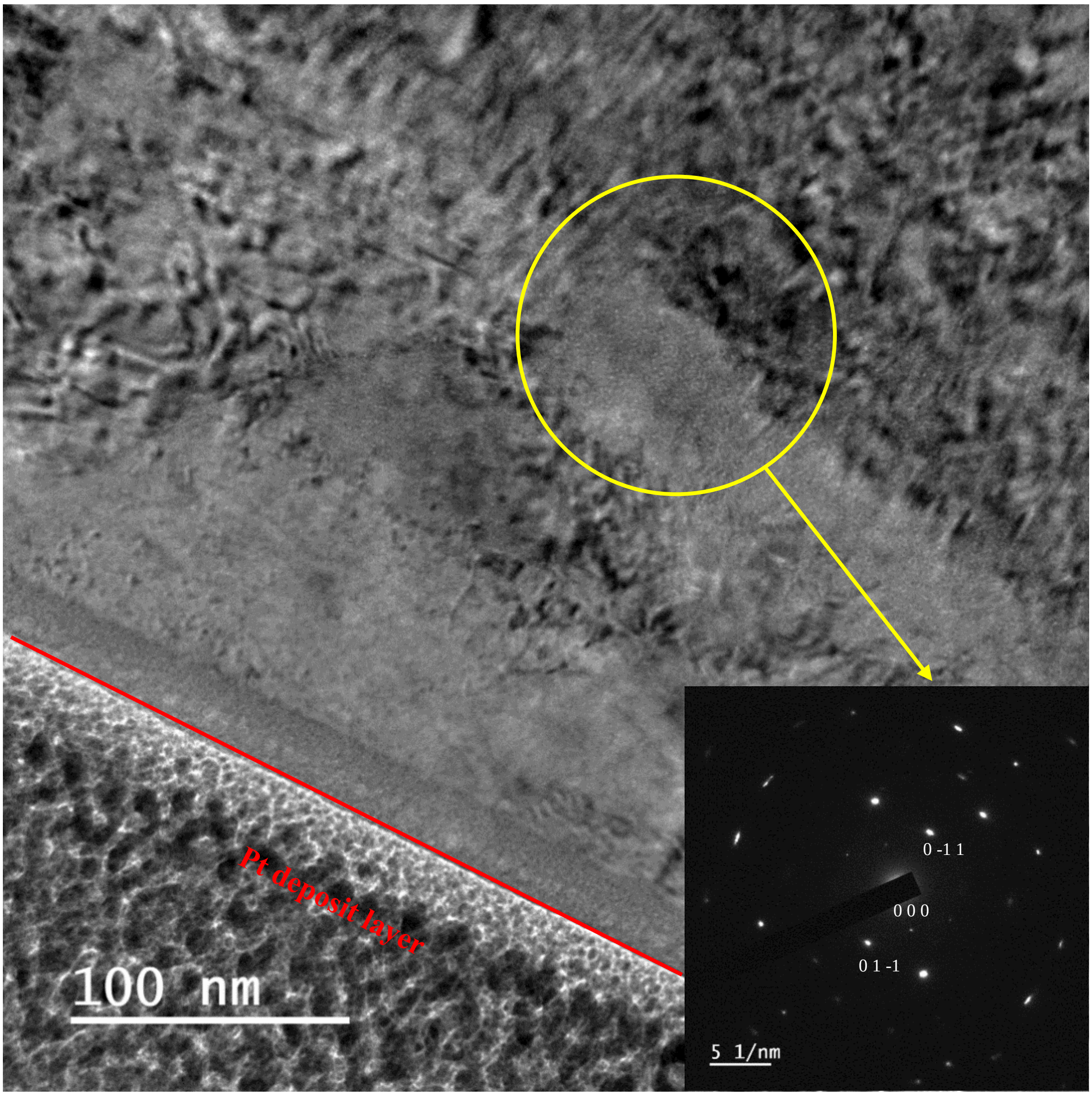

Figure 4.28 - TEM image recorded near the surface for He irradiated AlCoCrFeNi, the red line is Pt protection layer, and the yellow circle indicates where the electron diffraction pattern was obtained.

4.4.4 Energy dispersive X-ray Analysis

This sample in contrast to the others shows regions rich in Fe, Cr with Co, and those rich in Al and Ni with Co, As showing in Figure 4.29. Different from TaNbHfZrTi, this phenomenon does not seem to arise from insufficient mixing, rather from a rapid precipitation of Al during the cooling from the melt. [77] After irradiation, in Figure 4.30, and with this case alone, the unique feature of the grains can act as a reference for shifts in elemental distribution. However, there was no visible change of it after 5 × 10^{15} ions cm^{-2} 3 MeV Ni irradiation, with the boundaries remaining clear. After He irradiation, in Figure 4.31, similar to the Ni ion irradiation, the He irradiation also did not leave any traceable change in element distribution. the Fe-Cr-Co grain has kept same shape and boundary.

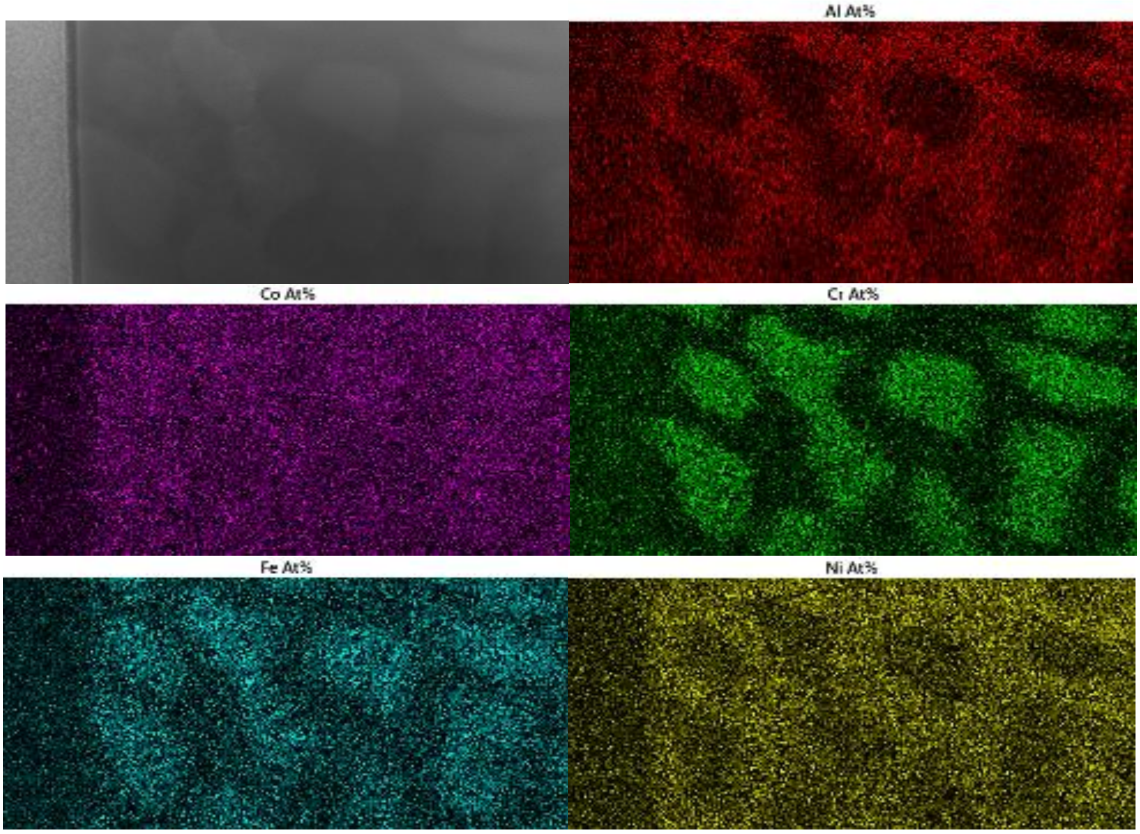

Figure 4.29 – EDX mapping of AlCoCrFeNi prior to irradiation, the sample surface is on the left side

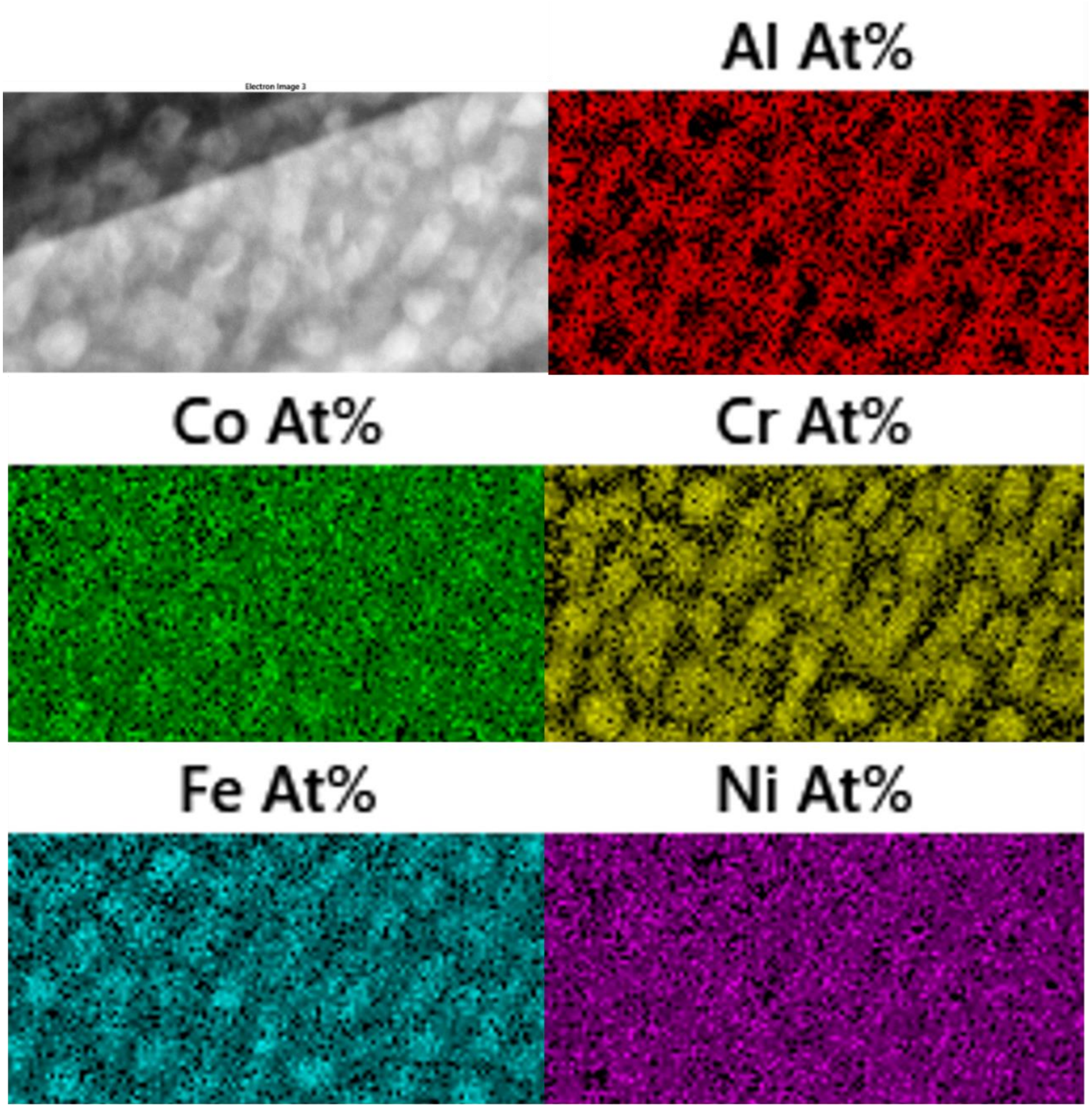

Figure 4.30 - EDX mapping of AlCoCrFeNi after irradiation with 3 MeV Ni, the sample surface is on the left side

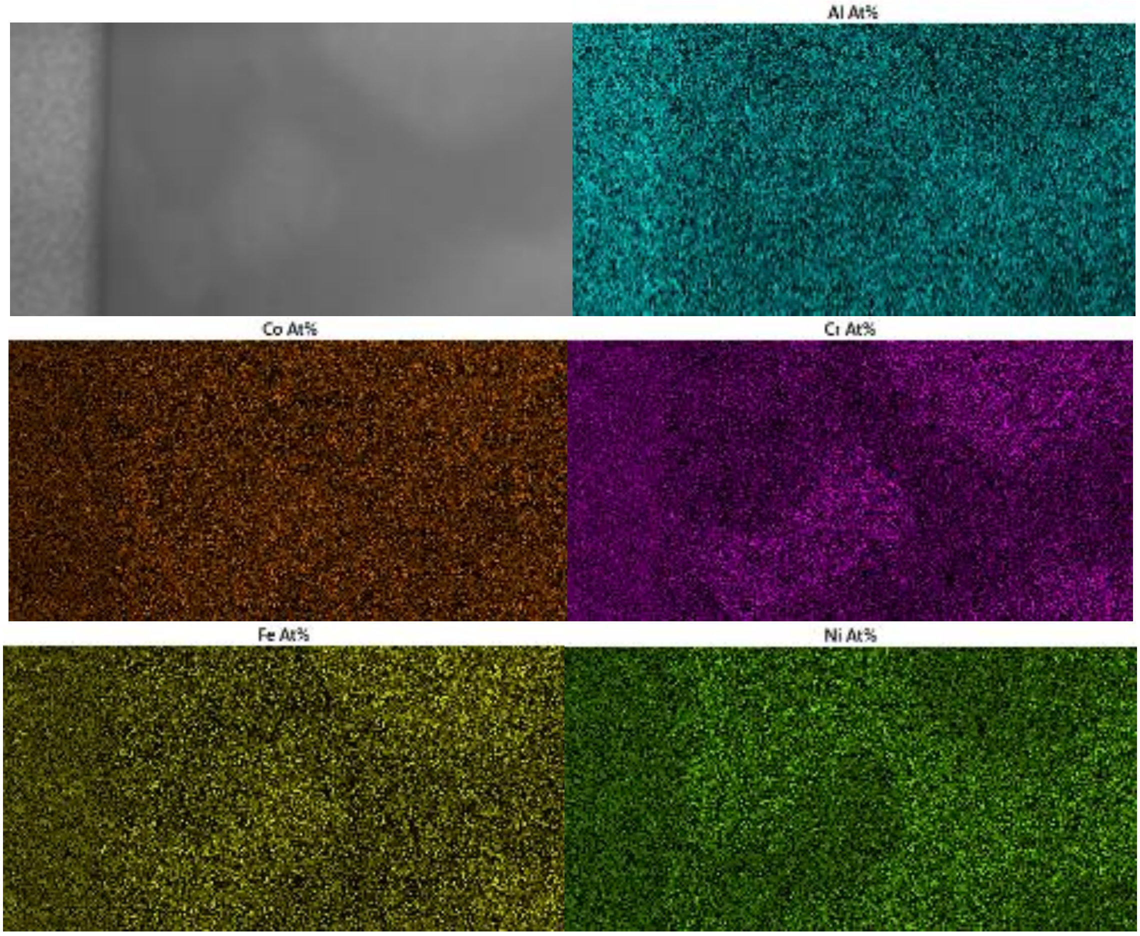

Figure 4.31 - EDX mapping of AlCoCrFeNi after irradiation with He, the sample surface is on the left side

Chapter 5 - Discussion

In this project, the main focus was to examine the irradiation resistance of a range of high entropy alloys, with potential applications within a reactor core. The research was stimulated by the increased proposed use of HEAs in nuclear reactor technology, both fission and fusion. For HEAs in nuclear reactors to work, and hopefully gain higher performance, it is essential to review the potential of HEAs with more detailed information about the response of this material to high energy particle irradiation.

Conventional alloys face significant challenges from their interactions with high energy particles, such as neutrons arising from the fission process, which can modify the microstructure from local interactions with the translating particles. These interactions can in turn lead to crack formation, changes in creep behaviour and hardness etc. High entropy alloys may be able to maintain their microstructure under high levels of irradiation due to their different atomic arrangement.

With conventional alloys, damage can be considered similar to an ordered system shifting to a disordered system. In this process, increasing irradiation damage increases entropy in the system, therefore, a high entropy alloy which already has a high level of entropy could in theory resist further gains in entropy. In a high entropy alloy, different elements occupy the same crystallographic site randomly, which means for a high entropy alloy, an atom displacement should not impact the crystal structure as significantly as in the conventional alloy. The displaced atom could then fit into the new location and maintain the highly mixed state. Additionally, the sluggish nature of diffusion will restrict any induced dislocation movement from the damage process. With this maintained microstructure, the mechanical properties of high entropy alloy could be preserved under high levels of heavy ion irradiation. Helium has a different nature, with a different mechanism for damage and impact on the target material. Helium is both a fission and decay product, with a lower atomic mass compared to other fission products. Therefore, it has less interaction with local atoms during its movement, and traverses deeper into the target material. Other than the normal irradiation damage mechanism, the helium ion can form helium gas bubbles and precipitate out in the lattice. This formation can induce significant change in a material, but due to the slow movement of atoms within a high entropy alloy, this precipitation of helium gas can be significantly reduced. As a result, high entropy alloy can gain special performance in resisting both heavy and light ion irradiation due to it special orientation of composite element.

To identify this potential irradiation resistance of high entropy alloy, a series of experiments have been performed on the high entropy alloy sample, with high energy ion particles. The experiment design was divided into two sides, examining the change in microstructure and hardness. Through the comparison of data collected before and after the irradiation, it allows for the analysis of the degree of damage and impact on the performance to be identified. The selected target high entropy alloy samples are $Co_{1.5}CrFeNi_{1.5}Ti_{0.5}Mo_{0.1}$, $AlCoCrFeNiSi_{0.1}$, TaNbHfZrTi and CoCrCuFeNi. These high entropy alloy samples have previously been studied in early research focusing on their corrosion resistance and helium ion implantation. These high entropy alloys represent both mainstream and high melting point high entropy alloys. As such this project can provide a view of the irradiation damage resistance and its impact within high entropy alloys.

During the synthesis process, all the samples were successful produced by a vacuum assisted arc-furnace. Due to the limitation of the furnace on ingredient physical form, the silicon in $AlCoCrFeNiSi_{0.1}$ was not added, however this has a minimal impact on the degree of entropy in this sample. From observation by EDX, there is some segregation present in some samples, as the arc-furnace did not, at least in these samples, provide sufficient mixing for an even distribution of elements in the final product. However not all the uneven distribution is led by the insufficient mixing, AlCoCrFeNi is one sample that naturally formed enriched grains during synthesis [78][74]. Different from the element rich grain found in other high entropy alloy, the grains within AlCoCrFeNi are generally spherical in nature and separated uniformly across the sample, helping to identify that formation occurs during solidification. Post formation preparation of the direct cast ingot high entropy alloys was problematic, as the diamond wafering saw, could not be clamped easily. Therefore, electrical discharge machining is more preferred method of section the sample.

To summarise the observation and comparison of the TEM and EDX analysis, they have identified that for the selected high entropy alloy samples, they will receive atomic level damage from both heavy and light ion irradiation, with the level of damage dependent on the differing levels of atomic displacement. However, all the selected high entropy alloys maintained their microstructure and element distribution to at least 5×10^{15} ions cm^{-2} of fluence, approximating to between ~140-240 dpa. At very shallow depths and where the inserting ion accumulates, some shift in microstructure has been observed. All the samples show the crystalline state being almost identical to the undamaged state. Even with the insufficient mixing during the synthesis process, those samples are still retaining their high entropy state. As shown in the electron diffraction image from the high dose Ni irradiated $Co_{1.5}CrFeNi_{1.5}Ti_{0.5}Mo_{0.1}$ sample, Figure 4.5, there is a significant ring pattern in the near surface area which indicates the formation of a damaged microstructure. Similar phenomenon has been found in all samples with high dose Ni irradiation. The degree of the irradiation damage received in each high entropy alloy is different. For CoCrCuFeNi, Figure 4.11 and 4.12, and TaNbHfZrTi, Figure 4.19, the microstructure at the surface area has moved from being large single crystals to a more multi crystal structure. For AlCoCrFeNi, Figure 4.27 it loses some of the sign and character of tiny crystal after been irradiated.

For helium irradiated samples, it is showing that helium seems to precipitate out of the target material during the irradiation process and form tiny holes/bubbles in the irradiation effect zone. Very dense light spots can be seen in TEM images of the irradiation affected zone, e.g., Figure 4.28. Initially those light spots had been treated as a ‘bubble’ created by the helium gas precipitation, but with detailed analysis using through-focused bright field imaging method this is not actually a helium ‘bubble’, however this phenomenon is found in all the helium irradiated high entropy alloy sample, so is seemingly linked to insertion of helium ions. The current hypothesis is that the formation of light spot is an initial state of a helium ‘bubble’. In this project, the ion irradiation is carried out at room temperature. Under this condition, the diffusion of helium atom has been restricted by the nature of high entropy alloy which is also knows as sluggish diffusion. This significantly reduce the rate of the formation of helium ‘bubble’ under such high dose of helium ion insertion and present as the initial stage of helium precipitation. Due to a limitation in the EDX technique, the helium component ratio inside a post helium irradiated sample is not detectable. Given the nature of the samples and method of preparation for analysis, it is likely any He present in the sample will have been lost by the time of analysis. However, EDX is still capable of confirming that all high entropy samples do not have noticeable element distribution shift after been irradiated with heavy and light ion. It provides the evidence that under these experimental conditions the high entropy alloy samples have kept the element distribution and hold the alloy characteristics and show no evidence for ‘de-alloying’. This is critical to a high entropy alloy as almost all the special properties within a high entropy alloy are related to the random orientation of element. Therefore, it suggests that high entropy alloys could maintain their general properties after been irradiated with high dose of ion particle.

The nano-intender gives detail about the post irradiation mechanical properties within high entropy alloy. The surface hardness is significantly affected by the ion irradiation. However, the hardness shift is not linearly proportional to the atomic damage level, especially with low dose of Nickel ion and helium ion irradiation. The pattern of this hardness shift seems to depend on the crystal structure of each high entropy alloy. The hardness of $Co_{1.5}CrFeNi_{1.5}Ti_{0.5}Mo_{0.1}$ and CoCrCuFeNi is reduced with increasing irradiation damage level, Figure 3.7 and 3.8. Whilst the hardness of TaNbHfZrTi and AlCoCrFeNi are increasing with low level ion irradiation, Figure 3.9 and 3.10. $Co_{1.5}CrFeNi_{1.5}Ti_{0.5}Mo_{0.1}$ and CoCrCuFeNi both adopt an FCC crystal structure whilst TaNbHfZrTi and AlCoCrFeNi adopt a BCC crystal structure.

The hardness drops within $Co_{1.5}CrFeNi_{1.5}Ti_{0.5}Mo_{0.1}$ and CoCrCuFeNi are directly linked with the level of irradiation damage received, resulting from the local atom displacement when it interacts with traversing particles. The more the structural atom moves, the higher the alteration in the microstructure, which significantly reduces the mechanical properties of the alloy material. On the other hand, the hardness rising in TaNbHfZrTi and AlCoCrFeNi with low dose of irradiation is more complicated. There are several possible explanations for this phenomenon. The first is that the low amount of irradiation damage is altering the surface microstructure to cause partial elemental precipitation out of the lattice to form a more brittle and harder layer of material. The second one is that high speed ion transfers a lot of heat to the sample surface and causes a temperature rise during the irradiation process. This extra heat process provides the situation where the sample can form more a rigid phase when it cools down. In addition, the inserted ion will slightly modify the composition of element in the area. All those hypothesises are based on that all high entropy alloys with BCC crystal structure have this hardness drop with low dose of ion irradiation. In the EDX mapping image, the altering of the element distribution cannot be directly found. It could be the actual hardening layer thickness is very small which cannot be clearly analysed by the EDX or the altered element distribution is very similar to the original sample material.

With more detailed observations on the hardness test for each sample, it can be seen that there is an increasing trend in hardness from a depth of 30nm to 60 nm in the majority of irradiated high entropy alloy samples. This could be evidence for the existence of melting and solidification occurring in the surface area. The extreme temperature is located on the very shallow surface due to the heat quickly distributed into rest of the sample and the loading platform of the irradiation experiment. All hardness tests of AlCoCrFeNi, regardless pre or post irradiation, have significant hardness drop with depth increase. The phenomenon is constant in each sample which suggests there is possible oxidation layer formation in the particular high entropy alloy material. Aluminium is known to be a very reactive metal which will form a very dense oxidation layer on the sample surface. This oxidation layer will have much higher hardness compared to the matrix material. What can be concluded from examination of the nano-intender data, is that the mechanical properties of high entropy alloy are clearly reduced by a significant dose of heavy ion irradiation. The trend of this hardness shift shows that with higher levels of damage the hardness will keep dropping until the material reaches the failing point when it has lost its original properties. On the other hand, for low level irradiation damage the hardness shift in a high entropy alloy seems related to the crystal structure with BCC high entropy alloys showing increased hardness, whilst FCC high entropy alloys show decreased hardness. Although the surface hardness will be affected by many factors such as material mechanical properties and the oxidation layer formation, the nano-intender is still able to give the comparable data of the mechanical properties on test sample.

To justify the consistency of test results from each sample, due to the purpose of ensuring the test result and avoid compressing the sample surface, the controlled test data is not acquired from the back side of the test sample. Therefore, the consistence of the result needs to be accessed in the different way. From the EDX mapping, each sample has a similar element distribution across the same alloy. This suggests that each sample shares a similar microstructure within each alloy batch. In addition, before each dynamic mechanical analysis (DMA) three simple hardness tests had been performed on the relative position of ion implanted area to obtain data on hardness. This test uses conventional methods with denting probe and microscope to analysis the dent mark left on the sample surface. Compared to DMA, this method is much faster and cost less, but the observation depth cannot be controlled. Through the analysis of the hardness test across all the samples, as Figure 5.1 shows, the change in hardness with different ion implantation does agrees with the trend of hardness data obtained from the DMA. It indicates that the test area is located in the ion implanted area. In the simple hardness test that probe will easy punch though the irradiation affects zone and the tip will stop at uncertain depth so it will not reflect the actual hardness of this thin layer of irradiated sample. but it will help verifying the consistence of the test result.

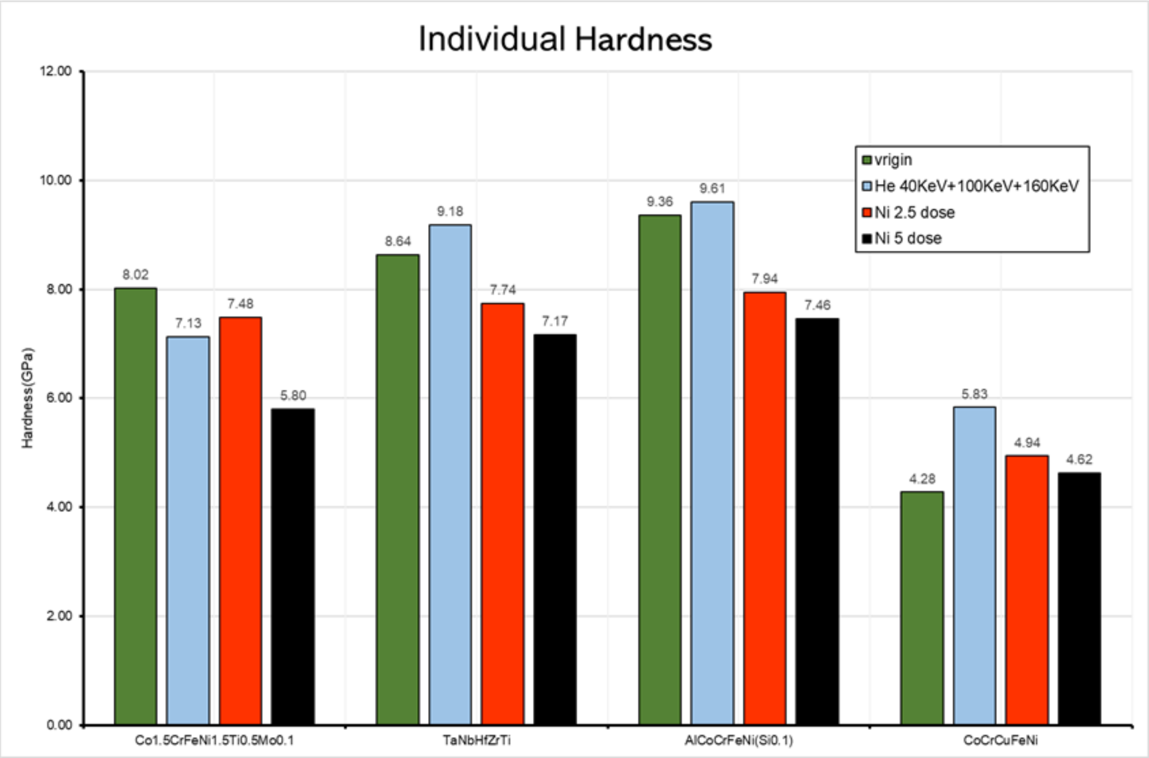

Figure 5.1 - The individual micro hardness test on each sample. Each test performed three times and take the average.

To perform consistent and comparable data, all material samples followed the same method for experimentation, with differences being minimised. However, the precision of the final result cannot not be quantified directly, as some of the information obtained can be affected by the proficiency of the operator. For example, TEM specimen preparation from the sample using FIB is highly dependent on the experience and skill of the pilot. The TEM specimens made in this project have been checked with SEM to ensure the thickness is below 100 nm, but due to the interference from magnetic elements within the samples, it is very difficult to keep the thickness exactly the same in each sample. The TEM imaging will also have the same limitation of the operator. In addition, the alignment of crystal structure in certain samples was limited by a single tilt platform, as a double tilt holder was not available. Although each TEM image followed the approach of finding the best alignment of the crystal, it was not the perfect TEM image to show all the detail within the high entropy alloy. Linked with this again as the use of magnetic elements, as with SEM, induced some interference in the observed images. As mentioned earlier the ideal data range of nanoindentation is relatively short, which leads to the observation of surface mechanical properties limited in depth to between 30nm-150nm. In addition, the mounting of the sample within the nano-intender is a key factor, and if not done correctly can result in a failed test, which has to be repeated.

As a conclusion this series of experiments and tests gives a general idea that high entropy alloy could have a higher relative level of irradiation damage compared to the conventional alloy such as stainless steel 316, before significant change in properties. Not only is the original hardness higher than stainless steel 316, but also the post irradiation sample hardness is maintained.[79] The potential resistance of helium bubble formation in high entropy alloy has also been noticed during helium ion irradiation. This is important to potential nuclear industry application of high entropy alloy, as in the real scenario of nuclear reactor, for example as cladding or as containment within a molten salt reactor core, the majority of irradiation damage received will be from the fission reactions, and alpha decay in the fuel. Compared to those two damage sources, other heavier fission products have less impact on the material properties, because the heavy particles have significant less penetration depth on the material and the mechanism of the damage is focused on the interaction of the original local microstructure. Helium will precipitate out when above a certain level and create bubbles that weaken the bulk material at a more macro level. The potential helium bubble resistance could provide long service life for these materials within a nuclear reactor. The restriction in the formation of helium bubble will directly delay this process and help reduce the formation of cracks, arising from the increased stress/strain around a bubble.

Other tests show valuable information in the understanding of high entropy alloy properties. The magnetic hysteresis test gives an indication of the magnetic performance for these materials. Even with all three magnetic elements in the high entropy alloy, the magnetic remanence within $Co_{1.5}CrFeNi_{1.5}Ti_{0.5}Mo_{0.1}$, AlCoCrFeNi and CoCrCuFeNi, Figure 3.11 is indicative of them being classed as soft magnetic materials. TaNbHfZrTi does not have any magnetic elements, so the magnetic properties are very close to air, with little remanence or saturation, Figure 3.12. AlCoCrFeNi has the highest magnetic saturation value in all four materials tested in this project, with the level being significant that magnetisation of this material, could become problematic. This will affect not only the application performance but also experimental analysis, as for example the magnetic properties will interact with the magnetic field within a TEM, impacting image quality. Overall, the magnetic properties of high entropy alloy are largely dependent on its composition, as $Co_{1.5}CrFeNi_{1.5}Ti_{0.5}Mo_{0.1}$, AlCoCrFeNi and CoCrCuFeNi all contain magnetic elements, but each high entropy alloy has differing magnetic behaviour. The addition of copper and titanium seems able to restrict the establishment of magnetic field. The addition of copper, a known diamagnetic material, may help CoCrCuFeNi reach a higher level of magnetisation and magnetic saturation. On the other hand, titanium as a non-magnetic element largely reduces the magnetic properties within $Co_{1.5}CrFeNi_{1.5}Ti_{0.5}Mo_{0.1}$. Aluminium seemingly enhances the magnetic properties of AlCoCrFeNi when compared to the other two cobalt, iron and nickel family high entropy alloys. The mechanism behind this magnetic property difference between each different high entropy alloy is not completely clear, as whilst the elemental nature has a significant effect on the magnetic property, the crystal structure will also play an important role in this gain of magnetic property.

Experimental uncertainty exists at every step of measurement, such as weighing the material, EDX mapping, hardness measurement or even the ion implanted in the sample. During the weighing, the material is sectioned into correct amount, so all the mass is measured to ± 0.01g each time. this will certainly affect the formation of high entropy state within the final alloy, but the entropy state formation does not have barrier limitation of the number equilibrium on atom account and the finally alloy still formed certain level of high entropy state. The ion implantation is performed by a large accelerator. The ions implanted on sample is counted by measurement on the current flow into sample, with the shutting of the beam having a short delay before being completely stopped. This short delay will cause around 0.002% overflow of total ion flow. Compared to the amount of ion implanted into sample, such amount of overflow should be insufficient to induce a difference on the irradiation damage of the tested sample. This type of uncertainty has very small effect on verification of mechanical property change with different grade of ion implantation. EDX mapping is using the X-ray characteristics of the atoms to analyse element distribution in a range of sample. The uncertainty of the EDX mapping is around ±5% of the element composition, and is linked with the performance of the X-ray detector. The higher performance detectors have uncertainty around ±2% of the element composition. In order to reduce the potential effect on verification of the experiment result, multiple EDX mapping have been down to ensure the even distribution of element and to check the possible clots of raw material which will reduce certain element distribution in the alloy. For the hardness performed by nano intender, the uncertainty is mainly because of the intending force control. As a result, the hardness measured by the equipment have ±0.005 GPa uncertainty within the result. In this project, the uncertainty comes from various process, the result might not be able to support accurate quantitative conclusion but the comparation between the degree of irradiation damage with various ion implantation grade is achievable.

Through the analysis of the information obtained from experiments, the main goal of the project is partially achieved, i.e., the impacts arising within an HEA from radiation damage. Although the high entropy alloy has maintained better performance than stainless steel 316, the effect of the irradiation damage on the microstructure and mechanical performance is still difficult to quantify. Future research should focus on experimental design that can quantify this effect in a high entropy alloys performance. One key area of work that should be undertaken is to examine these systems under the more damaging gold irradiation that was planned, but which had to be curtailed when the Covid pandemic started, and the ability to work in labs/facilities was restricted. This was work was planned to be undertaken during the lab/university shutdown but could not be completed. The results from such work would greatly aid the understanding of damage build-up, and its impact on properties

Chapter 6 - Conclusion

In this project, $Co_{1.5}CrFeNi_{1.5}Ti_{0.5}Mo_{0.1}$, CoCrCuFeNi, TaNbHfZrTi and $AlCoCrFeNiSi_{0.1}$ were selected as the research focus, and were chosen based on existing research. SRIM simulations were applied to produce estimations on the range and levels of damage for gold, nickel, and helium. The estimated depth for peak damage inside the samples were 300 nm for 4.5 MeV gold, 1000 nm for 3 MeV nickel and 7000 nm for 4 MeV helium. Although the total expected damage levels were different, they remain comparable and representative of the expected ranges of damage within a reactor. There was one problem with the helium ion, that under these conditions it would stop in a very narrow range inside the sample material due to the light mass and high energy. To compensate for this and create a wider observation window for the experiment, the helium implantation was separated into three lower energy implantations, giving rise to a range of ~ 600nm, and a damage range of ~100 to 400 nm.

All samples are fully melted thoroughly twice within the furnace to ensure all the material were combined evenly. There was visible evidence for oxidation appearing on the surface of the as cast ingot, however, it remained on the surface without have any deeper impact on the material inside the sample ingot. The crucible within the vacuum arc furnace was cooled by recirculated water, so the ingot was cooled rapidly. This gave the sample a very short normalization period and left the potential for the formation of small grains.

All samples were cut and polished into mirror finish. The diamond suspension used in the polishing stage had an unexpected effect on the surface microstructure. On the TEM image, all the as-cast sample showed a dark band appeared in the depth around 20nm to 40nm. This phenomenon could be caused by the mechanical pressure on the test surface, from the polishing.

After the high entropy alloy had been irradiated by Ni and He ions, a serious of experiments were undertaken to examine the irradiation impact on the microstructure. Due to various reasons, arising from the COVID-19 lockdown and restricted working, the gold ion irradiation, and subsequent analysis could not be performed.

The nano-intender was used to analyse the mechanical properties on a shallow area on the sample surface. From comparison of the results each sample reacts differently with different fluences of ion irradiation, normally a higher dose reduces hardness in the irradiation affected area. However, the 5 x 10^{15} ions cm^{-2} Ni ion irradiated samples showed the lowest hardness. Lower fluences of Ni ion irradiated and He ion irradiated samples did not always reduce the hardness, but rather enhanced the hardness in some samples. There were two different behaviours between the group of $Co_{1.5}CrFeNi_{1.5}Ti_{0.5}Mo_{0.1}$, and CoCrCuFeNi and the group of TaNbHfZrTi and AlCoCrFeNi. For $Co_{1.5}CrFeNi_{1.5}Ti_{0.5}Mo_{0.1}$ and CoCrCuFeNi, the hardness decreased with increasing accumulated damage. On the other hand, TaNbHfZrTi, and AlCoCrFeNi increased hardness with low levels of damage. TaNbHfZrTi had a higher hardness with 2.5 x 10^{15} ions cm^{-2} of helium, but in AlCoCrFeNi there was a reversed tendency with helium irradiation leading to a higher hardness. The postulated reason for this observation, is that the low levels of damage interacted with material surface and blocked dislocation planes, thus generating a higher hardness than the original sample.

The trend of hardness shift in each sample was also different. $Co_{1.5}CrFeNi_{1.5}Ti_{0.5}Mo_{0.1}$, CoCrCuFeNi and TaNbHfZrTi relatively maintained their hardness within the testing range. On the other side, AlCoCrFeNi showed a significant drop in all samples with differing levels of accumulated damage. There are two possible reasons for this difference. Due to the presence of aluminium within AlCoCrFeNi, there is the possibility that this gives a lower meting point which allows the sample surface to slightly melt during high energy irradiation. This re-melting process allows the material to rearrange and obtain increased hardness in the surface area. The second potential reason is that aluminium forms a rigid and dense oxidised layer on the surface, leading to a much higher hardness in the shallow part of sample. Overall, the group of $Co_{1.5}CrFeNi_{1.5}Ti_{0.5}Mo_{0.1}$, CoCrCuFeNi theoretically have a similar face centre cubic single crystal structure and whilst TaNbHfZrTi, AlCoCrFeNi theoretically have same body centre cubic single crystal structure, which can explain their broad similar behaviour.

From TEM analysis, all samples show a similar trend on microstructural shift with the various levels of accumulated irradiation damage. However, the actual response of each high entropy sample is different from each other. The as-cast sample of $Co_{1.5}CrFeNi_{1.5}Ti_{0.5}Mo_{0.1}$, CoCrCuFeNi, TaNbHfZrTi showed a dark feature under surface at a depth ~30–100 nm. This phenomenon disappeared after been irradiated. Higher magnified images can review the small grains formed inside the sample matrix. When it comes to diffraction images, different grains have the same crystal structure as the matrix.

After been irradiated with 5 x 10^{15} ions cm^{-2} Ni, these samples show a visible shift in the observed microstructure visible by TEM. This microstructural shift can be divided into two categories. The first being that the crystal structure becomes more unified in nature, when compared with the as-cast sample. From the analysis of $Co_{1.5}CrFeNi_{1.5}Ti_{0.5}Mo_{0.1}$ and AlCoCrFeNi, the diffraction images show a more regular diffraction pattern compared to the as-cast sample. With enhanced image analysis, a diffuse ring can be spotted around central spot, which suggest evidence for the formation of an amorphous phase, or at the very least a damaged region. The second one is that the samples have alternative grain formation after been irradiated with 5 x 10^{15} ions cm^{-2} of Ni. The TEM image of CoCrCuFeNi and TaNbHfZrTi, formed visible grains across the sample in the irradiated effected zone. It is hard to determine the actual crystal structure of those new grown grain, they normally have a size ~ 50 x 50 nm. On the diffraction image, those two samples showing the significant diffusion around the central spot. This phenomenon indicates that the crystals within an as-casted sample have been damaged by the Ni ion. He ion irradiation generally has a small effect on all high entropy alloy samples. There is no obvious formation of damaged grains, even in the diffraction image, the crystals showed similar images to the as-casted sample. With higher magnification, the round shape of a shadow formed within the irradiation effect zone. However, this was not identified as a helium gas bubble, but more likely to be the initial stage of helium precipitates out of the material.

There were other phenomena spotted during the TEM observation, one being the formation of grains with clear element segregation in the AlCoCrFeNi. These are regular round shape grains speared uniformly inside the sample. This element segregation appeared across the entire sample, indicating that this does not arise from the irradiation damage but formed during the casting process. The second observation is the actual irradiation damage accumulation range being deeper than the SRIM simulated result. The third observation is a grey band being visible in the AlCoCrFeNi sample, with a width of ~10 nm, which disappeared after been irradiated by Ni, but remained visible after irradiation with He.

EDX analysis was used to visualise the element composition in the observation area, as a map. EDX mapping of the as-fabricated samples indicate that the synthesis of high entropy alloy samples were not always perfectly mixed. In the CoCrCuFeNi EDX mapping, there is a large Cu rich grain visible in the sample, indicating an uneven mix of ingredients during the melting process. This uneven mix can also be found in the TaNbHfZrTi sample. AlCoCrFeNi has a unique feature of elemental segregation forming Cr-Fe rich areas across the entire sample. This Cr-Fe rich formation is derived from the nature of the initial elements and there was no significant visible difference in the elemental map, between pre and post-irradiated samples. Even after the high fluences of Ni irradiation, the shape of Cr-Fe rich grain retained its shape, without any visible diffusion around the grain.

The magnetisation characteristics are linked with the composition. All samples were able to be magnetised under an applied magnetic field, but all of them do not have any magnetic residues when the applied magnetic field been removed. AlCoCrFeNi has the highest magnetisation properties compare to the rest and has the highest magnetic saturation. In the contrast, TaNbHfZrTi has low magnetisation under a strong magnetic field, likely to be from the non-magnetic elements present.

Nano-indention has shown that in FCC samples the hardness decreases with increasing induced damage, but that BCC samples can show an increase. This change implies a link between the structure type and radiation damage, that should be investigated further.

Overall, this work has shown that high entropy alloys have potential within a nuclear reactor, but further work is needed to better understand the impacts of radiation damage, particularly with respect to potential He gas bubble formation. However, the materials prepared for this PhD indicate that when it comes to certain induced changes, a change in structure has more of an effect than a change in composition, for example going from BCC to FCC structure types.

Chapter 7 - Future research

During this project, a majority of the original main goals have been achieved. However, the behaviour of high entropy alloys still needs to be improved to review their potential and capability. In addition, there were several problems during the project that if were rectified for future work would allow for improved results. These can be broken down into two areas, enhanced experimental design, and improved sample fabrication.

During this project, four different high entropy alloys were selected. Three of them contained cobalt, iron and nickel which are the most common materials used high entropy alloys. The remainder was made from a composition of high melting point elements, theoretically forming better high entropy alloys. This combination gives a broad comparison of properties across a range of HEAs. However, all transition metals can be used in HEAs, therefore in the next stage research, different HEAs should be included in the test. Elements of particular interest include zirconium and tungsten, which have either a special neutronic applications, or a high melting point. With different high entropy alloy components in the work, the relationship between the addition element and the desirable property for nuclear applications becomes possible. This is important, as the current understanding of HEAs is still not fully clear, and the "Cocktail effect' within high entropy alloys is restricted to a relatively limited range of mechanical properties, such as hardness. With radiation damage other mechanical properties change, and such links need to be examined. For example, ductility is one of the essential properties, and the loss of elastic properties in the surface layer, may mismatch with deeper matrix material. For example, the surface layer may crack when applied with stress, whereas material at deeper depth may not. This property mismatch can affect the behaviour of material under high irradiation working conditions. Most mechanical properties can be test with nano-indentation, with testing of corrosion resistance of pre- and post-irradiation high entropy alloy also undertaken. Theoretically the chemical properties are related to the elemental composition, but practically the corrosion resistance is highly related to the speed of protective oxidation formation. This formation could be modified irradiation. Finally, the melting point of the high entropy alloy is valuable data to be collected. The melting point of an HEA is a good indication of the degree of entropy in the system, as the estimation of entropy within an HEA is based on the determined melting point. It will provide more information about the mechanism behind the establishment of the high entropy mixture system within the final product.

High entropy alloys with different methods of synthesis should also be included into future research. This means not only the modification of the electric arc furnace process used in this project, but also cross comparison of other different synthesis method, such as physical vapor deposition (PVD), high entropy mixing etc. Due to HEA properties being related to the homogeneity of the element distribution, it is critical to exam the effect of each synthesis method on the sample quality. During the synthesis of sample in this project, elemental segregation has been spotted in some samples which came from uneven mixing in synthesis. To remedy this insufficient mix, several techniques can be applied. Cold rolling can assist with the annealing process as a common method of homogenization, that allows for more even elemental distribution in a block of sample. Cooled rolling can also form the sample into more rectangular shape, increasing the utilisation single block sample. The other common method is increasing the stirring and melting time to maximise mixing. However, the time for stirring should be carefully controlled, as under the extreme high temperature some elements could evaporate and cause an unbalance in elements present in the final product. The cross comparison of HEAs with different synthesis method will provide information about the effect of synthesis process on the prepared HEA properties. In alternative synthesis methods, physical vapor deposition and high entropy mixing are two of the most interesting choices, as they are able to make high entropy alloy in atomic level. Fabricating a high entropy alloy at the atomic level can limit the movement of elements while maintain the uniform distribution of each elemental component. In comparison, the melt-cast rout will provide extra movement of atom migration during the solidification process. High entropy mixing is one of the advanced synthetic methods for making solid state solution material. High entropy mixing uses mechanical stirring to combine the ingredient directly in the solid form. Normally it would apply high speed ball milling, with nanosized elemental powders to ensure sufficient mixing and precise composition of produce powder. The majority of pure metal element is highly flammable, so the mixing process should be undertaken under vacuum or protective gas. After high entropy mixing, all ingredients should form the target alloy in powder form. This method can then take advantage from isothermal sintering which is able to apply same temperature across each particle in one die. Though the precise control of isothermal sintering, each particle will be diffused together without the need to be in liquid state. This maximises the advantage of the high entropy mixing in final product. However, this synthesis method is not perfect. Due to the nature of sintering, it will potentially leave more pores and microcracks in the final product. Physical vapor deposition (PVD), on the other hand, is very commonly used in making small alloy sample. In physical vapor deposition, the source material is vaporised and deposited on a substrate. This process can ensure all the source material is present in the alloy product at the same time with precise quantity control. It is a very convenient of making small amounts of sample which remove the heavy-duty work on section and polishing. The quality of PVD product is excellent, but it is not very good at avoiding the natural combination of certain elements. There are many other methods that are capable of delivering high quality high entropy alloy samples, involve more synthesis method not only be able to compare sample quality of each synthesis process, but also allow the evaluation of the high entropy alloy research design.

Modification of sample section and polishing process is also suggested, in this project, two section method are employed. Due to the button shape formed from the melting, the diamond wafer saw is limited by the clamping mechanism in order to perform a clean cut. In turn this can cause extra loss from the sample. Wire electrode electrical discharge machining is more suitable to preform sectioning of high entropy alloy samples. It has a much faster cutting speed and more controllable cutting slit. However, electrical discharge machining will pass a localised large current though the sample to carry out the cutting process. This might affect the sample in the various way not least of is modification of the microstructure. Although no noticeable different has been found during this project, the effect of this section method still needs to be thoroughly inspected. With cooled rolled alloy samples, a more aggressive cutting method can be applied such as band saw as long as the material near the cutting slit is removed.

Micro diamond particles were used in polishing, as they are one of the most effective methods for obtaining highly smooth surface on metallic samples. However, the dark band spotted on the sample surface is potentially linked by the diamond polishing process. Therefore, an additional step of polish is required to correct this problem, with a change from diamond to colloidal silica. This grinding agent is softer than the diamond which can reduce the mechanical stress on the sample surface. With this finishing polish process, the formation of dark band might be eliminated. All the samples in this project were ground and polished by hand, although a specially designed mounting tool was applied to ensure the flatness of surface. The auto polishing platform with Bakelite mounting is an ideal method to carry out all the polishing process, as Bakelite provides a universal shape for each set of samples which has benefit. Each Bakelite mounting can be installed with one group of samples to ensure all of them experiencing the same route to experiment and increase the comparability of each set of data. The auto polishing platform contains several mounting holes which allow the batch polishing to be carried out at same time. It is not only capable of preparing samples, but also controlling the polishing process to ensure a very similar sample condition. Thus, human error can be significantly reduced for the entire experiment. A possible problem from this modification plane is a temperature rising during ion implantation due to the poor thermal conductivity of Bakelite. This might lead the heat accumulation and an unwanted thermal impact to the high entropy alloy sample, which could change the microstructure. A solution to this problem is to add an extra piece of metal during the Bakelite mounting process which is glued to the high entropy alloy sample and acts as a heat sink/conduction path. The back of Bakelite sample would then be ground to expose the metal part to allow it to directly contact with mounting platform during the ion implantation.

The ion implantation strategy could also be altered to gain more efficiency. During this project, the ion implantation plan was sufficient to obtain irradiated high entropy alloy sample at the same time. However, it also leaves some problems which lead to loss of precious sample material. As an example, the irradiation zone from low dose ion implantation is not easily recognisable on the surface. Even with the mounting log image, it can still be tricky to determine which corner of the sample has been ion implanted due to four samples sharing the irradiation window with one corner on each sample. The ion implantation strategy used in this project, mainly focused on fitting as many samples as possible in limited irradiation experiment time. However, if irradiation zone can be enlarged to 4 cm^2 the entire sample surface could be irradiated with same ion concentration and the heat build-up on the surface could then have enough time to be dissipated. In addition, if more high entropy alloy samples were joined in the experiment, samples could be made into tiny bar shape, allowing for more sample to be mounted in one Bakelite sample holder. Each sample should directly contact with metal heat sink as mentioned earlier, as the ion implantation requires all samples are connect to ground which allow the charge to be balanced on sample. In this situation, the hidden metal piece will act as a circuit bus which connect to all samples at once. Other than the modification of ion implantation strategy, the ion implantation plan should also be expanded. Due to Covid-19 it was unfortunately not possible to undertake gold ion implantation, which was designed to simulate the high levels of accumulated radiation damage. Other than gold, an ingredient element in the alloy sample is also able to be applied as ion implantation source. This is to reduce the effect of an alien element introduced into local alloy system which allows the observation of irradiation damage more focused on itself.

The TEM and FIB are highly dependent on the skill of the operator. Apart from improvement in operator skills, there are changes to the operation to reduce the effects of an oxidation layer formation on freshly made TEM sample, with TEM observation being performed as soon as it made. During TEM sample fabrication, the thickness of sample should be milled down to approximately 60nm. Due to the complex microstructure within high entropy alloy, more detailed characteristics can be examined with thinner samples. An FIB is not the only method of making the TEM sample. Manual polishing is one of the potential alternations of making TEM samples. Although it will increase time and require skill to obtain a usable sample, it has the own advantage of making TEM sample with minimal effect of pollution which come from the ion milling can be completely avoided. A successful manual polished TEM sample with have much cleaner image and wider range of observation, through a cross section of the sample.

Higher resolution TEMs will significantly improve the quality and efficiency of image acquisition. However, in the future research, more advanced electron microscope could be applied to gain higher magnification image such as STEM. During this project, the alignment control is limited by the single tilt platform. A double tilt platform is able to provide wider range of the control the alignment between the crystal structure and electron beam. Thus, the diffraction image can be taken under much more ideal position. With that the crystal structure within target area can be thoroughly analysed. EDX mapping is helpful in this project which provide the element distribution analysis in the target area. In order to obtain more information, it requires higher magnification and more powerful electron to enhance the resolution.

Nano-indentation is one of the most suitable equipment of analysing the mechanical properties within the target material. This method can inspect an extreme thin layer of material without having the affection from the deeper material. However, an applicable range for the equipment is very limited, to obtain more comprehensive data, equipment with a wider applicable range should be employed in future research. With wider range of depth, the test range can cover from the surface to the non-irradiation effected zone. With light ion irradiation, the ion inserting can reach a depth larger than 1 μm. Normally the nano-intender would not reach this depth, so helium ion emission energy should be reduced to decrease the range of the irradiation affect zone. The clamping mechanism impacts the result of the nano-intender hardness test. The sample should be gently press down to the platform without any movement during the test. The adhesive used in this project may not have been very stable and could have impacted the results. A compact Bakelite sample holder could provide stable clamping to the test platform. This would not only stabilise the connection between the sample holder and test platform, but also cut the time between sample changing. Hence increasing both efficiency and accuracy of the nano-intender experiment.

There are experiments and tests that could be undertaken, that could expand the understanding of post irradiation HEA behaviour, such as corrosion resistance and mechanical properties. A more uniform volume of sample will provide more high-quality HEA to examine and help determine the universal properties of this novel material. The ultimate goal of this research is to establish increased understanding of this material type and determine its use within nuclear reactors.

References

[1] J. W. Yeh, “Physical Metallurgy of High-Entropy Alloys,” *Jom*, vol. 67, no. 10, pp. 2254–2261, 2015, doi: 10.1007/s11837-015-1583-5.

[2] Y. Zhang *et al.*, “Microstructures and properties of high-entropy alloys,” *Prog. Mater. Sci.*, vol. 61, no. September 2013, pp. 1–93, 2014, doi: 10.1016/j.pmatsci.2013.10.001.

[3] I. Florea, R. M. Florea, O. Bălţătescu, V. Soare, R. Chelariu, and I. Carcea, “High entropy alloys,” *J. Optoelectron. Adv. Mater.*, vol. 15, no. 7–8, pp. 761–767, 2013, doi: 10.1016/B978-0-12-800251-3.00001-8.

[4] E. Coyle D. and R. Simmons A., *Understanding the Global Energy Crisis*. 2014.

[5] World Energy Council, “World Energy Scenarios 2016,” *World Energy Counc.*, pp. 1–138, 2016, doi: ISBN: 978 0 946121 57 1.

[6] G. H. Kinchin and R. S. Pease, “The displacement of atoms in solids by radiation,” *Reports on Progress in Physics*. 1955, doi: 10.1088/0034-4885/18/1/301.

[7] N. Lior, “Sustainable energy development: The present (2011) situation and possible paths to the future,” *Energy*, 2012, doi: 10.1016/j.energy.2011.11.038.

[8] F. C. Olds, “NUCLEAR POWER ENGINEERING.,” *Power Eng. (Barrington, Illinois)*, 1975, doi: 10.13182/nse63-a28900.

[9] J. Kern, “Steam power plant,” in *Energy Conversion, Second Edition*, 2017.

[10] Y. Kim, M. Kim, and W. Kim, “Effect of the Fukushima nuclear disaster on global public acceptance of nuclear energy,” *Energy Policy*, 2013, doi: 10.1016/j.enpol.2013.06.107.

[11] J. Kenneth Shultis and R. Faw, *Fundamentals of Nuclear Science and Engineering*. 2002.

[12] K. Whittle, *Nuclear Materials Science*. IOP Publishing, 2016.

[13] R. Steffens, “Boiling water reactor system diagram,” *wiki*, 2004. https://commons.wikimedia.org/wiki/File:Boiling_water_reactor_english.svg (accessed Jun. 30, 2021).

[14] A. Robeson, “Nuclear Reactor Engineering,” *Nucl. Sci. Eng.*, 1982, doi: 10.13182/nse82-a20295.

[15] U.S.NRC., “File:PressurizedWaterReactor.gif - Wikimedia Commons,” *U.S.NRC.*, 2017. https://commons.wikimedia.org/wiki/File:PressurizedWaterReactor.gif

(accessed Jun. 30, 2021).

[16] S. J. Zinkle and G. S. Was, “Materials challenges in nuclear energy,” *Acta Mater.*, vol. 61, no. 3, pp. 735–758, 2013, doi: 10.1016/j.actamat.2012.11.004.

[17] J. H. Gwynne, *Nuclear Materials - Cambridge Materials Science*. 2013.

[18] Beao, “File:Sodium-Cooled Fast Reactor Schemata.svg - Wikimedia Commons,” *wiki*, 2009. https://commons.wikimedia.org/wiki/File:Sodium-Cooled_Fast_Reactor_Schemata.svg (accessed Jun. 30, 2021).

[19] L. C. Olson, J. W. Ambrosek, K. Sridharan, M. H. Anderson, and T. R. Allen, “Materials corrosion in molten LiF-NaF-KF salt,” *J. Fluor. Chem.*, vol. 130, no. 1, pp. 67–73, 2009, doi: 10.1016/j.jfluchem.2008.05.008.

[20] J. A. L. Robertson, “Zirconium-an international nuclear material,” *J. Nucl. Mater.*, vol. 100, no. 1–3, pp. 108–118, 1981, doi: 10.1016/0022-3115(81)90525-0.

[21] S. J. Zinkle and J. T. Busby, “Structural materials for fission & fusion energy,” *Mater. Today*, vol. 12, no. 11, pp. 12–19, 2009, doi: 10.1016/S1369-7021(09)70294-9.

[22] C. R. F. Azevedo, “Selection of fuel cladding material for nuclear fission reactors,” *Eng. Fail. Anal.*, vol. 18, no. 8, pp. 1943–1962, 2011, doi: 10.1016/j.engfailanal.2011.06.010.

[23] B. Cox and Y. M. Wong, “Hydrogen uptake micro-mechanism for Zr alloys,” *J. Nucl. Mater.*, 1999, doi: 10.1016/S0022-3115(98)00898-8.

[24] K. R. Whittle, M. G. Blackford, R. D. Aughterson, G. R. Lumpkin, and N. J. Zaluzec, “Ion irradiation of novel yttrium/ytterbium-based pyrochlores: The effect of disorder,” *Acta Mater.*, 2011, doi: 10.1016/j.actamat.2011.09.021.

[25] M. J. Norgett, M. T. Robinson, and I. M. Torrens, “A proposed method of calculating displacement dose rates,” *Nucl. Eng. Des.*, 1975, doi: 10.1016/0029-5493(75)90035-7.

[26] M. Saleh *et al.*, “Relationship between damage and hardness profiles in ion irradiated SS316 using nanoindentation - Experiments and modelling,” *Int. J. Plast.*, vol. 86, pp. 151–169, 2016, doi: 10.1016/j.ijplas.2016.08.006.

[27] J. G. Garland, “METALLURGY.,” *Met Constr Br Weld J*, 1974, doi: 10.4324/9781315682181-7.

[28] G. P. Sabol, “ZIRLO^{TM} - An alloy development success,” *J. ASTM Int.*, vol. 2, no. 2, 2005, doi: 10.1520/jai12942.

[29] R. Kozak, A. Sologubenko, and W. Steurer, “Single-phase high-entropy alloys - An

overview," *Zeitschrift fur Krist.*, vol. 230, no. 1, pp. 55–68, 2015, doi: 10.1515/zkri-2014-1739.

[30] J. W. Yeh *et al.*, "Nanostructured high-entropy alloys with multiple principal elements: Novel alloy design concepts and outcomes," *Adv. Eng. Mater.*, vol. 6, no. 5, pp. 299-303+274, 2004, doi: 10.1002/adem.200300567.

[31] J. W. Yeh, "Recent progress in high-entropy alloys," *Ann. Chim. Sci. des Mater.*, vol. 31, no. 6, pp. 633–648, 2006, doi: 10.3166/acsm.31.633-648.

[32] D. B. Miracle, "Critical Assessment 14: High entropy alloys and their development as structural materials," *Materials Science and Technology*, vol. 31, no. 10. pp. 1142–1147, 2015, doi: 10.1179/1743284714Y.0000000749.

[33] B. S. Murty, J. W. Yeh, and S. Ranganathan, "Alloy Design in the Twenty-First Century," *High Entropy Alloy.*, no. 1981, pp. 57–76, 2014, doi: 10.1016/B978-0-12-800251-3.00004-3.

[34] G. Meyrick and G. W. Powell, "Phase Transformations in Metals and Alloys," *Annu. Rev. Mater. Sci.*, 2003, doi: 10.1146/annurev.ms.03.080173.001551.

[35] Z. Li, "High Entropy Alloys | Max-Planck-Institut für Eisenforschung GmbH." https://www.mpie.de/3679520/high_entropy_alloys (accessed Jun. 30, 2021).

[36] Y. F. Kao, S. K. Chen, T. J. Chen, P. C. Chu, J. W. Yeh, and S. J. Lin, "Electrical, magnetic, and Hall properties of AlxCoCrFeNi high-entropy alloys," *J. Alloys Compd.*, 2011, doi: 10.1016/j.jallcom.2010.10.210.

[37] J. W. Yeh, S. Y. Chang, Y. Der Hong, S. K. Chen, and S. J. Lin, "Anomalous decrease in X-ray diffraction intensities of Cu-Ni-Al-Co-Cr-Fe-Si alloy systems with multi-principal elements," *Mater. Chem. Phys.*, 2007, doi: 10.1016/j.matchemphys.2007.01.003.

[38] W. Dong *et al.*, "Applications of high-pressure technology for high-entropy alloys: A review," *Metals (Basel).*, vol. 9, no. 8, 2019, doi: 10.3390/met9080867.

[39] D. C. Tsai, Y. L. Huang, S. R. Lin, D. R. Jung, and F. S. Shieu, "Effect of nitrogen flow ratios on the microstructure and properties of (TiVCr)N coatings by reactive magnetic sputtering," *Nucl. Instruments Methods Phys. Res. Sect. B Beam Interact. with Mater. Atoms*, 2011, doi: 10.1016/j.nimb.2011.01.127.

[40] M. A. Tunes *et al.*, "Investigating sluggish diffusion in a concentrated solid solution alloy using ion irradiation with in situ TEM," *Intermetallics*, 2019, doi: 10.1016/j.intermet.2019.04.004.

[41] S. Ranganathan, "Alloyed pleasures: Multimetallic cocktails," *Curr. Sci.*, 2003.

[42] O. N. Senkov and C. F. Woodward, “Microstructure and properties of a refractory NbCrMo0.5Ta0.5TiZr alloy,” *Mater. Sci. Eng. A*, 2011, doi: 10.1016/j.msea.2011.09.033.

[43] D. B. Miracle and O. N. Senkov, “A critical review of high entropy alloys and related concepts,” *Acta Mater.*, vol. 122, pp. 448–511, 2017, doi: 10.1016/j.actamat.2016.08.081.

[44] Y. Zou, S. Maiti, W. Steurer, and R. Spolenak, “Size-dependent plasticity in an Nb25Mo25Ta25W25refractory high-entropy alloy,” *Acta Mater.*, vol. 65, pp. 85–97, 2014, doi: 10.1016/j.actamat.2013.11.049.

[45] S. Baik, M. J. S. Rawlings, and D. C. Dunand, “Effect of hafnium micro-addition on precipitate microstructure and creep properties of a Fe-Ni-Al-Cr-Ti ferritic superalloy,” *Acta Materialia*. 2018, doi: 10.1016/j.actamat.2018.04.044.

[46] W. D. Callister, “Materials science and engineering: An introduction (2nd edition),” *Mater. Des.*, 1991, doi: 10.1016/0261-3069(91)90101-9.

[47] Y. Wu *et al.*, “In-situ neutron diffraction study of deformation behavior of a multi-component high-entropy alloy,” *Appl. Phys. Lett.*, 2014, doi: 10.1063/1.4863748.

[48] M. V. Ivchenko, V. G. Pushin, and N. Wanderka, “High-entropy equiatomic AlCrFeCoNiCu alloy: Hypotheses and experimental data,” *Tech. Phys.*, 2014, doi: 10.1134/S1063784214020108.

[49] C. P. Lee, Y. Y. Chen, C. Y. Hsu, J. W. Yeh, and H. C. Shih, “Enhancing pitting corrosion resistance of AlxCrFe1.5MnNi0.5 high-entropy alloys by anodic treatment in sulfuric acid,” *Thin Solid Films*, 2008, doi: 10.1016/j.tsf.2008.06.014.

[50] S. Banerjee and T. R. Govindan Kutty, “Nuclear Fuels,” in *Functional Materials*, 2012.

[51] B. S. Murty, J. W. Yeh, and S. Ranganathan, “Functional Properties,” *High Entropy Alloy.*, no. 1, pp. 149–158, 2014, doi: 10.1016/B978-0-12-800251-3.00009-2.

[52] B. S. Murty, J. W. Yeh, and S. Ranganathan, “Synthesis and Processing,” *High Entropy Alloy.*, pp. 77–89, 2014, doi: 10.1016/B978-0-12-800251-3.00005-5.

[53] “File:Propane air burner.jpg - Wikimedia Commons,” 2006. https://commons.wikimedia.org/wiki/File:Propane_air_burner.jpg (accessed Jun. 30, 2021).

[54] R. Fleming, “Induction furnace,” *Ind. Eng. Chem.*, 1912, doi: 10.1021/ie50043a611.

[55] ARGENTA, “INDUCTION MELTING ALLOY - INDUCTION MELTING ALLOY -.”

http://www.argenta.pl/en/catalogue/induction_melting_alloy/a/induction_melting_alloy (accessed Jun. 30, 2021).

[56] Arcast, “Arcast melter.” http://www.arcastinc.com/news.htm (accessed Jul. 01, 2021).

[57] SCHMIDT CD, “DIRECT ARC FURNACE IN THE CAST IRON INDUSTRY,” 1969.

[58] H. Ren, H. Zoz, G. Kaupp, and M. R. Naimi-Jamal, “Environmentally Protecting Reactive Milling,” no. February 2015, pp. 1–6.

[59] C. Suryanarayana, “Mechanical alloying and milling,” *Progress in Materials Science*. 2001, doi: 10.1016/S0079-6425(99)00010-9.

[60] 3dprintingindustry, “3D Printing Industry-The Authority on 3D Printing & Additive Manufacturing.” https://3dprintingindustry.com/news/optomec-lens-metal-3d-printing-systems-to-be-sold-to-u-s-government-147295/ (accessed Jul. 01, 2021).

[61] W. Liu and J. N. DuPont, “Fabrication of functionally graded TiC/Ti composites by laser engineered net shaping,” *Scr. Mater.*, 2003, doi: 10.1016/S1359-6462(03)00020-4.

[62] Total Materia, “Spark Plasma Sintering | Total Materia Blog.” http://blog.totalmateria.com/spark-plasma-sintering/ (accessed Jul. 01, 2021).

[63] W. Ji *et al.*, “Mechanical alloying synthesis and spark plasma sintering consolidation of CoCrFeNiAl high-entropy alloy,” *J. Alloys Compd.*, vol. 589, pp. 61–66, 2014, doi: 10.1016/j.jallcom.2013.11.146.

[64] C. Xiang *et al.*, “Corrosion behavior of several high-entropy alloys in high temperature high pressurewater,” *J. Chinese Soc. Corros. Prot.*, vol. 36, no. 2, 2016, doi: 10.11902/1005.4537.2016.024.

[65] S. Q. Xia, X. Yang, T. F. Yang, S. Liu, and Y. Zhang, “Irradiation Resistance in Al x CoCrFeNi High Entropy Alloys,” *Jom*, vol. 67, no. 10, pp. 2340–2344, 2015, doi: 10.1007/s11837-015-1568-4.

[66] J. F. Ziegler, M. D. Ziegler, and J. P. Biersack, “SRIM - The stopping and range of ions in matter (2010),” *Nucl. Instruments Methods Phys. Res. Sect. B Beam Interact. with Mater. Atoms*, 2010, doi: 10.1016/j.nimb.2010.02.091.

[67] J. P. Biersack and L. G. Haggmark, “A Monte Carlo computer program for the transport of energetic ions in amorphous targets,” *Nucl. Instruments Methods*, 1980, doi: 10.1016/0029-554x(80)90440-1.

[68] S. Cimmino, E. Martuscelli, and C. Silvestre, “Scanning Electron Microscopy

(SEM)," in *Test Procedures for the Blood Compatibility of Biomaterials*, 2011.

[69] J. I. Goldstein, D. E. Newbury, J. R. Michael, N. W. M. Ritchie, J. H. J. Scott, and D. C. Joy, *Scanning electron microscopy and x-ray microanalysis*. 2017.

[70] L. A. Bendersky and F. W. Gayle, "Electron diffraction using transmission electron microscopy," *Journal of Research of the National Institute of Standards and Technology*, vol. 106, no. 6. p. 997, 2012, doi: 10.6028/jres.106.051.

[71] M. Leslie, "Two microscopes are better than one," *Journal of Cell Biology*, vol. 192, no. 1. p. 3, 2011, doi: 10.1083/jcb.1921if.

[72] B. Poon, D. Rittel, and G. Ravichandran, "An analysis of nanoindentation in linearly elastic solids," *Int. J. Solids Struct.*, vol. 45, no. 24, pp. 6018–6033, 2008, doi: 10.1016/j.ijsolstr.2008.07.021.

[73] K. Whittle, "The challenges of nuclear waste," *Nucl. Mater. Sci.*, no. 100 m, pp. 1–21, 2016, doi: 10.1088/978-0-7503-1104-5ch7.

[74] Y. Zhang *et al.*, "Microstructures and properties of high-entropy alloys," *Prog. Mater. Sci.*, vol. 61, no. November 2013, pp. 1–93, 2014, doi: 10.1016/j.pmatsci.2013.10.001.

[75] T. Nagase, P. D. Rack, J. H. Noh, and T. Egami, "In-situ TEM observation of structural changes in nano-crystalline CoCrCuFeNi multicomponent high-entropy alloy (HEA) under fast electron irradiation by high voltage electron microscopy (HVEM)," *Intermetallics*, vol. 59, 2015, doi: 10.1016/j.intermet.2014.12.007.

[76] B. S. Murty, J. W. Yeh, and S. Ranganathan, "Structural Properties," *High Entropy Alloy.*, pp. 133–148, 2014, doi: 10.1016/B978-0-12-800251-3.00008-0.

[77] B. S. Murty, J. W. Yeh, and S. Ranganathan, "High-Entropy Alloy Solid Solutions," *High Entropy Alloy.*, pp. 91–118, 2014, doi: 10.1016/B978-0-12-800251-3.00006-7.

[78] C. Xiang *et al.*, "Corrosion behavior of several high-entropy alloys in high temperature high pressure water," vol. 36, no. 2, pp. 107–112, 2016, doi: 10.11902/1005.4537.2016.024.

[79] M. A. Tunes *et al.*, "Investigating sluggish diffusion in a concentrated solid solution alloy using ion irradiation with in situ TEM," *Intermetallics*, vol. 110, Jul. 2019, doi: 10.1016/j.intermet.2019.04.004.

[80] K. Jin et al., "Effects of compositional complexity on the ion-irradiation induced swelling and hardening in Ni-containing equiatomic alloys," Scr. Mater., 2016.

Appendix

elemant	form	size	piece	dansity(g*cm-3)	purity	company	code	total mass(g)
Nickel	foil	1m*250mm*0.0125mm	1	8.91	99.95%	advent	GI4164	27.84375
Iron	foil	50mm*50mm*0.25mm	10	7.87	99.50%	advent	GI669	49.1875
Molybdenum	foil	100mm*100mm*0.025mm	1	10.28	99.95%	advent	GI1901	2.57
Tantalum	foil	50mm*50mm*0.5mm	1	16.65	99.90%	advent	GI4490	20.8125
Aluminium	foil	100mm*100m*0.125mm	1	2.7	99.50%	advent	GI1930	3.375
Titanium	foil	100mm*100mm*0.25mm	1	4.51	99.6+%	advent	GI2463	11.275
Copper	foil	100mm*100mm*0.0125mm	10	8.92	99.90%	advent	GI1043	11.15
Niobium	foil	50mm*50mm*0.5mm	1	8.57	99.90%	advent	GI1892	10.7125
Zircornium	foil	100mm*100mm*0.5mm	1	6.51	99.20%	goodfellow	ls49202	33.1
chromium	broken plate	2-3mm thick	several	7.14	99.995%	alfa-aesar	u29a027	50
silicon	power	-140 mesh		2.33	98%	alfa-aesar	61600713	50
Hafnium	wire	Dimeter 1.0mm Length 2meter	1	13.31	97.00%	advent	Gi520510	20
Cobalt	wire	diameter 2.0mm length 100mm	1	8.9	99.99+%	Advent	Gi4269	2.8
Coblat	powder	`-400mesh			99.50%	alfa Aesar	44085	250
Coblat	foil	0.5mm*25mm*25mm	2		99.95%	alfa Aesar	42659	2.8*2
Coblat	foil	2.0mm*25mm*25mm	2		99.95%	alfa Aesar	42661	11.2*2

Appendix Figure 1 – The raw material purchased list

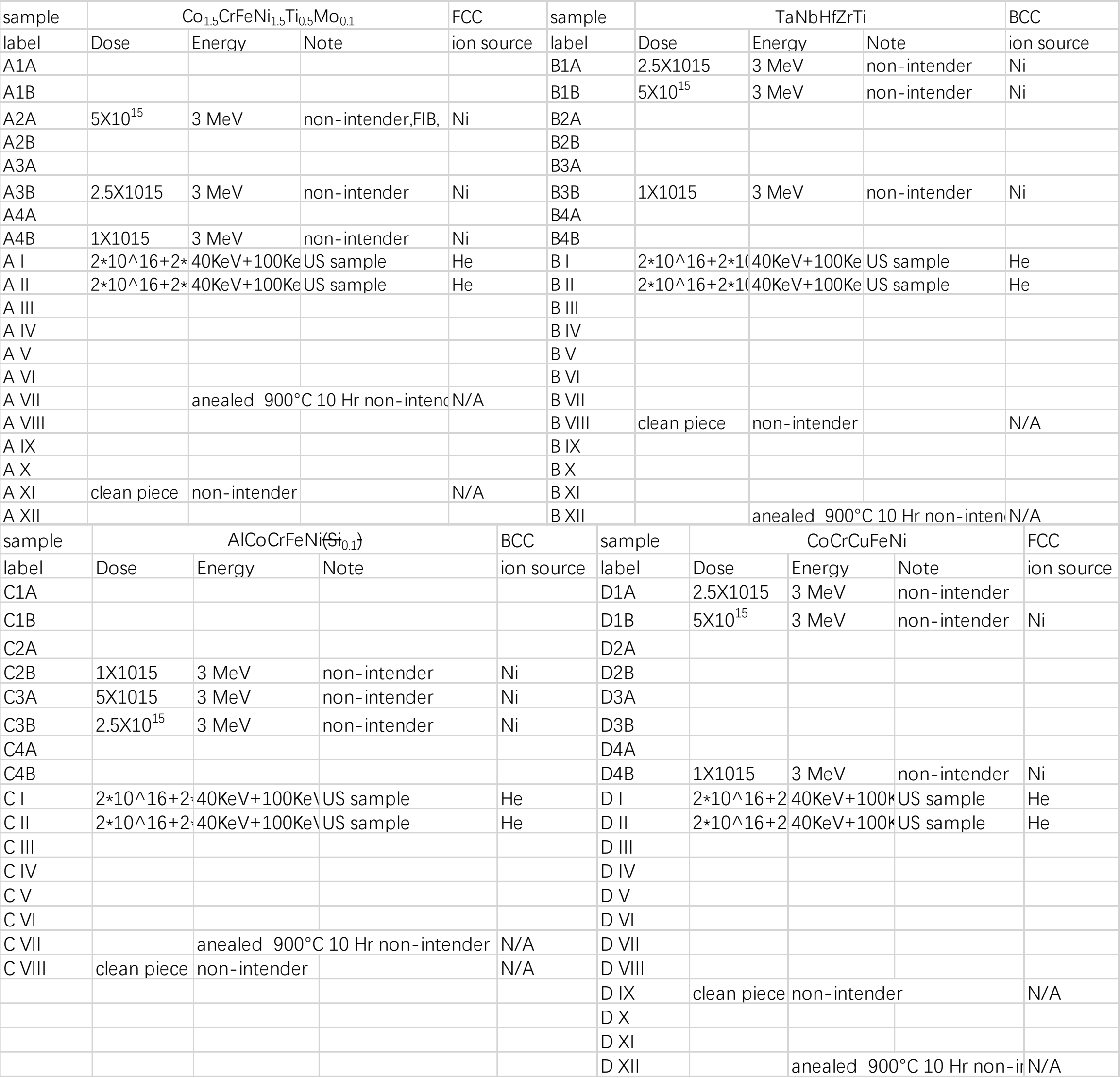

sample	Co$_{1.5}$CrFeNi$_{1.5}$Ti$_{0.5}$Mo$_{0.1}$			FCC	sample	TaNbHfZrTi			BCC
label	Dose	Energy	Note	ion source	label	Dose	Energy	Note	ion source
A1A					B1A	2.5X1015	3 MeV	non-intender	Ni
A1B					B1B	5X10^{15}	3 MeV	non-intender	Ni
A2A	5X10^{15}	3 MeV	non-intender,FIB,	Ni	B2A				
A2B					B2B				
A3A					B3A				
A3B	2.5X1015	3 MeV	non-intender	Ni	B3B	1X1015	3 MeV	non-intender	Ni
A4A					B4A				
A4B	1X1015	3 MeV	non-intender	Ni	B4B				
A I	2*10^16+2*	40KeV+100Ke	US sample	He	B I	2*10^16+2*1(	40KeV+100Ke	US sample	He
A II	2*10^16+2*	40KeV+100Ke	US sample	He	B II	2*10^16+2*1(	40KeV+100Ke	US sample	He
A III					B III				
A IV					B IV				
A V					B V				
A VI					B VI				
A VII		anealed 900°C 10 Hr non-intend		N/A	B VII				
A VIII					B VIII	clean piece	non-intender		N/A
A IX					B IX				
A X					B X				
A XI	clean piece	non-intender		N/A	B XI				
A XII					B XII		anealed 900°C 10 Hr non-inten		N/A

sample	AlCoCrFeNi(~~Si~~$_{0.1}$)			BCC	sample	CoCrCuFeNi			FCC
label	Dose	Energy	Note	ion source	label	Dose	Energy	Note	ion source
C1A					D1A	2.5X1015	3 MeV	non-intender	
C1B					D1B	5X10^{15}	3 MeV	non-intender	Ni
C2A					D2A				
C2B	1X1015	3 MeV	non-intender	Ni	D2B				
C3A	5X1015	3 MeV	non-intender	Ni	D3A				
C3B	2.5X10^{15}	3 MeV	non-intender	Ni	D3B				
C4A					D4A				
C4B					D4B	1X1015	3 MeV	non-intender	Ni
C I	2*10^16+2	40KeV+100KeV	US sample	He	D I	2*10^16+2	40KeV+100K	US sample	He
C II	2*10^16+2	40KeV+100KeV	US sample	He	D II	2*10^16+2	40KeV+100K	US sample	He
C III					D III				
C IV					D IV				
C V					D V				
C VI					D VI				
C VII		anealed 900°C 10 Hr non-intender		N/A	D VII				
C VIII	clean piece	non-intender		N/A	D VIII				
					D IX	clean piece	non-intender		N/A
					D X				
					D XI				
					D XII		anealed 900°C 10 Hr non-ir		N/A

Appendix Figure 2 – The sample mapping of each specimen